UNIVERSITAT POLITÈCNICA DE CATALUNYA BARCELONATECH

Quantification of dopaminergic neurotransmission SPECT studies with ^{123}I-labelled radioligands

Judith Gallego Blanco

Quantification of dopaminergic neurotransmission SPECT studies with ^{123}I-labelled radioligands

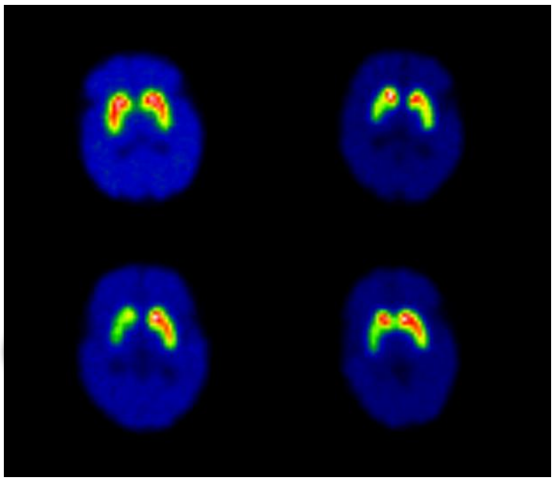

Author

Judith Gallego Blanco

Supervisors

Dr. Domènec Ros Puig and Dr. Albert Cot Sanz

DOCTORAL DISSERTATION

PH.D. IN NUCLEAR ENGINEERING AND IONISING RADIATION

UNIVERSITAT POLITÈCNICA DE CATALUNYA
BARCELONATECH
Escola de Doctorat

Acta de qualificació de tesi doctoral

Curs acadèmic:

Nom i cognoms

Programa de doctorat

Unitat estructural responsable del programa

Resolució del Tribunal

Reunit el Tribunal designat a l'efecte, el doctorand / la doctoranda exposa el tema de la seva tesi doctoral titulada _____

_____.

Acabada la lectura i després de donar resposta a les qüestions formulades pels membres titulars del tribunal, aquest atorga la qualificació:

☐ NO APTE ☐ APROVAT ☐ NOTABLE ☐ EXCEL·LENT

(Nom, cognoms i signatura) President/a	(Nom, cognoms i signatura) Secretari/ària

(Nom, cognoms i signatura) Vocal	(Nom, cognoms i signatura) Vocal	(Nom, cognoms i signatura) Vocal

_____, _____ d'/de _____ de _____

El resultat de l'escrutini dels vots emesos pels membres titulars del tribunal, efectuat per l'Escola de Doctorat, a instància de la Comissió de Doctorat de la UPC, atorga la MENCIÓ CUM LAUDE:

☐ SÍ ☐ NO

(Nom, cognoms i signatura) President de la Comissió Permanent de l'Escola de Doctorat	(Nom, cognoms i signatura) Secretari de la Comissió Permanent de l'Escola de Doctorat

Barcelona, _____ d'/de _____ de _____

ESCOLA TÈCNICA SUPERIOR D'ENGINYERIA INDUSTRIAL DE BARCELONA
(ETSEIB)

PH.D. IN NUCLEAR ENGINEERING AND IONISING RADIATION

Quantification of dopaminergic neurotransmission SPECT studies with ^{123}I-labelled radioligands

Thesis presented by Judith Gallego Blanco
for her doctorate at the Universitat Politècnica de Catalunya

Supervisors:
Dr. Domènec Ros Puig and Dr. Albert Cot Sanz

NOVEMBER 2015

Abstract

Dopaminergic neurotransmission SPECT studies with ^{123}I-labelled radioligands can help in the diagnosis of neurological and psychiatric disorders such as Parkinson's disease and schizophrenia. Nowadays, interpretation of SPECT images is based mainly on visual assessment by experienced observers. However, a quantitative evaluation of the images is recommended in current clinical guidelines. Quantitative information can help diagnose the disease at the early pre-clinical stages, follow its progression and assess the effects of treatment strategies.

SPECT images are affected by a number of effects that are inherent in the image formation: attenuation and scattering of photons, system response and partial volume effect. These effects degrade the contrast and resolution of the images and, as a consequence, the real activity distribution of the radiotracer is distorted. Whilst the photon emission of ^{123}I is dominated by a low-energy line of 159 keV, it also emits several high-energy lines. When ^{123}I-labelled radioligands are used, a non-negligible fraction of high-energy photons undergoes backscattering in the detector and the gantry and reaches the detector within the energy window.

In this work, a complete methodology for the compensation of all the degrading effects involved in dopaminergic neurotransmission SPECT imaging with ^{123}I is presented. The proposed method uses Monte Carlo simulation to estimate the scattered photons detected in the projections. For this purpose, the SimSET Monte Carlo code was modified so as to adapt it to the more complex simulation of high-energy photons emitted by ^{123}I. Once validated, the modified SimSET code was used to simulate ^{123}I SPECT studies of an anthropomorphic striatal phantom using different imaging systems. The projections obtained showed that scatter is strongly dependent on the imaging system and comprises at least 40% of the detected photons. Applying the new methodology demonstrated that absolute quantification can be achieved when the method includes accurate compensations for all the degrading effects. When the method did not include correction for all degradations, calculated values depended on the imaging system, although a linear relationship was found between calculated and true values. It was also found that partial volume effect and scatter corrections play a major role in the recovery of nominal values.

Despite the advantages of absolute quantification, the computational and methodological requirements needed severely limit the possibility of application in clinical routine. Thus, for the time being, absolute quantification is limited to academic studies and research trials. In a clinical context, reliable, simple and rapid methods are needed, thus, semi-quantitative methods are used. Diagnosis also requires the establishment of robust reference values for healthy controls. These values are usually derived from a large data pool obtained in multicentre clinical trials. The comparison between the semi-quantitative values obtained from a patient and the reference is only feasible if the quantitative values have been previously standardised, *i.e.* they are independent of the gamma camera, acquisition protocol, reconstruction parameters and quantification procedure applied. Thus, standardisation requires that the calculated values are compensated somehow for all the image-degrading phenomena.

In this thesis dissertation, a methodology for the standardisation of the quantitative values extracted from dopaminergic neurotransmission SPECT studies with ^{123}I is evaluated using Monte Carlo simulation. This methodology is based on the linear relationship found between calculated and true values for a group of studies corresponding to different subjects with non-negligible anatomical and tracer uptake differences. Reconstruction and quantification methods were found to have a high impact on the linearity of the relationship and on the accuracy of the standardised results.

Besides the aforementioned methodological works based on Monte Carlo simulation, the methods presented in this thesis were also applied in research and clinical frameworks with real studies from healthy subjects and patients.

Keywords: dopaminergic neurotransmission, ^{123}I SPECT, image degrading effects, Monte Carlo simulation, absolute quantification, standardisation.

Acknowledgements

This work could have not been completed without the participation of the following collaborators.

First and foremost, I want to thank Dr. Domènec Ros and Dr. Albert Cot for their guidance during these years. Their dedication, perseverance and endless need to know have been a daily inspiration for me.

I also thank Dr. Javier Pavía for his fruitful discussions and smart ideas, Dr. Carles Falcón for his help with SPM and his valuable suggestions, and Dra. Anna Mané and Dr. Joan Duch for giving me the opportunity to get involved in clinical research. I am also very grateful to Dra. Cristina Crespo and Dra. Aida Niñerola for their important collaboration in the works presented in this thesis.

Furthermore, I greatly appreciate the help of Dr. Francisco Calviño for giving me the opportunity to collaborate with research at the *Unitat de Biofísica i Bioenginyeria de la Facultat de Medicina de la Universitat de Barcelona*.

My gratitude also extends to all those people from INTE and the *Unitat de Biofísica i Bioenginyeria* for all the wonderful moments spent together. Special thanks to my family and friends for their patience, comprehension, interest and support.

Contents

List of Figures

List of Tables

List of Abbreviations

1D	One-Dimensional
2D	Two-Dimensional
3D	Three-Dimensional
AAL	Automated Anatomical Labelling
AQM	Absolute Quantification Method
ARF	Angular Response Function
CBD	Corticobasal Degeneration
CT	Computed Tomography
DAT	Dopamine Transporter
ESSE	Effective Scatter Source Estimation
ET	Essential Tremor
FBP	Filtered Back Projection
FOV	Field of View
FWHM	Full Width Half Maximum
IRBD	Idiopathic Rapid-eye-movement sleep Behaviour Disorder
LCC	Local Correlation Coefficient
LEHR	Low-Energy High Resolution
MC	Monte Carlo
ML-EM	Maximum Likelihood Expectation Maximization
MNI	Montreal Neurologic Institute
MR	Magnetic Resonance
MRI	Magnetic Resonance Imaging
MSA	Multiple System Atrophy
OS	Ordered Subsets
OS-EM	Ordered Subsets Expectation Maximization
PET	Positron Emission Tomography
PD	Parkinson's Disease
PDF	Probability Density Function
PM	Photomultipliers
PSF	Point Spread Function
PSP	Progressive Supranuclear Palsy

PVE	Partial Volume Effect
RBD	Rapid-eye-movement sleep Behaviour Disorder
RMSD	Root Mean Square Deviation
RO	Receptor Occupancy
ROI	Region of Interest
SBR	Specific Binding Ratio
SimSET	Simulation System for Emission Tomography
SNR	Signal-to-noise Ratio
SPECT	Single Photon Emission Computed Tomography
SPM	Statistical Parametric Mapping
SULS	Striatal Uptake Linear System
SUR	Specific Uptake Ratio
TCS	Transcranial Sonography
TDCS	Transmission-Dependent Convolution Subtraction
TEW	Triple Energy Window
VTA	Ventral Tegmental Area

Chapter 1

1 Introduction

1.1 The role of functional imaging in the study of the dopaminergic neurotransmission

1.1.1 The dopaminergic system

The nervous system contains a network of neurons that transmit signals to other specific target cells as electrochemical waves through cellular junctions called synapses. Synapses may be electrical, establishing a direct connection between neurons, or chemical. The neuron that sends the signal is called presynaptic and the target cell that receives the signal is called postsynaptic. The synaptic cleft is the space between the presynaptic and postsynaptic membranes.

In an electrical synapse, the presynaptic and postsynaptic cell membranes connect through special channels called gap junctions that are capable of passing electric current very quickly. In a chemical synapse, the presynaptic area contains the neurotransmitter which is a chemical that is stored in spherical vessels named synaptic vesicles. When the electrical impulse reaches the presynaptic terminal it releases the neurotransmitter into the synaptic cleft. Once released from the vesicles, the neurotransmitter is bound to the receptors embedded in the postsynaptic membrane and activates the cell. Depending on the type of receptor, the effect may be excitatory, inhibitory or modulatory.

Dopamine is a neurotransmitter which is implied in brain processes that regulate movement and emotional responses, and helps control the brain's reward and pleasure centres. So, dopamine regulation plays a crucial role in mental and physical health. Neurons containing dopamine are clustered in the midbrain in an

area called the *substantia nigra* and in the ventral tegmental area (VTA). Dopamine activates at least five types of dopamine receptors named D_1, D_2, D_3, D_4 and D_5, and it is removed from synapses by a protein called dopamine transporter (DAT). This protein, located in the membrane of the presynaptic neuron, sends the dopamine back to the vesicles for storage, thus finishing with the signal. Figure 1.1 shows a scheme of the dopamine biosynthesis, release and metabolism.

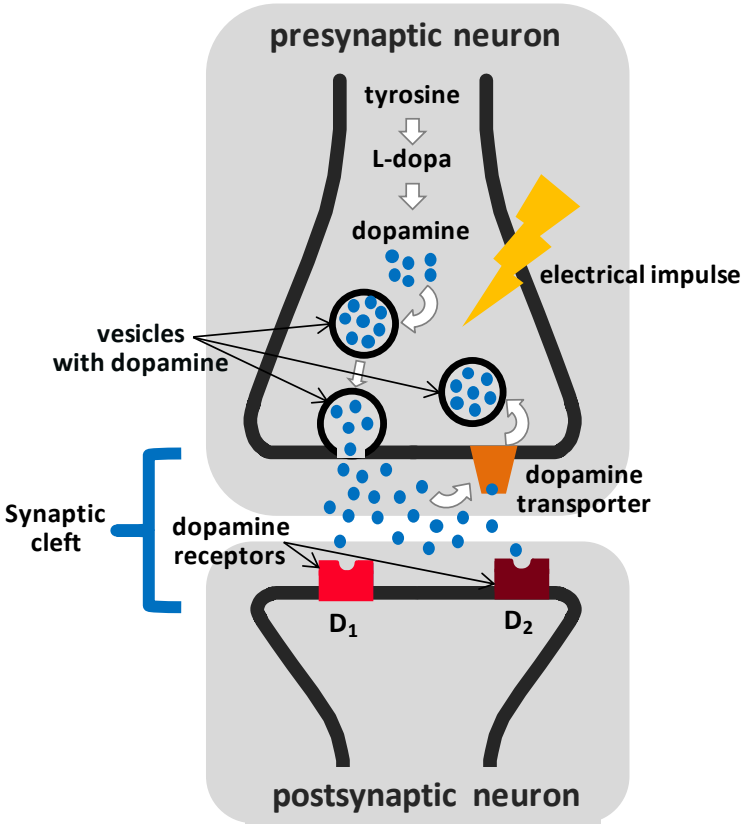

Figure 1.1 Scheme of the dopamine biosynthesis, release and metabolism.

1.1.2 Dysfunction of the dopaminergic system in patients with Parkinson's disease and schizophrenia

Dysfunction of the dopaminergic system has long been implicated in many neurological and psychiatric disorders. Of all the brain disorders associated with abnormal dopaminergic functioning, the most recognised dopamine-related disorder is Parkinson's disease (PD) and, with less straightforward evidence, the pathogenesis of schizophrenia.

Parkinson's disease

Parkinson's disease (PD) is a progressive degenerative neurological disorder that affects muscle movement and control, leading to severe limitations in daily activity and quality of life. It is associated with the loss of dopamine-secreting neurons projecting from the *substantia nigra* to the subcortical part of the forebrain called the striatum which, as a consequence, presents dopamine depletion (Kish *et al* 1988).

The caudate nucleus and the putamen are the striatal structures most associated with this pathology. As dopamine relays information between the *substantia nigra* and the areas of the brain that coordinate movements, when there is a shortage of available dopamine, the motor symptoms of PD appear. This usually affects people around the age of 60, although it can occasionally present at a much earlier age. Additional non-motor symptoms of PD may include depression, cognitive, behavioural and emotional problems, and sleep disorders.

There is no cure for PD, but various pharmaceutical and surgical treatments can help manage symptoms and improve the patient's quality of life. PD affects 0.5-1% of people in the age of 65-69 years and 1-3% of people over the age of 80, and it is the second most common neurodegenerative disorder after Alzheimer's dementia (Nussbaum and Ellis 2003). Symptoms tend to fluctuate and intensify over time.

The common clinical features shared by patients suffering from movement disorders are referred to as parkinsonism. There are different pathologies than can cause parkinsonism but PD accounts for around 80% of parkinsonism cases. Thus, people with PD classically present the symptoms associated with parkinsonism: tremor at rest (in hands, arms, legs, jaw and face), rigidity, bradykinesia (slowness of movement), hypokinesia (reduced movement), akinesia (loss of movement) and postural abnormalities (Marsden 1994).

The neurodegenerative diseases called Parkinson's syndromes include PD and Parkinson-plus syndromes, also referred to as atypical parkinsonism. The latter is a group of neurodegenerative diseases that present the classical features of parkinsonism with additional features that distinguish them from PD. They include multiple system atrophy (MSA) (Gilman *et al* 2008), progressive supranuclear palsy (PSP) (Brooks 2002) and corticobasal degeneration (CBD) (Mahapatra *et al* 2004). Discrimination of these disorders is a difficult task but it is key to the process of

differentiating patients who require different therapeutic strategies and have different prognoses.

Schizophrenia

Schizophrenia is a complex psychiatric disorder that affects approximately 1% of the population (Perälä *et al* 2007). Manifestations of the illness are commonly divided into positive, negative and cognitive symptoms. Positive symptoms include abnormalities in the perception or expression of reality such as auditory hallucinations, paranoid or bizarre delusions, or disorganised speech and thinking. Negative symptoms reflect a diminution or loss of normal functions, and include flattened affect, inability to experience pleasure, lack of drive and motivation, and social withdrawal (Andreasen and Olsen 1982). Cognitive symptoms comprise attention deficits, impaired executive functions such as planning, abstract thinking, rule flexibility and memory deficits (Gold and Harvey 1993). Onset of schizophrenia typically occurs in early adulthood and is often followed by a chronic and disabling course of the disorder.

Studies suggest that genetics, early environment, neurobiology, psychological and social processes are important contributory factors (Tsuang 2000, Walker *et al* 2004), but the neuropathology of schizophrenia remains unknown.

For many years scientists have suspected the involvement of dopamine, as increased dopamine presynaptic activity is consistently found in schizophrenic individuals (Reith *et al* 1994, Hietala *et al* 1995, Lindström *et al* 1999). It has been proposed that hyperactivity of dopamine transmission is responsible for positive symptoms. This hypothesis is based on the fact that a large number of antipsychotics have dopamine-receptor antagonistic effects (Seeman and Lee 1975) and dopamine-enhancing drugs have psychotogenic effects (Lieberman *et al* 1987). Functional imaging has shown elevated release of dopamine in the striatum of schizophrenic patients both at basal conditions (Abi-Dargham *et al* 2000) and in response to amphetamine (Laruelle *et al* 1996, Abi-Dargham *et al* 1998). Whilst not fully explaining the cause of schizophrenia, it shows the disruption of dopaminergic activity that it is observed in this disorder (Howes and Kapur 2009, Lyon *et al* 2011). Furthermore, it should be highlighted that the mainstay of treatment is antipsychotic medication, whose primarily function is to suppress dopamine activity.

1.1.3 Study of the dopaminergic neurotransmission using functional imaging

Non-invasive functional imaging using specific dopamine-related tracers can assess functioning at the presynaptic terminals or postsynaptic binding sites. Both positron emission tomography (PET) and single photon emission computed tomography (SPECT) are suitable for functional imaging.

Presynaptic functioning imaging

As previously mentioned, the presynaptic dopaminergic function is associated with DAT. DAT is the protein that controls the intensity and duration of dopaminergic neurotransmission by re-uptaking dopamine from the synaptic cleft (see figure 1.1) (Amara and Kuhar 1993, Giros and Caron 1993, Jaber *et al* 1997). Thanks to different studies and investigations, we now know that a reduction in the number of DATs denotes a reduction of the nigrostriatal dopamine function, which in turn decreases dopamine levels in the striatum (Uhl *et al* 1994, Counihan and Penney 1998, Bezard *et al* 2001). Thus, DAT density can serve as an imaging biomarker for diagnosing PD.

A number of cocaine analogues labelled with gamma-emitter radionuclides that bind to DAT sites have been developed for SPECT imaging of the dopaminergic system (Neumeyer *et al* 1994, Tatsch 2001, Halldin *et al* 2001, Johannsen and Pietzsch 2002). As the radiolabelled compound joins the DAT, the activity concentration in the striatum becomes an indicator of the DAT concentration. ^{99m}Tc and ^{123}I have been used for the study of the presynaptic dopaminergic function in SPECT studies. ^{123}I-FP-CIT, under the commercial name of DaTSCAN (GE Healthcare, UK), is the radiopharmaceutical currently used for DAT SPECT imaging. Due to its availability, cost and clinical results, neurotransmission SPECT imaging has now become a common tool in the *in vivo* study of presynaptic dopamine function in PD (Frey 2002, Huang *et al* 2003). DaTSCAN plays a major role in differentiating PD patients from patients with essential tremor (ET), since dopamine is depleted in PD patients but not in ET patients (Benamer *et al* 2000). DAT SPECT imaging has also been used to study the relationship between schizophrenia and DAT binding but results are still inconclusive (Laruelle *et al* 2000, Mateos *et al* 2005, Schmitt *et al* 2005).

An analogue of levodopa (L-DOPA), which is the immediate precursor of dopamine and it is used in the treatment of PD, is labelled with ^{18}F for PET scans of the striatal dopaminergic presynaptic function. ^{18}F-DOPA reflects the activity of the decarboxylating enzyme that generates dopamine from L-DOPA and the storage capacity of dopamine (Brown *et al* 1999). Studies suggest that in the early stages of PD, dopamine synthesis rate might be up-regulated as a compensatory phenomenon. Consequently, the uptake of ^{18}F-DOPA may be normal even in parkinsonian patients. In contrast, DAT is down-regulated, making ^{123}I-FP-CIT more sensitive for the early detection of PD (Zigmond MJ *et al* 1990). For economic reasons, ^{18}F-DOPA is less frequently used than ^{123}I-FP-CIT for monitoring the progression of the disease. In schizophrenia, studies using ^{18}F-DOPA and ^{11}C-DOPA have evidenced an overactivity of presynaptic dopamine in the striatum (Reith *et al* 1994, Hietala *et al* 1995, Lindström *et al* 1999, Kumakura *et al* 2007, Bose *et al* 2008).

Postsynaptic functioning imaging

SPECT and PET imaging can also be used to assess dopamine receptor binding. ^{123}I-IBZM (GE Healthcare, UK) is the most common radiopharmaceutical for imaging D_2 postsynaptic receptors in SPECT. It is used to differentiate PD patients from Parkinson-plus syndromes patients (Marshall and Grosset 2003, Gerasimou *et al* 2005, Plotkin *et al* 2005). The equivalent radiotracer for PET is ^{11}C-Raclopride (Catafau *et al* 2009). In schizophrenia, dopamine receptor availability in drug-naive or drug-free patients has been studied using functional SPECT and PET and no significant alterations in striatal D2 receptors that would indicate a D2 receptor abnormality in this disease were found (Lomeña *et al* 2004, Talvik *et al* 2006).

Functional imaging is used in pharmacology for the development of antipsychotic drugs. Drugs are labelled with selective radioligands such as ^{123}I-IBZM and ^{11}C-Raclopride to obtain SPECT and PET studies of the postsynaptic D2 dopamine receptors. These studies provide information about the degree of receptor occupancy, the minimum effective dose and the duration of the drug action (Fischman *et al* 2002).

1.1.4 The role of dopaminergic imaging in clinical diagnosis

Diagnosis of neurological and psychiatric diseases associated with disturbances of the dopaminergic system provide many challenges. Several symptoms are common to different disorders, making a straightforward clinical diagnosis difficult to ascertain, particularly in the early stages of the disease. What is more, many disorders do not have definite causes or do not have specific biomarkers or tests that allow a differential diagnostic. Thus, diagnosis requires the patient's complete medical history together with physical and neurological examinations.

Patients with parkinsonism

There is no definitive test for identifying PD in patients and so diagnosis is based on clinical criteria that range from the presence of pre-motor clinical signs such as olfactory loss, rapid-eye-movement sleep behaviour disorder (RBD), somnolence, and late age onset anxiety and depression, to the presence of motor symptoms. In the early stages of the disease, clinical signs may be subtle or can be confused with other Parkinson's syndromes. Furthermore, clinical diagnosis can be influenced and complicated by symptomatic medication. Early and accurate diagnosis of PD is important for correct prognostication and management and avoidance of unnecessary medical examinations and therapies. Dopaminergic neurotransmission functional imaging may assist diagnosis.

Diagnosis using functional SPECT and PET imaging is primarily based on visual assessment by experienced observers (Benamer *et al* 2000). Functional imaging of the presynaptic dopaminergic system discriminates patients with PD from healthy subjects by identifying dopaminergic deficits in caudate and putamen with high specificity and sensitivity (Weng *et al* 2004, Eshuis *et al* 2009). The shape of the striatum and its completeness offers valuable information about left or right asymmetric radiopharmaceutical uptake, as the loss of the dopaminergic neurons starts ipsilaterally, on the contralateral side to the symptoms (Asenbaum *et al* 1997). SPECT images of healthy volunteers show similar, uniform uptake in caudate and putamen which make the whole striatum present a "comma-shaped" form (figure 1.2b). The neurological degeneration that takes place in PD makes the striatum lose its shape and become, in severe cases, "point-like" (figure 1.2c). Reduction of striatal uptake is more profound in advanced stages than in the early stages of the disease.

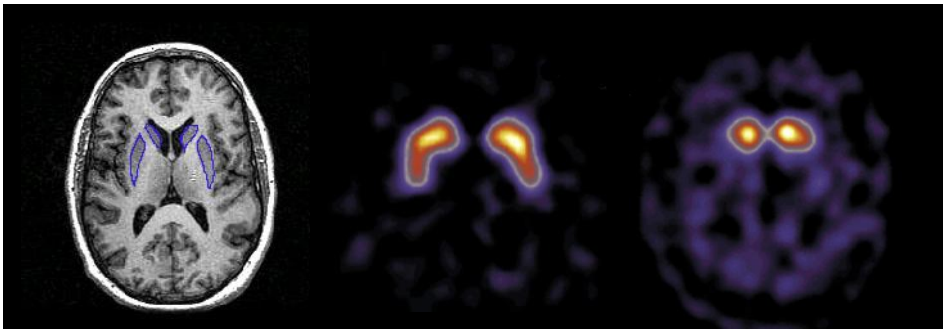

a **b** **c**

Figure 1.2 Slice from a magnetic resonance imaging (MRI) scan showing the caudate nucleus and the putamen delineated in blue **a**; slice of a neurotransmission SPECT study of a healthy subject **b**; slice of a neurotransmission SPECT study of a patient suffering from PD at an advanced stage of the disease **c**. Note that in **c**, the intensity of the image has had to be increased to obtain uptake values comparable to **b**.

In clinically uncertain cases, presynaptic dopaminergic imaging may assist in discriminating between neurodegenerative parkinsonism and its mimics, since non-neurodegenerative patients, such as patients with ET, show a tracer uptake similar to healthy controls (Catafau and Tolosa 2004). However, DAT imaging cannot help differentiate PD from atypical parkinsonian syndromes, since both are associated with presynaptic dopaminergic deficiency (Varrone *et al* 2001). In contrast, postsynaptic D2 receptor imaging can help differentiate between PD and atypical parkinsonism since patients suffering from PD usually show normal or up-regulated D2 receptor binding while patients with atypical parkinsonism show reduced binding (Schreckenberger *et al* 2004).

Patients with schizophrenia

In recent decades, empirical evidence from post-mortem, *in vivo* neuroimaging, neurochemical and neuropsychological studies have confirmed structural abnormalities, biochemical abnormalities and impairments in brain functioning in patients with schizophrenia. Specifically, alterations in the dopaminergic system have been long implicated in schizophrenia. Dopaminergic imaging could provide a key to the understanding of the dysfunction of the dopaminergic system in patients with schizophrenia as well as serve as a diagnostic tool. Nevertheless, the results found so far are still discordant, in part due to the clinical heterogeneity of the disorder. For this reason, current diagnosis of schizophrenia is still based on

behavioural observations by clinicians and self-reports by the patients about their abnormal mental experiences.

1.2 Quantitative evaluation of dopaminergic imaging in SPECT

Dopaminergic neurotransmission SPECT functional images contain valuable information about quantitative distribution of the radiotracer in the striatum. As previously mentioned, the clinical evaluation of this information is normally based on visual assessment but it would be beneficial to have a quantitative assessment wherever possible. Quantitative information can help diagnosis together with descriptive findings. Besides being observer-independent, quantification is especially valued in early diagnosis of the disease at pre-clinical stages (Booij *et al* 1999), for staging of the patient, for therapeutic management and in follow-up (Buvat 2007). Quantification is, therefore, one of the main topics of research in medical imaging today. Functional images can establish normal or disease-related states, and indicate response to treatment.

The radiotracer distribution as it appears on the images is affected by a number of non-desirable effects that are inherent in the image formation: attenuation, the scattered photons detected, the system response and the partial volume effect (PVE). As a consequence, the contrast and resolution of the images are degraded and the real activity distribution of the radiotracer is distorted. For some time now, a large number of studies have been devoted to the development of accurate corrections for these degradations and, until now, the area has been an intensive field of research for SPECT studies. Accurate corrections may require multimodal imaging and the use of simulation techniques with calculation times which are difficult to incorporate into clinical routine. Thus, a truly accurate correction of all the degrading factors is, for the time being, limited to academic studies (Cot *et al* 2005, Crespo *et al* 2008) and research trials.

In any case, a semi-quantitative evaluation of the images is highly recommended in clinical routine. Wherever possible, nuclear medicine practitioners employ dedicated software to elicit numerical information from the images and calculate different semi-quantitative ratios between regions with specific uptake (caudate and putamen) and regions with non-specific uptake (reference areas). Evaluation of the calculated ratios is performed by comparing those values corresponding to (preferably) age-matched normal controls obtained using the same imaging system

and the same acquisition, reconstruction and quantification protocols. The quantitative information obtained this way is reproducible, observer-independent and can help clinical diagnosis along with visual assessment, making semi-quantitative evaluation more and more necessary in clinical protocols.

A major drawback of this practice is that semi-quantitative results from different cameras, or from the same camera but under different acquisition, reconstruction or quantification protocols, cannot be compared directly. Standardised values, independent of the different imaging set-ups used, can be obtained by compensating somehow for all the degrading effects so as to recover the true original ratios (El Fakhri *et al* 2001, Soret *et al* 2003).

In recent works using anthropomorphic phantoms, a linear relationship between measured and true values has been found for a single subject. Some research groups use this relationship to standardise their results (Varrone *et al* 2013), although its applicability to any other subject or group of subjects has not yet been clearly argued nor demonstrated (Gallego *et al* 2015). Assuming that this methodology proved to be suitable, standardised values could be achieved in a straightforward manner.

Standardisation is essential for the creation of large data bases from multicentre studies with reference values for normal and pathological stages. This database would make it possible to derive robust conclusions about age effects and gender differences, for example. A simple methodology for the standardisation of the semi-quantitative values derived from SPECT neuroimaging is crucial for the accurate assessment of neurological diseases such as PD and schizophrenia.

Chapter 2

2 Aim of the thesis

2.1 Statement of the problem

SPECT allows evaluating the functionality of the nigroestriatal dopaminergic system, which is of great interest in PD and schizophrenia. In order to help diagnosis, quantification is recommended. However, accurate quantification of SPECT images is impaired by a number of degrading factors such as attenuation, scattered photons, system response and partial volume effect.

The development of methodologies that can compensate these degrading effects requires a tool which allows an evaluation of the performance of the implemented method. Monte Carlo (MC) simulation makes it possible to generate SPECT projections from known activity distributions. Since the ground truth is known, MC simulation allows us to evaluate the reconstruction algorithms, the compensations that have been included, and the quantification methods applied. In order to obtain reliable results in the evaluation, the suitability of the selected MC code for the simulation of the SPECT studies is crucial.

There are several dedicated MC codes for SPECT imaging (Buvat and Castiglioni 2002). One of these codes, SimSET (Haynor *et al* 1991), uses a collimator/detector response to reduce the simulation time spent in tracking photons through the collimators. In particular, it uses an analytical function which only considers the geometric response of the collimator. This simplification is valid when simulating low-energy photons, such as the 140 keV corresponding to the mono-energetic emission from ^{99m}Tc or the 159 keV line from ^{123}I (with a yield of 97%). However, for the high-energy photons emitted by ^{123}I (3%), which have energies between 248 and 783 keV, this simplification leads to inaccurate simulations, since septal

penetration and scatter within the collimator and in the backscatter compartment (De Vries *et al* 1990) cannot be neglected. Other MC codes reproduce the contribution to the projections of high-energy photons by tracking photons in the collimator but with unacceptably long calculation times. Thus, there is a clear need for a model that allows the rapid and realistic simulation of the contribution of high-energy photons in SPECT studies using ^{123}I.

Several reconstruction algorithms which include corrections for the degrading phenomena have already been developed for the absolute quantification of SPECT studies with ^{99m}Tc (Beekman *et al* 2002, Cot *et al* 2005). However, when ^{123}I-labelled radioligands are used, the scatter correction becomes more complex due to the additional contamination caused by the high-energy emission from ^{123}I. This highlights the need for a specific methodology for the absolute quantification of ^{123}I SPECT studies of the dopaminergic system that includes an accurate correction of the high-energy scatter component. Such an approach permits the study of different degrading phenomena that have an effect on SPECT imaging, assessing their individual influence, both visually and quantitatively, and evaluating the reconstruction methods applied. Due to its high degree of complexity and computational burden, this methodology is basically applied to research trials.

In a clinical context, reliable, simple and rapid methods are needed to quantify the studies. Absolute quantification has computational and methodological requirements which hamper its application in clinical routine. Thus, semi-quantitative methods are used. Diagnosis assessment also requires the establishment of robust reference values for healthy controls. These values are usually derived from a large data pool obtained in multicentre clinical trials, so that the semi-quantitative values obtained from a patient can be compared with the reference. However, this comparison is only feasible if the quantitative values have been previously standardised, *i.e.* they are independent of the gamma camera, acquisition protocol, reconstruction parameters and quantification procedure applied. Standardisation requires that the calculated values derived from the images are compensated somehow for all the image-degrading phenomena.

2.2 Aim

The aim of this thesis was to provide a methodology that allowed the accurate quantification of dopaminergic neurotransmission SPECT studies when ^{123}I-

labelled radioligands are used. The study was developed considering the two contexts where quantification is required, *i.e.* research and clinical routine.

To this end the following specific objectives were established:

1. Adaptation and validation of the Monte Carlo simulator SimSET for SPECT studies with ^{123}I which includes both low and high-energy emissions.

2. Development and validation of a complete methodology for the absolute quantification of dopaminergic neurotransmission SPECT studies with ^{123}I to be applied in research trials.

3. Development and validation of a straightforward methodology for the standardisation of the semi-quantitative values extracted from dopaminergic neurotransmission SPECT studies with ^{123}I which can be applied in clinical routine.

2.3 Contents of the thesis

This thesis starts with an introduction to the study of the dopaminergic system using functional imaging and its role in the clinical diagnosis of Parkinson's disease and schizophrenia (chapter 1). In this context, the aim is established and three specific goals are determined to fulfil the main objective of this doctoral dissertation (chapter 2). The background information about acquisition, data processing and the use of Monte Carlo simulation in SPECT imaging is described in chapter 3. Next, each of the three specific goals of the thesis is explained, methodologically addressed and developed in turn (chapters 4, 5 and 6), one per objective. Thus, chapter 4 describes the changes introduced to the MC code SimSET to adapt it to the simulation of ^{123}I SPECT studies and demonstrates its validity, chapter 5 presents and validates a methodology for the absolute quantification of ^{123}I SPECT studies of the dopaminergic neurotransmission system to be applied in research trials, and chapter 6 proposes and validates an alternative methodology to achieve standardised results from the semi-quantitative values extracted from dopaminergic neurotransmission SPECT studies with ^{123}I-labelled radioligands which can be applied in clinical routine. In addition, the contribution of these methodologies in several clinical works proposed and developed by other researchers in the fields of PD and schizophrenia is discussed in chapter 7. Finally, chapter 8 provides the concluding remarks.

Chapter 3

3 Acquisition, data processing and Monte Carlo simulation in SPECT imaging

3.1 Data acquisition

A SPECT neuroimaging study starts with the intravenous administration of a radiotracer to the patient. The radiotracer consists of a gamma-emitter radionuclide together with a ligand, which leads the radionuclide to the region of the body under study. Following a time delay after injection, photons emitted from the radiotracer start to be detected *in vivo* by a rotating gamma camera which acquires a set of 2D planar projections at evenly spaced angles around the patient over a full 360° arc (Anger 1958). Figure 3.1 shows one of the SPECT gamma-cameras installed at Hospital Clínic of Barcelona (Barcelona, Spain).

In dopaminergic SPECT imaging of the presynaptic function, the radiopharmaceutical injected into the patient is a cocaine analogue which binds to DAT. Postsynaptic levels can also be targeted by SPECT tracers that bind to the postsynaptic D1 and D2 receptors. The radionuclides most widely used in SPECT neuroimaging are ^{99m}Tc and ^{123}I. ^{99m}Tc has a simple decay scheme with a low-energy photon emission of 140 keV, while ^{123}I emission is dominated by a low-

energy photon emission of 159 keV (97%) and other emission lines of higher energies up to 783 keV (3%).

Figure 3.1 SPECT gamma camera (Hospital Clínic of Barcelona).

A gamma camera consists of several (from one to three) detector heads containing a collimator and a scintillation detector with position logic circuits, and a data analysis computer. The detector heads are attached to a gantry for motion control. Each detector head is shielded from background radiation leaving a large open detection area (typically 25x50 cm) where the collimator and a thin NaI(Tl) crystal are located (see figure 3.2). Only triple or dual head dedicated SPECT gamma cameras are recommended for brain imaging.

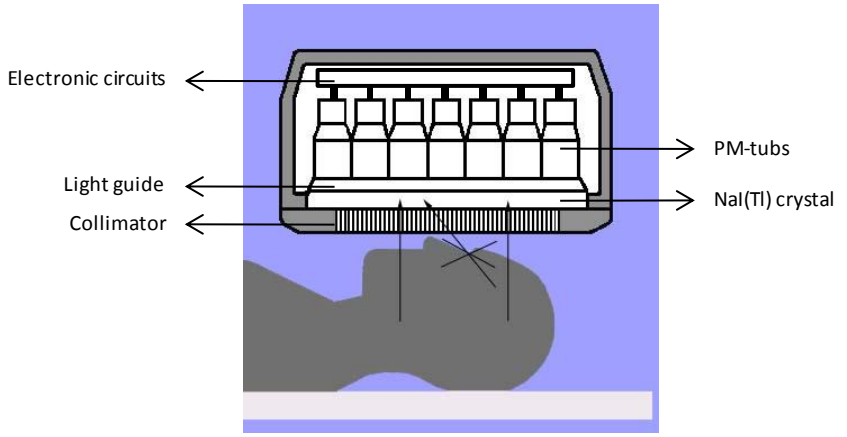

Figure 3.2 Components of the detector head of a gamma camera. The tracer emits radiation isotropically but the collimator holes set the direction of the detected photons.

The collimator sets the acceptance angle for the detection of the emitted photons. It consists of a pattern of several tens of thousands of holes perforating a slab of lead. The holes are a few centimetres long and a few millimetres in diameter, usually of hexagonal shape. The lead walls between the holes are called septa. As few photons are capable of going through the lead septa, projections mainly correspond to those photons which have travelled along the holes. The hole diameter, the collimator thickness and the septal thickness have a direct impact in the sensitivity of the collimator. The collimator ensures that the direction of the detected photons is well known, but it drastically reduces the sensitivity of the gamma camera, *i.e.* the number of detected photons divided by the number of emitted photons, which is typically around 10^{-4}.

Brain SPECT imaging is often performed with parallel and fan-beam collimators. In parallel collimators, the holes are perpendicular to the plane of the lead plate and parallel to each other. Thus, the image and the object have the same size. In fan-beam collimators, the holes are parallel to each other in the *y-axis* but not in the *x-axis*, as it is shown in figure 3.3. In such geometrical configuration, the holes point towards a focal line which is parallel to the collimator plane. In this case, the image is augmented in the *x*-direction.

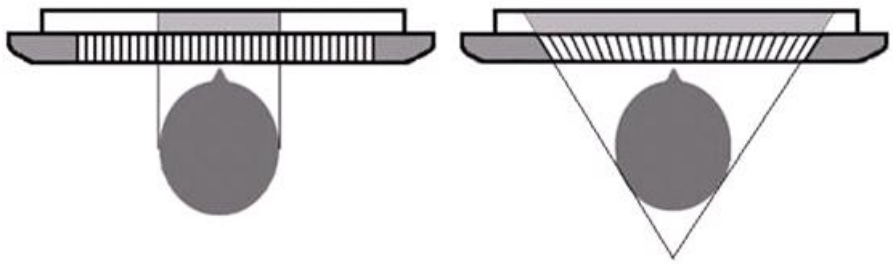

Figure 3.3 Different collimator configurations used in brain SPECT imaging: (left) parallel collimator and (right) fan-beam collimator.

The detector of the gamma camera is generally a NaI(Tl) crystal of about one centimetre thick. This crystal presents optimal detection efficiency for the energy range used. Photons interact with the crystal by means of photoelectric effect or Compton scattering and produce light in proportion to the energy deposited in the crystal in a process known as scintillation. Light is then led to an array of photomultipliers (PM) tubs by a glass light guide. The PM-tubs convert the light photons into electrons, amplify the number of electrons and convert them into an electrical pulse. Pulses are processed through position logic circuits which allow

the localization of the detection in the crystal. Finally, the detected photon is accepted or rejected depending on its energy. As the energy resolution of the detector is around 10% for energies ranging from 100 to 200 keV, the energy detection window is usually fixed at around 15-20% of the photopeak energy of the gamma-emitter radionuclide.

The position of the detected photon is incorporated into a digitalised image which has been divided into a grid. Each square of the grid (known as "bin") constitutes an element of the matrix that holds information on the number of detections registered on each element. In neuroimaging, the size of the matrix is set to 128 x 128 bins. The total information stored constitutes a projection of the object on the detector plane.

The acquired projections are finally reconstructed with a processing computer which applies tomographic reconstruction algorithms to obtain the volumetric 3D distribution of the tracer inside the body. In order to obtain the reconstructed image, projections have to be acquired at a sufficient number of angles. In SPECT neuroimaging, 120 or 128 projections over 360° are acquired depending on the gamma camera used. The scan time is set to acquire more than 3 million total counts, which takes about 40 minutes. The distance between the detection heads and the patient, *i.e.* the rotational radius, is set to be the smallest possible with appropriate patient safeguards.

3.2 Image degrading effects

SPECT projections are severely affected by a number of non-desirable effects that degrade the quality of the images. The most important effects are: statistical noise, attenuation of the photon flux, improper detection of the scattered photons and collimator/detector blurring. These image degrading effects result in poor spatial resolution, low contrast and high noise levels in the images, and may have a large impact on quantitative accuracy if left uncorrected. In the following sections, a description of each degrading effect is given. Figure 3.4 synthesizes the events that a photon can undergo after its emission from the radiotracer distribution in the patient.

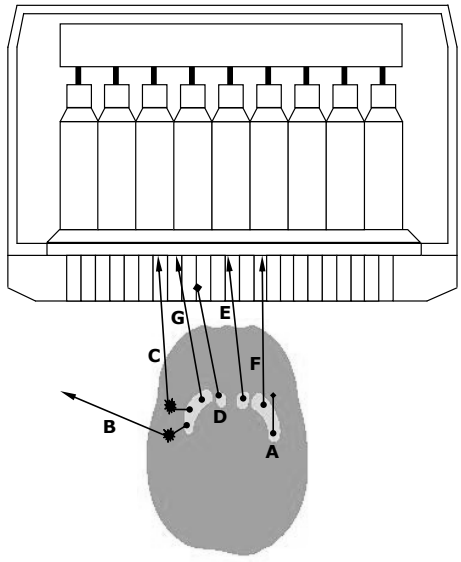

Figure 3.4 An emitted photon can be: attenuated by the surrounding tissues by means of photoelectric (A) or scatter interactions (B), detected after scattering (C), absorbed by the collimator septa (D), and, detected after travelling along the holes (E and F) or after penetrating the collimator septa (G).

3.2.1 Statistical noise

Since the radiotracer photon emission follows a Poisson probability distribution, SPECT projections are certainly affected by statistical noise.

Signal-to-noise ratio (SNR), which is the ratio between the mean counts and the noise at each bin of the projection, can be improved using longer acquisition times, higher dose administrations or by increasing the number of detectors and the size of the bin. However, none of these are appropriate or technically possible in a clinical context. A longer study time increases patient discomfort and the possibility of movement, as well as reduces the number of patients that can be attended per day. Radiotracer doses are limited due to radiological protection criteria. The number of detection heads in the gamma camera is technically limited to three and brain SPECT imaging requires high resolution images with small bin sizes.

3.2.2 Attenuation of the photon flux

The photon flux is attenuated by the patient media on its way to the detector. As shown in figure 3.5, photons may be absorbed by photoelectric absorption (photon A) or scattered (photon B) in such a way that they will not become part of the projection. Thus, attenuation causes a non-uniform decrease in the signal, which will vary depending on the length and tissues that each photon has to go through as well as on the photon's energy.

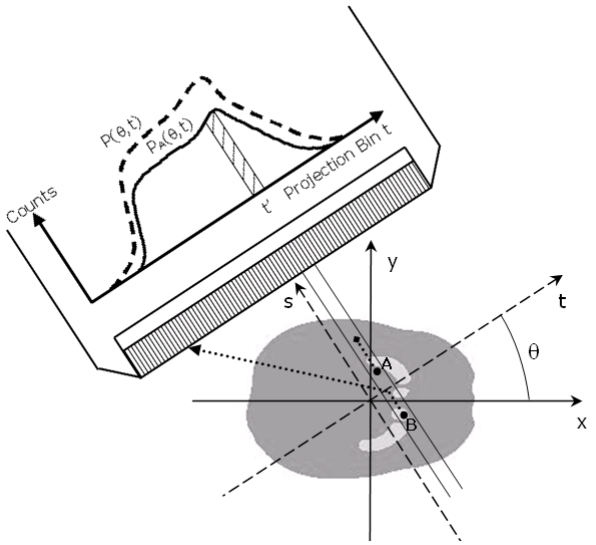

Figure 3.5 Impact of attenuation on SPECT imaging: photon A is attenuated by photoelectric absorption, while photon B suffers Compton scattering and it is not detected. As a result there is a decrease in the number of counts in the projection data (solid line) with respect to the ideal SPECT imaging (dashed line).

For photons emitted with energies between 50 keV and 1000 keV, the most probable interaction with matter is Compton scatter. At lower energies (below 100 keV) and for materials such as the lead walls of the collimator, photoelectric absorption is also relevant. Coherent scatter (Rayleigh scatter) can be the dominant interaction at small angles of scatter (Kaplan *et al* 1998). Thus, in brain SPECT studies, attenuation is mainly due to Compton scatter and to some photoelectric absorption.

A mono-energetic beam of photons I passing through a non-uniform medium of thickness d is attenuated according to the following equation:

$$I = I_0 \cdot exp\left(-\int_0^d \mu(x)dx\right) \qquad (3.1)$$

Where I_0 stands for the incident photon flux and μ is the linear attenuation coefficient of the material, which depends on the photon energy. In SPECT neuroimaging μ values for brain and bone are 0.143 cm^{-1} and 0.304 cm^{-1} for ^{99m}Tc, and 0.149 cm^{-1} and 0.307 cm^{-1} for the low-energy emission from ^{123}I, respectively. Thus, bone causes stronger attenuation than brain. Attenuation is also more probable for those photons originated in inner tissues. Attenuation results in regions with the same activity distribution making a different contribution to the projection.

3.2.3 Scattered photons detected

Photons which have undergone scatter before detection are an important source of haziness in the projections as they are tracked back incorrectly during reconstruction. As a consequence, the contrast of the reconstructed images is affected and quantitative accuracy is degraded. The impact of scatter in the projections is illustrated in figure 3.6.

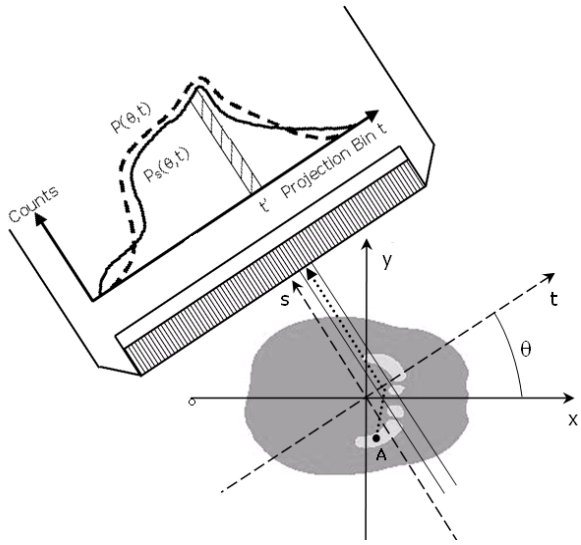

Figure 3.6 Impact of scatter on SPECT imaging: the addition of the scattered photon A leads to its incorrect location in the projection (solid line) with respect to the ideal SPECT imaging (dashed line).

If narrow energy detection windows are used, the amount of scattered photons can be reduced during the acquisition. The energy window is centred on the energy of the dominant emission and has a width which depends on the system's energy resolution. Usually, energy detection windows are set to 15-20% of the photopeak energy. When ^{123}I-labelled radiotracers are used, a fraction of the high-energy photons emitted reach the detector crystal within the energy window. This is possible due to the interactions that these photons undergo at the backscatter compartment of the detector. Thus, an important part of the detected photons in the projections would have suffered scatter.

3.2.4 The spatially variant collimator/detector response

Another source of degradation is the finite, distance-dependent spatial resolution of the imaging system. As shown in figure 3.7, the image of a point source in air through the collimator/detector system is a 2D distribution. This distribution is called the point spread function (PSF) and its width is the spatial resolution of the system. PSF depends on the geometrical characteristics of the collimator, the intrinsic resolution of the detector, the energy of the incident photon and the distance from the collimator. PSF can be described by two variables: sensitivity, which is the number of photons detected per emitted photon, and resolution, which is defined as the full width half maximum (FWHM) of the planar projection of a point source. Resolution has two components, the collimator resolution and the intrinsic resolution of the detector and electronics.

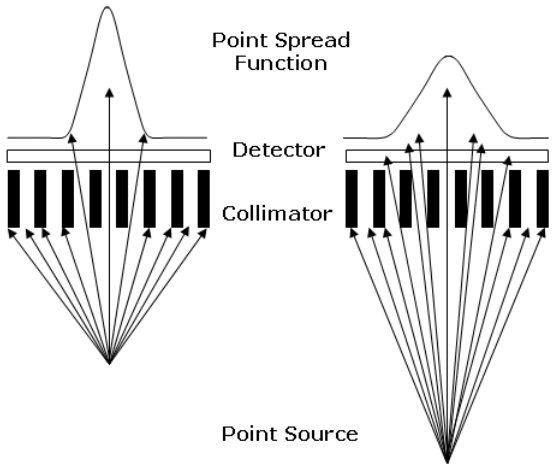

Figure 3.7 PSF of a point source at different distances.

Collimator resolution is illustrated in figure 3.8. In this figure, both photon A, which is emitted parallel to the *s-axis*, and photon B, which is angled relative to the *s-axis*, are geometrically accepted through the holes of the collimator.

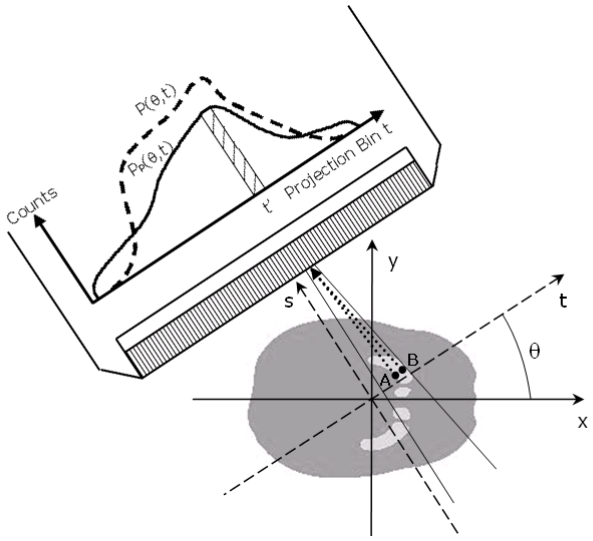

Figure 3.8 Impact of the spatial resolution of the imaging system on SPECT imaging: both photon A, which is emitted parallel to the s-axis, and photon B, which is angled relative to the s-axis, are geometrically accepted through the holes of the collimator contributing to the same projection bin (solid line).

The collimator design plays a major role in the sensitivity and resolution compromise. Smaller holes improve resolution but decrease sensitivity. Since collimator resolution also depends on the distance between the source and the camera, detector heads are positioned as close as possible to the patient. In brain SPECT imaging, resolution is the main objective because of the small volume of the structures. Thus, Low-Energy High Resolution (LEHR) parallel and fan-beam collimators characterised by small hole diameters are used. Although parallel collimators are the most widely used in SPECT, fan-beam collimators are especially indicated for brain SPECT as they provide greater count rate capability and a wider area of detection while retaining a reasonable resolution.

3.2.5 Other image degrading effects

Other image degrading effects, of minor relevance compared to the phenomena highlighted above, are associated with non-linearity and non-uniformity of the

detector and the inaccuracy of its centre of rotation, and these can usually be corrected by the camera software. On the other hand, biological factors such as the tracer kinetics and target specificity and more importantly, patient and organ movement, have a disturbing effect which has recently become of great concern as quantification gets more accurate (Koch *et al* 2007a). As in SPECT neuroimaging there is no internal organ motion, patient movement can be reduced by the use of head restraints.

3.3 Image reconstruction

The projections acquired by the gamma camera need to be reconstructed to obtain the volumetric distribution of the source inside the patient. The final image is obtained using mathematical algorithms which process and reconstruct the projection data set on a computer.

Until now, filtered back projection (FBP) has been the most widely used reconstruction technique in clinical routine. Nevertheless, an alternative methodology, iterative reconstruction, is gaining popularity since it is being included in most SPECT camera software packages. It is in research, however, where the particularities of iterative reconstruction are exploited most. The main advantage of iterative reconstruction is that it allows including accurate information about the object and the gamma camera in the algorithm, so images can be compensated for the degrading phenomena. Unfortunately, the modelling of these effects is much demanding in terms of processing time than FBP.

3.3.1 Filtered back projection

FBP reconstruction provides an exact, analytical solution to the ideal problem of reconstructing the source from geometrical projections, *i.e.* when no degradations are involved in the process. Its popularity is mainly due to its simplicity and to the fact that the reconstruction time needed is very short. The value in each pixel of the image is calculated as the sum of the values of all the bins of the acquired projections that can receive photons from that pixel divided by the number of projections. Back projection takes into account the fact that the contribution of a given pixel to a given bin depends on their relative positions and acquisition angle.

FBP is based on the central section theorem, which relates the 1D Fourier transform of the projections with the 2D Fourier transform of the image evaluated on the line that the projection was taken. FBP turns to be the convolution product between the projection and a ramp filter. The aim of the ramp filter is to recover the high frequencies which have been attenuated in the back projection process. Uniform images or with soft changes would be characterised by low frequency components while details or strong changes would need high frequencies to be represented properly.

In a real case, FBP produces noisy images which show a streak artefact because image degradations are not considered and because the number of projections is finite. In order to improve the reconstructed images, compensations for the degrading effects have to be applied.

Improving image signal-to-noise

Noise has high frequency components that are strengthened in FBP reconstruction due to the ramp filter. It is therefore necessary to apply additional low-pass filters to smooth the images, although these will affect the spatial resolution. One of the filters most frequently used to improve noise is the Butterworth filter:

$$H(w) = \sqrt{\frac{1}{1+\left(\frac{w}{w_c}\right)^{2n}}} \qquad (3.2)$$

Where w_c is the cut-off frequency, *i.e.* the frequency above which the noise is eliminated, and n is the order of the filter and controls the slope of the function. Thus, a high order will result in a sharp decrease. The cut-off and order of the filter will depend on the protocol of the centre and their selection is a trade-off between resolution and noise.

Attenuation correction

The Chang algorithm is the methodology most commonly used in clinical routine to correct attenuation after FBP reconstruction (Chang 1978, 1979). Chang's method consists in a post-reconstruction correction which seeks to compensate for attenuation by multiplying each point in the body by a correction factor. The correction matrix is generated using a homogeneous linear attenuation coefficient of 0.10-0.12 cm^{-1} for ^{123}I and 0.12-0.14 cm^{-1} for ^{99m}Tc. The value of the coefficient

depends on whether the acquired projections have been previously corrected for scatter or not. In the absence of scatter correction, the lowest values are selected. For each transaxial slice, the shape contour of the brain including the scalp should be defined or, if this is not available, some kind of approximation. In any case, this correction can only be a rough approximation, since it is only reasonable for a point source surrounded by a homogeneous medium.

PSF correction

PSF can be approximately corrected by applying a Metz filter (Metz and Beck 1974, Metz *et al* 1980), but this is not usual.

Scatter correction

There are many approaches for correcting scatter but, in general, all methods can be classified into two groups: those based on measurements, *i.e.* applying empirical methods that involve the direct measurement of the scatter fraction present in the projections, and those based on the modelling of the scatter distribution.

In clinical routine, only very basic scatter correction methods are used (Hutton *et al* 2011). The empirical method most widely used to estimate the scattered fraction in acquired projections is the Triple Energy Window (TEW) (Ogawa *et al* 1991, Ichihara *et al* 1993). This method is based on the energy spectrum data and consists of using two additional energy windows during the acquisition. The additional windows are relatively narrow and are placed at each side of the photopeak to achieve a good estimation of the scatter distribution and a realistic estimate of the amount of scattered photons detected. The primary fraction in each projection bin is estimated by correcting the detected photons in the photopeak window by the mean value of the lateral windows. Its advantages of speed and simplicity have lead to TEW being adopted as a standard scatter correction. More sophisticated multi-windows methods have since been developed (Haynor *et al* 1995), but they have not demonstrated a clear advantage over TEW (Assié *et al* 2010).

Far more frequently, scatter is compensated during reconstruction rather than corrected in the projections. This compensation involves applying an effective linear attenuation coefficient in the Chang's method. Its value, which is lower than that used when projections have been corrected for scatter, seeks to compensate

for both attenuation and scatter phenomena within the object. The coefficient is calculated to under correct the primary photons of the projections in such a way that the reconstruction of a cylinder with uniform activity distribution results in a uniform image.

3.3.2 Iterative reconstruction

The accuracy of the images improves if all the degrading effects that occur during the acquisition are modelled in the reconstruction algorithm. Iterative reconstruction can carry out this modelling but it requires long computational times. Thus, until recently, iterative reconstruction was limited to research. Nowadays, access to more powerful computers as well as the appearance of accelerated codes is starting to bring iterative algorithms within clinical reach. However, the accurate modelling of most degradations requires methodologies that are still too complex to be implemented in clinical routine and so they are only found in research trials.

Iterative reconstruction proposes a probabilistic interpretation of the problem which is suitable due to the stochastic nature of the radioactive decay process. In iterative algorithms, an initial estimate of the activity distribution is used to generate the estimated projections, for example, a uniform image or an image obtained by FBP. The generated projections are then compared with the real acquired projections. As a next step, the result of this comparison is used to update the estimation of the activity distribution. The process of forward projection, comparison and updating continues iteratively until the errors achieve a predefined value or the maximum number of iterations is reached. Iterative algorithms use a transition matrix to model the forward projection. An accurately modelled transition matrix leads to more realistic estimations of the activity distribution.

Among the different iterative algorithms, Maximum Likelihood Expectation Maximization (ML-EM) (Shepp and Vardi 1982, Lange and Carson 1984) is the most commonly used for SPECT. The advantages which have contributed to its popularity are its good theoretical base and its convergence (Chornoboy *et al* 1990). ML-EM seeks to find a general solution that is the best estimate for the activity distribution, *i.e.* the mean number of radioactive disintegrations in the image that can produce the acquired projections with the highest likelihood. ML-EM algorithm updates all the voxels in the image λ_i using the following expression:

$$\lambda_i^{k+1} = \frac{\lambda_i^k}{\sum_{j=1}^{nbin} t_{ji}} \cdot \sum_{j=1}^{nbin} \frac{t_{ji} \cdot p_j}{\sum_{m=1}^{nvox} t_{jm} \cdot \lambda_m^k} \qquad (3.3)$$

Where λ_i^{k+1} is the image new estimation at iteration $k+1$; t_{ji} represents the transition matrix, which are the probabilities that a photon emitted in voxel i contributes to the projection bin j; p_j represents the measured projections; and $\sum_m t_{jm} \cdot \lambda_m^k$ is the projection bin j after forward projection of the image estimation at iteration k. Although accuracy improves with each iteration, random noise also increases at each computation step. It is therefore important to establish the number of iterations needed to reach the image quality or quantitative parameters required by the user.

ML-EM is so slow that this scheme is almost always accelerated by the most widely used accelerating technique, the ordered subsets algorithm (OS). This algorithm, which was introduced by Hudson and Larkin in 1994, was added to the EM algorithm, resulting in the Ordered Subsets Expectation Maximization (OS-EM). The acceleration given by the OS algorithm comes from grouping the projection data into an ordered sequence of subsets. EM algorithm is then applied to the first subset of projections and the result is considered to be the starting estimate of the next subset. This acceleration does not degrade the quality of the images but reduces the computational time needed by a factor which is proportional to the number of subsets used (Kamphuis *et al* 1996). This acceleration leads to clinically acceptable reconstruction times, allowing its introduction in routine use for selected applications instead of FBP (Koch *et al* 2006, Catafau *et al* 2008).

Fully 3D reconstruction is necessary to accurately model photon crosstalk between transaxial slices. However, the problem can be simplified to 2D reconstructions by considering each tomographic section of the image individually. 2D approximations are favoured for clinical routine primarily because 3D reconstructions, although improving the quality of the reconstructed images, require a larger matrix together with major computational considerations (Guilland *et al* 1994).

The transition matrix

The transition matrix T models the forward projection and re-projection. Each element of this matrix stands for the probability that a photon originated in the voxel s_i of the activity distribution image is observed in the projection bin p_j. The transition matrix is generated based on the relative geometric positions between

the emitter voxels and the detector bins, and considering an ideal projection of the object, *i.e.* supposing perfect collimation and detection.

The transition matrix has a number of columns equal to the number of voxels in the image and a number of rows equal to the number of bins in the projection. Given an activity distribution s, the projection data p can be estimated by using the transition matrix:

$$\sum_i T_{ji} \cdot s_i = p_j \quad (3.4)$$

This process of mathematically projecting emulates imaging and so this is where the physics of SPECT need to be included. Including an accurate modelling of all the physical effects of the photon transport (*i.e.* attenuation, collimator/detector blurring and scatter) is necessary to find the original activity distribution of the source. The reconstruction algorithm solves the inverse problem as the unknown variable is the activity distribution of the source.

Modelling of the PSF

The distance dependent collimator response describes, for a given point source, the spatial distribution of the detected photons. Thus, the modelling of the PSF calculates the probability of detection of the photons through the collimator/detector system. PSF can be described by a Gaussian function whose standard deviation varies with the distance in a way that the farthest planes are blurred the most. The modelling of the PSF must be incorporated into the transition matrix to compensate for the loss of resolution.

PSF has several components including geometric, scatter, and septal penetration components. For low-energy photons, several analytic models have been proposed to model PSF. These models only take into account the geometric component of the PSF and do not model scattering or penetration within the collimator (Metz *et al* 1980, Tsui and Gullberg 1990, Frey *et al* 1998, Pareto *et al* 2002). These approximations are considered to be accurate enough for low-energy photons where the geometric component accounts for approximately 95% of the total PSF for both parallel and fan beam collimators (Cot *et al* 2002).

When radionuclides which emit high-energy photons are used, such as ^{123}I in neuroimaging, the non-geometric components of the PSF turn out to be non-

negligible. The decrease of the absorption cross section and the increase of the Compton cross section cause the geometrical component to become less relevant than septal penetration and scattering (Cot *et al* 2004). Thus, the analytical model for low-energy photons is not valid for high-energy emitters. PSF for ^{123}I high-energy photons emission has been modelled by Cot *et al* 2006 and is described in section 3.5.2.

Including the modelling of the PSF in the transition matrix improves the resolution of the reconstructed images.

Modelling of the attenuation effect

Attenuation is described by the photon path length through the attenuating object from the voxel source to the projection bin and by the characteristics of the materials that the photon goes through, *i.e.* the linear attenuation coefficients of brain and bone in neuroimaging. The density distribution of each patient is known as the attenuation map. Subject specific attenuation maps can be generated from computed tomography (CT) scans by segmenting the different tissues, or from transmission data obtained with the SPECT camera and a transmission source (Welch *et al* 1997). In any case, images have to be accurately coregistered with the SPECT data in order to position the map correctly, which is not an easy task in some cases. A great advance has been achieved with hybrid SPECT/CT systems which simultaneously acquire SPECT and CT data, as they ensure a good attenuation modelling.

If the attenuation map is known, the different global attenuation factors that correspond to each element of the transition matrix can be calculated. Thus, the transition matrix can be corrected for attenuation. If attenuation correction is not included, reconstructed images present a reduction of the signal in the centre of the body compared with the borders.

Modelling of the scattered photons detected fraction

There are many methodologies proposed for correcting scatter. Although for clinical routine only the most simple are applied, there are also much more complex approaches which seek to achieve ideal scatter correction. As mentioned earlier, the scattered fraction of the projections can be estimated using direct measurement or modelling (Beekman *et al* 1997, Kadrmas *et al* 1998). In both cases, estimated

scatter can be directly subtracted from the projections prior to reconstruction, or incorporated into the iterative reconstruction. The latter can model scatter during reconstruction by including it in the transition matrix, calculating it *on-the-fly*, or estimating it separately.

Scatter can be modelled using different approaches. One of the methodologies proposed is based on the calculation of the scatter response using the Klein-Nishina scatter equations (Riauka and Gortel 1994), but it requires long processing times and large data storage. Another approach is the transmission-dependent convolution subtraction method (TDCS) (Meikle *et al* 1994) originally based on the convolution of the photopeak counts by a mono-exponential function modelling the scatter response. One final method is the slab-derived scatter estimation (Frey and Tsui 1993, Beekman and Viergever 1995) which relies on response tables calculated for a source placed behind slabs of water of variable thickness. This method was extended with the development of effective scatter source estimation (ESSE) (Frey and Tsui 1996) which incorporates the attenuation from each point of Compton interaction to the detector.

An alternative to these simplified models would be the use of Monte Carlo (MC) simulation (see section 3.5) to calculate scatter for each subject. Until recently, calculation times were considered wholly unpractical, especially if scatter had to be re-estimated at each iteration. Nowadays, methods which accelerate simulations by combining stochastic photon transport within the patient media with analytical models for detection have demonstrated that MC simulation is a feasible tool for scatter estimation given the distributions of activity and attenuation coefficients (Beekman *et al* 2002, Cot *et al* 2006).

Methods which model the scatter distribution in the transition matrix map scattered photons back to their point of origin instead of trying to determine a separate estimation of the scatter (Kadrmas *et al* 1998, Lazaro *et al* 2005). Although these methods have potential benefits in terms of signal-to-noise, the inclusion of attenuation, collimator blurring and scatter in the transition matrix leads to prohibitive calculation times and memory requirements (Floyd *et al* 1986). As an alternative, measured or pre-calculated scatter can be treated as a constant term in the denominator of the ML-EM algorithm or can be iteratively updated during reconstruction. These methods use an unmatched projector/backprojector pair known as dual matrix implementation (Kadrmas *et al* 1998, Kamphuis *et al* 1998). The projection step includes attenuation, detector blurring and scatter, whereas the

back-projection includes only attenuation and detector blurring. As a result, the reconstruction process is accelerated. The main advantage of adding the scatter term in the denominator of the algorithm is that it avoids direct subtraction, which negates the assumption of Poisson distributed counts in the projections and can result in negative values. These methods achieve their high accuracy by modelling scatter using MC simulations of low-noise projections, which avoids the need for massive transition matrix storage (Beekman *et al* 2002). The MC-based scatter correction method developed by our group is described in chapter 5.

3.4 Image quantification

Visual interpretation of the reconstructed images is, in general, suitable for clinical assessment. Thus, in a clinical context, diagnosis is still predominantly based on experienced observers' assessment of the striatal activity. Visual assessment gives an idea of whether the radiotracer uptake is normal or abnormal, and may provide information about asymmetries and the structures most affected. Thus, the striatum shape, symmetry, gradient between caudate and putamen and degree of activity reduction is examined. However, since it depends heavily on the observer's experience and shows inter- and intra-observer variability (Verhoeff *et al* 1993), current clinical guidelines recommend a quantitative analysis of the studies that can offer an objective assessment and improve diagnostic accuracy (Darcourt *et al* 2010).

Within the context of functional brain imaging, the aim of quantification is to provide a reliable numerical measure of the brain function (Zaidi and El Fakhri 2008). Quantification is especially attractive in the process of early diagnosis of Parkinson's disease, for differential diagnosis (Koch *et al* 2007b), for prognosis (as it can help stage the patient), to strengthen diagnosis (Habraken *et al* 1999), improve sensitivity and for therapeutic management and follow-up (Seibyl *et al* 1997, Booij *et al* 2001, Buvat 2007). In recent years, many methods which seek to quantify the images have been developed and quantification is still a major field of research in SPECT imaging.

3.4.1 Absolute quantification

The quantitative values extracted from reconstructed images are affected by the degradations that functional SPECT images present. All these effects need to be

compensated for if we want quantification values that are close to the theoretical ones. In order to recover the true values that correspond to the real distribution of the radionuclide in the patient's brain, absolute quantification is needed. Absolute quantification is only dependent on the patient's brain function.

As mentioned above, the development of accurate corrections for degradations is still a highly active field of research on the path to absolute quantification. In chapter 5 the full methodology developed by our group for the absolute quantification of SPECT studies of the dopaminergic system is explained in detail. Nevertheless, although methodologies based on the correction of all degradations for each subject are accurate, realistic and instructive, the need for additional CT images to generate individual attenuation maps and magnetic resonance (MR) images to create subject specific maps of the regions of interest (ROI), calculation times and storage data requirements still make it prohibitive to transfer these methods into clinical routine. So, for the time being, they are applied only for academic purposes and research trials, where these practical limitations are not so crucial.

3.4.2 Semi-quantitative evaluation

At present, quantification mainly relies on semi-quantification methods. These methods use dedicated software to elicit numerical information from the reconstructed images to quantify radiopharmaceutical uptake in the regions of interest, *i.e.* caudate and putamen, with respect to reference areas. Convenient semi-quantitative parameters to measure are the specific uptake ratio (SUR) or the specific binding ratio (SBR). Both ratios are a measure of the mean counts in the ROIs defined in the striatum with respect to the mean counts in ROIs defined in areas which are devoid of nigrostriatal neurons, such as the occipital lobe. Determination of derived indexes such as putamen to caudate ratios, left and right asymmetries, etc. are also helpful when interpreting results.

Although visual assessment is still the basis of image interpretation, semi-quantitative evaluation is recommended in clinical protocols. However, there is no common methodology either in the definition of the ROIs or in the indexes chosen to evaluate the images, and its implementation varies from centre to centre. This means that many semi-quantitative methods have been developed to assist diagnosis. The main differences between them lie in the procedure chosen to draw and locate the ROIs on the image. This procedure can vary from manual drawing

methods to automated techniques based on normalisation, registration, fusion and segmentation (Badiavas *et al* 2011). While manual positional methods are more usually found in clinical routine, advanced automated and semi-automated quantification methods are already being used in research trials.

Anatomical ROIs based on MRIs

A recent magnetic resonance imaging (MRI) scan of the patient can be used to draw the patient's striatum structures and define precise anatomical ROIs. In this technique, the segmentation of the structures can be drawn manually or solved using specific software such as FSL (FMRIB, University of Oxford, UK) (Patenaude *et al* 2011). In order to place the ROIs ready for quantification, the ROIs map and the MRI scan need to be coregistered with the SPECT image. The use of external markers attached to the patient's head increase the accuracy of SPECT-MR registration (Seibyl *et al* 1995, van der Wee *et al* 2008). ROIs obtained by this method can be considered a gold standard as they are based on the individual morphology of each patient.

The technique is particularly useful when a region presents a very low uptake poorly contrasted on the functional image. Unfortunately, this methodology is difficult to adopt in clinical routine as MRI scans are not usually included in the diagnostic procedures for PD and schizophrenia. In addition, the delineation of ROIs is a time-consuming task that requires skilled professionals and the use of dedicated software. Consequently, although accuracy is reduced, it is more common to apply generic ROI templates (Koole *et al* 2001, Rojas *et al* 2007), even in research centres.

Standard ROIs

To reduce operator intervention, current clinical guidelines recommend that functional images are normalised to a standard space before quantification. The main advantage of incorporating a normalisation step into the quantification procedure is that it allows a unique template of ROIs to be defined in a standard space. This standard template can then be used to quantify all the normalised studies, simplifying and speeding up the quantification process. The application of this template of ROIs can be done directly or with the final intervention of the operator or some software that adjusts the ROIs to each study. Normalisation modifies the anatomy of the study so that it matches the template whilst preserving

the activity distribution of the brain structures. So semi-quantification results are not modified by this technique.

Specially-designed software packages for the analysis of brain imaging data such as SPM (Statistical Parametric Mapping; Wellcome Trust Centre for Neuroimaging) come with standard templates for several modalities of anatomical and functional imaging. Templates are usually defined in the MNI standard space, which was defined by the Montreal Neurologic Institute. Automated Anatomical Labelling (AAL) is a standardised anatomical ROI map defined in the MNI standard space that provides generic templates for all brain structures (Tzourio-Mazoyer *et al* 2002).

Nevertheless, some institutions and research centres choose to create their own templates using scans of their own control subjects. This procedure requires a MR image and a SPECT study of each normal control. The creation of the template starts with the coregistration of the MR and SPECT images. Then, the coregistered images are normalised to a standard space, usually the one defined by MNI. Generally, MR images are normalised to the T1-weighted template and the same transformations are applied to the SPECT images. Finally, the normalised images from the same technique (MRI and SPECT, separately) are summed together and averaged out. The result is usually smoothed by the application of a Gaussian filter. Home-made MRI and SPECT templates can then be used to define the template of ROIs.

Advanced semi-quantification methods usually incorporate a registration algorithm to normalise the studies to the standard space before applying the predefined template of ROIs. The template of ROIs can be based on anatomical maps (such as the AAL map) or may consist of a predefined location of geometrical ROIs (frequently circular) in a few consecutive transaxial slices. Slices may be selected visually as representing the most active areas of the striatum or by identifying the slice with maximum counts and adding a number of slices either side of it. There is no width considered as globally standard and typical values used by institutions can vary from around 10 to 30 mm (Walker *et al* 2002, Varrone *et al* 2004).

The main drawback of these techniques lies in the limitations inherent in the normalisation process. The application of a 3D pre-filtering to the studies is recommended in order to smooth the images and facilitate normalisation. However, some studies may require additional programming to ensure accurate normalisation, such as those with low uptake ratios, or where anatomically pre-

defined ROIs such as the AAL map are used. Anatomical differences between predefined anatomical ROIs and the real structures can cause inaccurate quantifications. In spite of the complexity of this technique, normalisation of studies to a standard space before applying the template of ROIs is becoming mandatory in leading centres.

Problems derived from semi-quantification: need of standardisation

In clinical routine, the interpretation of the quantitative information elicited from the image is based on its comparison with those values obtained with age-matched normal controls. The main advantage of using relative quantification is that there is no need to correct for those effects that will in the main be cancelled out in the comparison. However, this only occurs when the same type of scanner, acquisition protocol, reconstruction parameters and quantification procedure are used to obtain the values of the reference normal database. Thus, those reference values are not standard and cannot be transferred to other centres.

As mentioned above, results provided by semi-quantification methods are dependent on the imaging system and acquisition protocol, the corrections applied for the degrading phenomena and the quantification procedure (size and morphology of the ROIs, selected slices, location of the ROIs, image registration, etc.). This dependence is of enormous importance since it prevents the creation of a single unambiguous standardised database that would help differentiate between known diseases and their states. The lack of a single standard database forces nuclear medicine centres to create their own local normal databases. But to obtain standardised values, somehow all the degrading effects need to be compensated for in order to recover the true ratios corresponding to the original activity distribution in the patient (El Fakhri *et al* 2001, Soret *et al* 2003).

As an alternative to the arduous task of correcting all the degrading effects study by study (as is done in absolute quantification), standardised values may be obtained if a direct relationship between the calculated results and the real values could be established. To calculate the standardising function, anthropomorphic brain phantoms could be used since the true activity distributions are known. To make this standardisation possible, the anthropomorphic phantom should follow the same nuclear imaging protocol as patients and should be shown to be representative of the average anatomy of the population. The main drawback of this technique is the fact that calculated values would be standardised according to

a function defined for the particular anatomy of the phantom. Thus, significant errors could occur in those patients with large anatomical differences with respect to the phantom.

3.5 Monte Carlo simulation in SPECT

Monte Carlo (MC) simulation is a statistical simulation method based on random numbers generated according to the dynamics of the system under study. MC simulation is applied to those problems which can be globally described by probability density functions. The physics of radiation emission, transport and detection makes MC simulation the appropriate tool for modelling SPECT imaging and other nuclear medicine techniques (Zaidi 1999, Buvat and Castiglioni 2002, Rogers 2006, Buvat and Lazaro 2006).

MC simulation in emission tomography is applied to the design and selection of gamma cameras and their components (Lupton and Keller 1983, Bradshaw *et al* 1985); modelling of the detector system response (PSF) (Du *et al* 2002, Cot *et al* 2004, Staelens *et al* 2007); modelling of the spatial and energy distribution of Compton scatter (Cot *et al* 2002; Zaidi and Koral 2004); the study of the effect and contribution of each image degradation (Crespo *et al* 2008); the design and assessment of image-degrading compensation methods (Ljungberg and Strand 1990) and the design and evaluation of quantification protocols (Cot *et al* 2005). Since the original activity distribution of the source is known, MC simulation permits the testing of semi-quantification methodologies using a variety of anatomical and tracer uptake cases that would be almost impossible to reproduce otherwise. Thus, MC simulations allow the reliability of applied methodologies to be confirmed and identify any inherent errors in the method used.

3.5.1 Monte Carlo codes for emission tomography

Depending on the specificity of its application, MC codes for particle transport are classified into general purpose codes and dedicated codes. General purpose codes are more flexible and, in general, provide more detailed simulations. On the other hand, dedicated codes for SPECT focus on the relevant aspects for the emission tomography omitting those which are not relevant for the application. As a result, they are often faster and easier to program by the user.

General purpose codes available for nuclear medical applications are: EGS4 (Murray 1990), MCNP (MCNP directory), PENELOPE (PENELOPE home page), ITS (Halbleib *et al* 1992) and GEANT (GEANT4 home page). Dedicated MC packages for SPECT are: SIMIND (Ljungberg and Strand 1989), SimSPECT (Belanger *et al* 1998) and MCMATV (Smith *et al* 1993). Among the most frequently used codes for both SPECT and PET simulations are GATE (Yanch *et al* 1992) and SimSET (Haynor *et al* 1991). Basically, these codes differ on the energy range of the simulated particles, the physical models and approximations applied to describe interactions, the geometric limitations in the definition of the bodies and sources, and the interface with the user.

In this doctoral dissertation, SimSET was used to simulate SPECT projections after introducing some improvements into the code.

3.5.2 SimSET

Simulation System for Emission Tomography (SimSET) is a dedicated MC code for the simulation of the physical processes and the instrumentation used in SPECT and PET. SimSET was developed in 1993 at the Imaging Research Laboratory at the University of Washington for public distribution to Nuclear Medicine research centres and it runs on a wide range of computer platforms. It is a fast code that considers the specific parameters of a SPECT acquisition, such as the number of projections, the number of counts, the radius of rotation, the field of view, the energy window and the pixel size among other variables.

The code must be provided with an image of the distribution of the radiation source (activity map) as well as of the tissues or materials that surround it (attenuation map). In order to characterise the collimator, the description of its main features must be specified: septal thickness, hole size and focal distance for fan-beam collimators. One interesting point is that this code allows discrimination of the different components of the resulting projections into scattered and unscattered photons. In addition, it allows the introduction of some modifications to the code so as to improve it.

Like other dedicated MC simulators, SimSET uses analytical functions to accelerate the tracking process through the collimator/detector system. The task would otherwise require intensive computational processes that make it impossible to complete in a reasonable time using current computers. These analytical functions

calculate the probability of detection through the collimator/detector system for each photon and are based on PSF responses.

PSF model for low-energy photons

The collimator response originally implemented in SimSET was based on a PSF model developed for low-energy photons (Metz *et al* 1980, Tsui and Gullberg 1990, Frey *et al* 1998) which only took into account the geometric component of the PSF. As this model presents some inaccurate hypotheses (see Cot 2003 for a detailed analysis), our group decided to develop a new PSF model after a MC study.

In Cot *et al* 2002, a complete characterization of a fan-beam collimator response to ^{99m}Tc point sources was carried out using the MC code PENELOPE (PENELOPE home page). MC simulation was performed using a detailed representation of the hexagonal shape of the holes of the collimator as well as its pattern. All the collimator effects were carefully simulated. In order to differentiate contributions to the final PSF, each photon reaching the detector layer was flagged according to its past interactions as either geometric photons (no interaction suffered and no septa crossed), septal penetration (no interaction, one or more septa crossed), photons that underwent deflection due to a coherent interaction without energy loss (Rayleigh) or photons that underwent deflection due to an incoherent interaction with energy loss (Compton). Detector effects were not included in the simulations. Figure 3.9 shows the four components of the PSF for a ^{99m}Tc point source.

As a result of this study, it was found that the major contribution to the fan-beam PSF was the geometric component, *i.e.* the geometric pattern of the holes of the collimator, which represented approximately 95.1% of the total PSF. Septal penetration was the second major contribution with 3.7%. Rayleigh photons had a contribution of 1.1% and the Compton interaction was 0.1%. These results were in accordance with those obtained by De Vries (De Vries *et al* 1990) with a parallel collimator. Thus, a complete collimator/detector response could be obtained by convolving only the geometrical PSF with the intrinsic response of the detector. The result was fitted to a Gaussian function with a high correlation coefficient.

This work demonstrated that ray-tracing techniques that allow calculating the geometrical component of the PSF are good enough to model the PSF for low-energy photons (Pareto *et al* 2002).

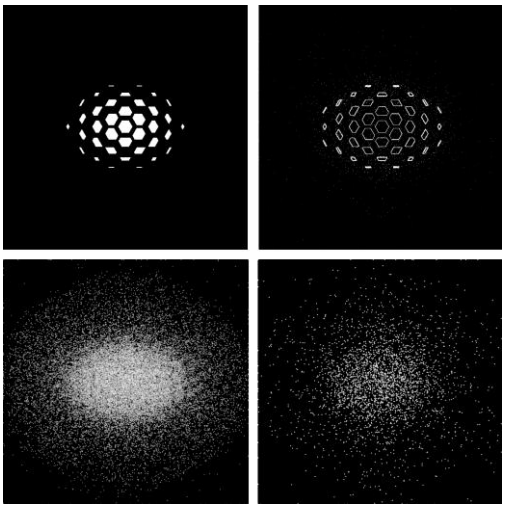

Figure 3.9 PSF components for a ^{99m}Tc point source located at 10 cm from the collimator front plane: geometric component (top left), septal penetration (top right), coherent scatter (bottom left) and incoherent scatter (bottom right).

Thus, our group replaced the original PSF model of SimSET (Frey *et al* 1998) with a more accurate PSF model developed in-house using ray-tracing techniques (Pareto *et al* 2002). In this model the sensibility of the collimator, *i.e.* the amplitude of the Gaussian function, was modelled as:

$$\eta(Z_s, \cos\theta) = k_1 \frac{F+L}{F-Z_s} cos^2\theta \qquad (3.5)$$

Where F is the focal length, L is the thickness of the collimator and Z_s is the distance between the source and the collimator. θ is the source aperture angle, which is the angle between the normal to the collimator and the straight line that joins the source point and its interaction point with the detector. k-constants are parameters that have to be fitted to experimental or simulated data.

The resolution, *i.e.* the standard deviation of the Gaussian function, on the x-axis, which is the direction in which the fan-beam collimator amplifies the image, was modelled as:

$$\sigma_x(Z_s, \theta) = k_{2,x} \frac{R(Z_S+L+B)(2F+L)}{\sqrt{L^2(F-Z_S)^2 - R^2(L+2Z_S)^2}} \frac{1}{cos\theta} \quad (3.6)$$

And on the y-axis:

$$\sigma_y(Z_s) = k_{2,y}\frac{2R(Z_S+L+B)}{L} \quad (3.7)$$

Where B is the distance between the back collimator face and the image plane and R is the distance between the centre and the vertex of the hole.

The parallel collimator is a particular case of the fan beam collimator where the focal distance is infinite.

The intrinsic resolution of the detector is known to follow a Gaussian distribution. The standard deviation of this distribution can be obtained from experimental measurements and convolved with the collimator response.

Given the similar behaviour between the low-energy line from ^{123}I and photons emitted by ^{99m}Tc, the PSF model for low-energy photons is also suitable for ^{123}I low-energy emission.

PSF model for high-energy photons

The photon emission of ^{123}I is dominated by a low-energy line of 159 keV (97%) but it also emits several high-energy lines at 248 (0.08%), 281 (0.09%), 346 (0.15%), 440 (0.50%), 505 (0.37%), 529 (1.62%), 538 (0.44%), 624 (0.10%) and 783 (0.07%). Please note that only those rays with a yield larger than 0.06% have been listed. Low and high-energy photons generate very different responses in the gamma camera that need to be modelled separately.

As it has been previously shown, the deterministic modelling of the PSF is accurate enough at low-energy ranges. At higher energies, the non-geometric effects turn out to be non-negligible and thus, the geometrical model is no longer valid. All the interactions that take place at the backscatter compartment of the detector (optical guide, photomultipliers, electronics, electric wires, shielding materials, etc.) cause high-energy photons emitted by ^{123}I to lose part of their energy and make a non-negligible contribution to the projections. For the highest yields emitted, *i.e.* 440, 505, 529 and 538 keV, the backscatter peaks are 162, 170, 172 and 173 keV, respectively. Thus, they all fall within the detection window centred on 159 keV (Dobbeleir *et al* 1999, Cot *et al* 2004, Staelens *et al* 2007).

Taking a similar approach to that developed by Cot *et al* 2002 for the study of the PSF for low-energy photons, in Cot *et al* 2006 our group used PENELOPE to simulate the high-energy lines of ^{123}I with yields higher than 0.1%, *i.e.* 346, 440, 505, 529 and 538 keV. High-energy lines were simulated as isotropic sources located at different distances from a LEHR fan-beam collimator and at different off-axis positions. Since the collimator geometry was formed by approximately 40.000 hexagonal holes, the simulation was simplified by considering one single hole whose position and geometry varied *on the fly*, according to the location of the photon tracked. The backscatter compartment was simulated as a single layer of Pyrex since the characteristics of the backscatter phenomena were found to be better reproduced using this material than others such as iron or copper (De Vries *et al* 1990, Cot *et al* 2004). The thickness of the layer was selected to match with the sensibility of the experimental measurements. MC simulations were validated against experimental measurements using ^{18}F-FDG point sources emitting photons of 511 keV.

Results showed that PSF for high-energy photons extends over the whole field of view (FOV) and it can be modelled using the following Gaussian function:

$$g(x,y) = A \cdot exp\left\{-\left[\left(\frac{x-x_0}{b_x}\right)^2 + \left(\frac{y-y_0}{b_y}\right)^2\right]\right\} \quad (3.8)$$

where x and y are Cartesian coordinates on the collimator front plane and the parameters A, b_x and b_y depend on the energy and location of the source (x_0, y_0).

Probability density functions (PDF) were generated by our group to characterize the following gamma cameras: Elscint HELIX equipped with a LEHR fan-beam collimator (Cot *et al* 2006), Siemens E.CAM with a LEHR parallel-hole collimator (Crespo *et al* 2008), and Picker PRISM 3000 S with a LEHR fan-beam collimator (Roé 2011). PDF describes the response of the collimator/detector system and is based on the modelling of the PSF.

Chapter 4

4 Validation of SimSET for ^{123}I SPECT studies of the dopaminergic system

4.1 Introduction

SPECT images allow the study of the dopaminergic system using radiopharmaceuticals labelled with ^{123}I. As mentioned in chapter 3, the original SimSET MC code included a PSF model that was valid for low-energy photons but not appropriate for the high-energy photons emitted by ^{123}I with energies above 200 keV. The contribution of the high-energy photons to the projections comes from the scattering and penetration effects that high-energy photons undergo within the collimator and, especially, in the backscatter compartment of the detector (Cot *et al* 2004, Rault *et al* 2011), which causes them to lose part of their energy and thus fall within the energy window. As this can result in inaccurate simulations (De Vries *et al* 1990, Dewaraja *et al* 2001) which are unacceptable for most applications, our group developed a PSF model for the high-energy emission of ^{123}I after a detailed MC simulation study (Cot *et al* 2006).

Once the PSF model for high-energy emission had been defined, PDF functions for different collimator configurations were generated by our group and incorporated into the collimator module of SimSET. PDF functions are dependent on the energy

and on the location of the source. With the inclusion of these functions, the new version of SimSET calculates "on the fly" the probability of detection at the bin hit by the photon. This probability is calculated as the integral of the PDF over the projection bin. PDF is considered to be centred at the intersection of the backplane of the collimator with the perpendicular line from the point of the last interaction of the photon to the focal line. The probability of detection is calculated for all available collimator views. This methodology speeds up the simulation with respect to other approaches such as those based on angular response functions (ARF) (Song *et al* 2005). ARF functions are dependent on the energy and the direction of the incident photon. They store the probability that the incident photon passes through the collimator and is detected within the energy range, at the intersection point of the photon direction vector and the detection plane. These functions are applied as a post-processing of all the photon histories calculated by SimSET within the object.

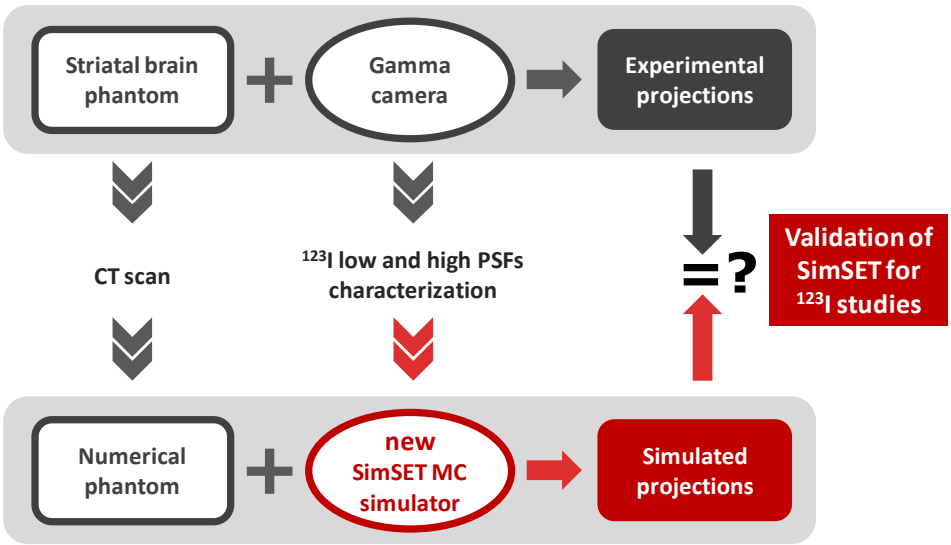

Figure 4.1 Scheme of the methodology applied to validate the new version of SimSET for ^{123}I SPECT studies.

This chapter covers the experimental validation of the new version of SimSET for the simulation of ^{123}I SPECT studies using a Picker PRISM 3000 S equipped with a LEHR fan-beam collimator. Validation was performed by comparing the experimental projections obtained from an anthropomorphic striatal phantom using the Picker PRISM system and the simulated projections obtained from a numerical phantom derived from this striatal phantom by applying the new version

of SimSET. This version included the PDF functions previously obtained for this collimator/detector system. The scheme of the approach is shown in figure 4.1 and developed in the following sections.

4.2 Materials and methods

4.2.1 Experimental projections

Striatal brain phantom

The anthropomorphic striatal brain phantom (Radiology Support Devices, RSD. Inc, Long Beach, CA) was used to mimic real SPECT studies with ^{123}I-labelled pharmaceuticals (see figure 4.2).

This phantom consists of five compartments which correspond to the left and right caudate nuclei and putamen, and the rest of the brain. All these structures have a normal human brain shape and size, and are surrounded by two different materials which are equivalent to soft tissue and bone.

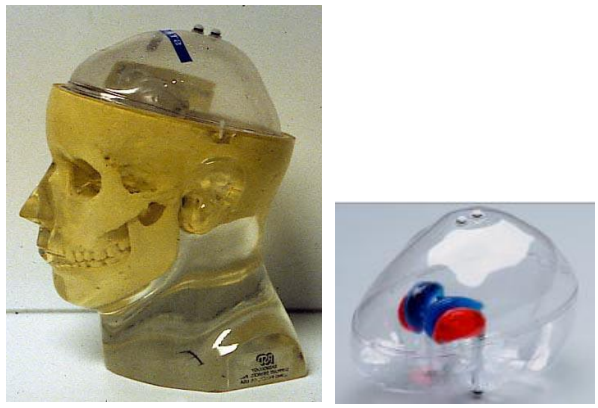

Figure 4.2 The anthropomorphic striatal brain phantom.

Data acquisition

Experimental projections of the striatal brain phantom were acquired using a Picker PRISM 3000 S gamma camera equipped with a LEHR fan-beam collimator (see figure 4.3). The main parameters of the imaging system are summarised in table 4.1.

The four compartments of the striatum of the phantom were filled with the same activity concentration. Radiotracer distributions corresponding to SUR values of 0.00, 1.97, 3.73 and 6.63 were considered so as to cover a range of normal and pathological distributions. 120 projections over 360° with a 20% energy window centred on 159 keV (143-175 keV) were acquired. A 128x128 matrix with a bin size of 3.55 mm was selected. The radius of rotation was set to 14.5 cm. All experimental studies were set to have more than 2.5 million counts. To statistically assess the influence of noise, acquisitions were repeated consecutively six times for each SUR value. Finally, the set of studies corresponding to each SUR value were normalised to the number of counts of the first acquisition.

Figure 4.3 Acquisition of the experimental projections of the striatal brain phantom with the Picker Prism 3000 S gamma camera.

Table 4.1 Parameters of the PRISM SPECT system

Parameter	PRISM SPECT system
Collimator	LEHR fan-beam
Focal length (mm)	650
Hole shape	Hexagonal
Hole radius (mm)	0.86
Septal thickness (mm)	0.15
Length (mm)	27.00
Crystal thickness (mm)	9.50
Crystal material	NaI

4.2.2 Simulated projections

The modified SimSET simulator

Simulated projections were generated using the new version of the SimSET code. In this version, SimSET was modified by the inclusion of the high-energy PDF functions calculated for the Picker imaging system. These functions allow acceleration of the MC simulation by calculating the probability of detection through the collimator/detector system for each photon.

The adjustments of the PDF functions for the high-energy emission of ^{123}I were incorporated into the collimator module of SimSET in the form of look up tables. These tables were previously calculated using the MC code PENELOPE and then included in SimSET.

Look up tables are dependent on the collimator/detector configuration and on the isotope, and contain the values of the parameters A, b_x and b_y from equation (3.8). Since these parameters are dependent on the energy and on the location of the source (x_0, y_0) a selected number of energies and locations were considered. In particular, values were calculated for the energy lines with yields higher than 0.1%, *i.e.* 346, 440, 505, 529 and 538 keV, located at 5, 10, 15, 20 and 25 cm from the collimator front plane. When the simulated photon in SimSET does not have any of the energies considered and/or it is not located at any of the positions considered, the parameters A, b_x and b_y are calculated by applying an interpolation of energies and/or locations. PDF look up tables were incorporated into the new version of SimSET together with the geometric PSF model developed for low-energy photons.

SPECT projections were simulated using a simplified emission model which considers that all the high-energy lines from ^{123}I are equivalent to one single line of 529 keV with a yield of 3% (Roé 2011).

Numerical phantom

A computed tomography (CT) scan of the anthropomorphic striatal brain phantom was acquired to create the numerical phantom for the simulation. The CT image had 256x256x196 voxels, with a voxel size of 0.89x0.89x0.89 mm^3. The attenuation map was generated by segmenting the CT image into brain tissue and bone using an intensity threshold. The activity map was defined by manually drawing the striatal

cavities over the corresponding slices. Maps were selected to have 80x80x64 voxels, 3.56x3.56x3.56 mm^3. In order to guarantee the same orientation as in the experimental study, the attenuation and activity maps were coregistered with the experimental studies reconstructed with FBP.

MC simulation of the projections

Simulated projections were generated using the modified SimSET code with the same parameters as those used for the experimental acquisitions. The simplified ^{123}I emission model was applied, *i.e.* 97% of photons with 159 keV and 3% of photons with 529 keV. Since the linear attenuation coefficients are dependent on the energy of the simulated photons, the coefficients of the attenuation map were different for the simulation of low and high-energy emissions.

A very high signal-to-noise ratio simulation was carried out for each experimental SUR value. To this end, MC simulation was performed to obtain a variance one hundred times lower than the total counts in projections. Thus, these projections could be considered to be noise-free. Each study took approximately 3 hours in a processor with 3.2 GHz clock speed. Finally, counts obtained in the simulated projections were compared with the mean counts of the six consecutive experimental projections.

4.3 Results and discussion

Figures 4.4 and 4.5 show the experimental and simulated profiles for a set of several representative projections (front, lateral left, back and lateral right projections) and for two of the considered SUR values. Figures 4.6 and 4.7 show the corresponding profiles of one selected row of the aforementioned projections. The row was selected to include the striatal nuclei. Experimental results are represented by the mean value found for the six acquisitions made and by the error bar corresponding to one standard deviation. The simulated profiles are represented by the value found for each projection bin. Similar profiles were obtained for the remaining projections and SUR values.

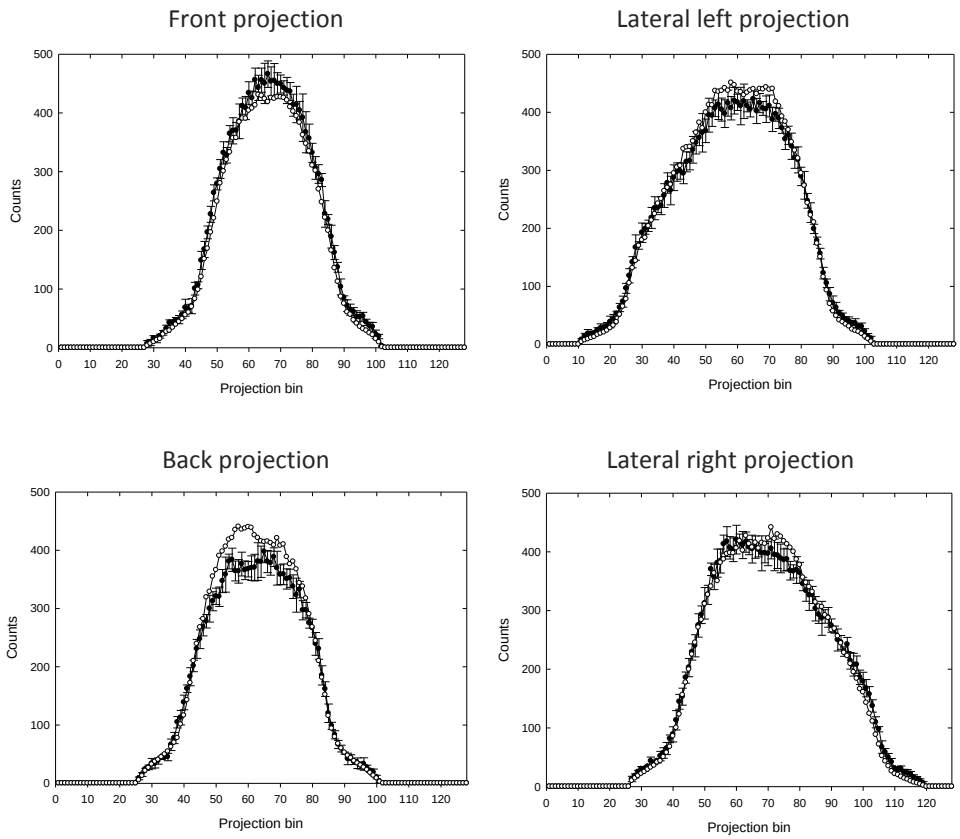

Figure 4.4 Experimental (black circles) and simulated (white circles) profiles of projections of the striatal phantom for a SUR value of 0. Experimental values are represented as the average value of the six acquisitions and by the error bar corresponding to one standard deviation.

Results show that the simulated curve follows the experimental within the error interval for almost all projections. This behaviour is also observed in the results corresponding to the row that contains information of the striatum.

Differences found for those projections that correspond to the view of the back of the phantom can be explained by the attenuation caused by the head-holder. Since the simulation does not include this device, experimental and simulated profiles diverge in those projections that are most affected by the head-holder for all SUR values. So, when part of the head-holder is located between the phantom and the detector, the simulated profile would be above the experimental values.

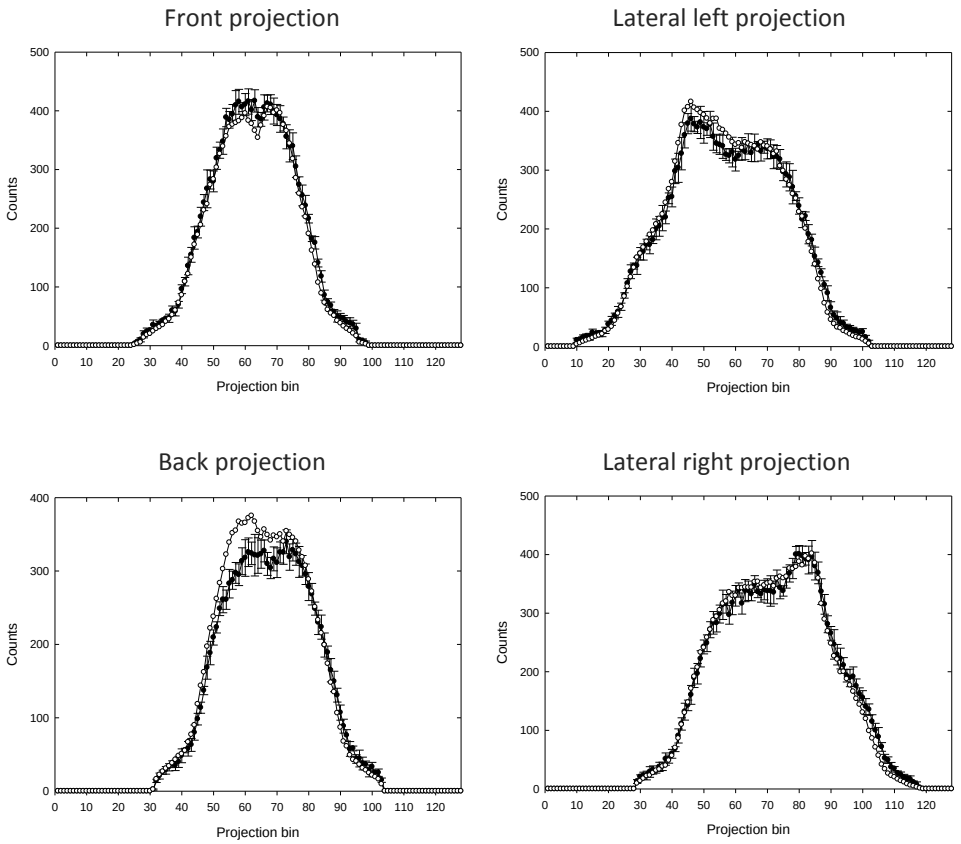

Figure 4.5 Experimental (black circles) and simulated (white circles) profiles of projections of the striatal phantom for a SUR value of 6.63. Experimental values are represented as the average value of the six acquisitions and by the error bar corresponding to one standard deviation.

In order to compare the projections quantitatively, the root mean square deviation (RMSD) was used to estimate the difference between simulated and experimental pairs of images. This parameter is defined as follows:

$$RMSD = \sqrt{\frac{1}{N}\sum_{i=1}^{N}(S_i - O_i)^2} \qquad (4.1)$$

Where S_i and O_i are the i-th bin values of the simulated and experimental projections, respectively.

RMSD values found for each considered SUR are shown in table 4.2. These values indicate the mean deviation in the number of counts in each bin between experimental and simulated projections.

Table 4.2 RMSD values found for each considered SUR

SUR	RMSD
0.00	1.48
1.97	1.30
3.73	1.30
6.63	1.28

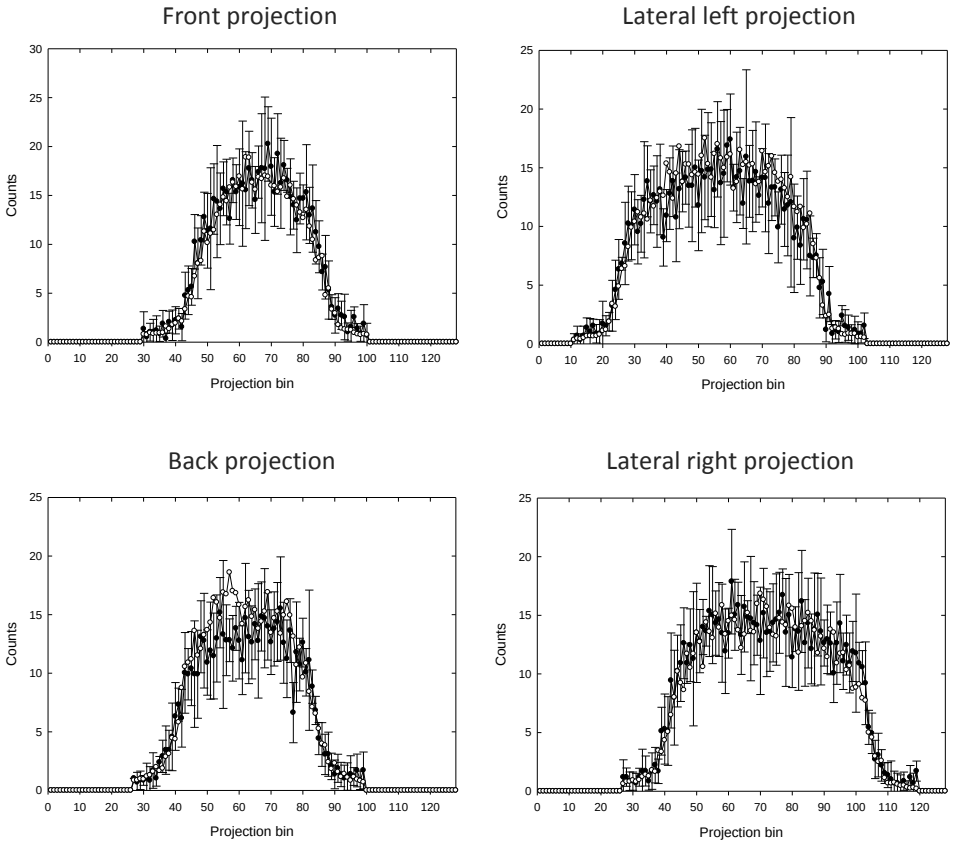

Figure 4.6 Experimental (black circles) and simulated (white circles) profiles corresponding to one row of the projection for a SUR value of 0. Experimental values are represented as the average value of the six acquisitions and by the error bar corresponding to one standard deviation.

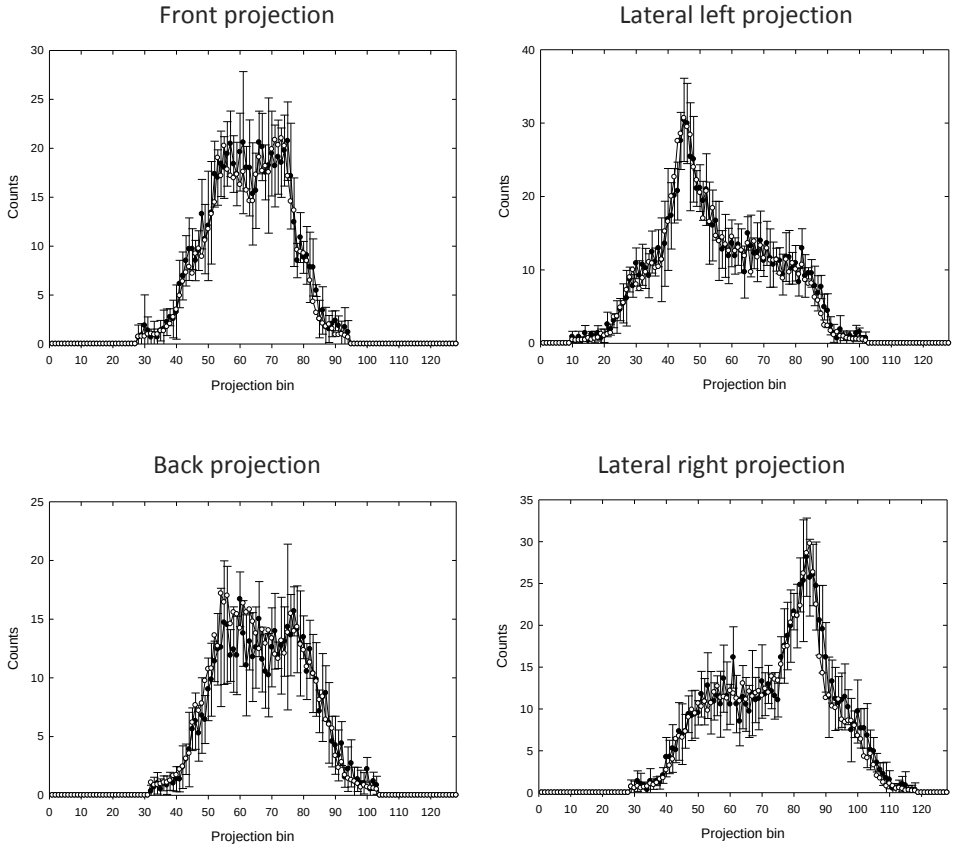

Figure 4.7 Experimental (black circles) and simulated (white circles) profiles corresponding to one row of the projection for a SUR value of 6.63. Experimental values are represented as the average value of the six acquisitions and by the error bar corresponding to one standard deviation.

As it can be observed, the calculated RMSD values for all SURs are remarkably similar, all falling in the range of 1.3-1.5. These values indicate that the differences between simulated and experimental projections are negligible. In fact, these differences are lower than those found between two experimental acquisitions corresponding to the same SUR. It should be remembered that the experimental acquisitions for each SUR value were performed successively, without modifying any parameter of the imaging system. Thus, experimental acquisitions were essentially not affected by any additional noise other than statistical noise. In addition, comparison is performed between the mean value of the six consecutive experimental acquisitions (once normalised to the number of counts of the first study) and the profile given by the very high signal-to-noise ratio simulation. Thus,

the effect of noise in this comparison is certainly low so as to ensure that RMSD values are primarily a result of the simulation model applied.

4.4 Conclusions

This work confirms that the PDF functions incorporated into the collimator module of SimSET, make this code a reliable and accurate tool for the simulation of SPECT studies of the dopaminergic system using ^{123}I.

Chapter 5

5 Absolute quantification of dopaminergic neurotransmission SPECT studies with ^{123}I for research trials

5.1 Introduction

Several methodologies have been proposed to correct the non-desirable effects that degrade SPECT images and impair accurate quantification such as attenuation and PSF (El Fakhri *et al* 2001, Pareto *et al* 2003), scatter (Hutton *et al* 2011) and the partial volume effect (PVE) (Soret *et al* 2003). In 2005, our group at Hospital Clínic of Barcelona (Barcelona, Spain) developed a complete method named Absolute Quantification Method (AQM) for the accurate quantification of dopaminergic neurotransmission SPECT studies obtained using ^{99m}Tc-labelled radioligands (Cot *et al* 2005). This method performed a fully 3D iterative reconstruction with attenuation and PSF corrections and included a MC-based scatter compensation.

Since SPECT imaging makes most use of ^{123}I-labelled radioligands, an extension of the previous AQM was needed to adapt this method to the particularities of ^{123}I photon emission. As previously seen in chapter 3, in ^{123}I SPECT imaging, the

contribution from high-energy photons (above 200 keV) is not negligible, because the backscatter peaks of these emission lines fall well inside the detection window (Cot *et al* 2004, Du *et al* 2006). This so called high-energy contamination needs careful attention because, while in the decay scheme of this radioisotope the high-energy yield is low (~3%), its contribution to the total counts in the projections may be important. So AQM was modified to include a MC-based scatter compensation for the effect of the high-energy photons in ^{123}I SPECT studies. Given its significance, the method was also provided with a handy post-reconstruction compensation for PVE.

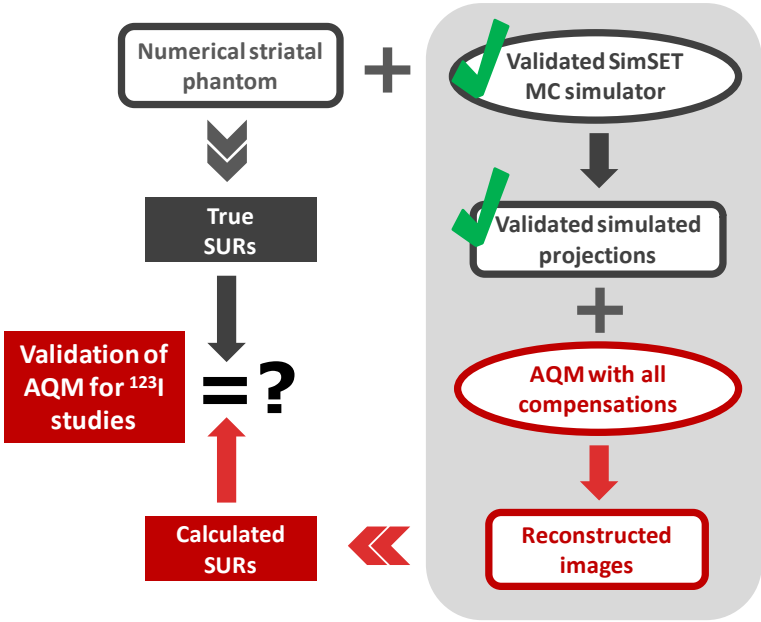

Figure 5.1 Scheme of the methodology applied to validate AQM for ^{123}I SPECT studies.

The new version of AQM was tested using two different imaging systems equipped with a parallel and a fan-beam collimator, given that both types of collimator are regularly used in ^{123}I neurotransmission SPECT imaging (Darcourt *et al* 2010, van Laere *et al* 2010).

The new version of the SimSET MC code was used to generate the projections. Thus, quantitative results could be compared with the true values to evaluate their reliability and accuracy. Ideally, quantitative values provided by AQM should be similar to those extracted from the activity maps that were used to generate the

projections. Moreover, quantitative values should be similar for both imaging configurations after correcting for all degradations. The scheme of this approach is shown in figure 5.1.

5.2 Materials and methods

5.2.1 Numerical phantom

Simulated projections were generated by using the numerical phantom obtained from a CT scan of the anthropomorphic striatal brain phantom shown in figure 4.2. The CT scan consisted of 256×256×196 cubic voxels with a voxel size of 0.89×0.89×0.89 mm^3. Brain tissue and bone were automatically segmented by thresholding the CT image, while the striatal cavities were manually drawn over the corresponding slices.

The attenuation map was obtained by setting the appropriate attenuation coefficients to brain and bone. The value of these coefficients was changed according to the energy of the simulated photons, *i.e.* low and high-energy emissions. Thirty different activity distributions were considered with SUR values which modelled normal and pathological distributions of ^{123}I-FP-CIT. The striatum was considered to have uniform activity distribution and tracer uptake was considered to be the same in caudate and putamen. Figure 5.2 shows a central slice of the activity and the attenuation maps used in the simulations.

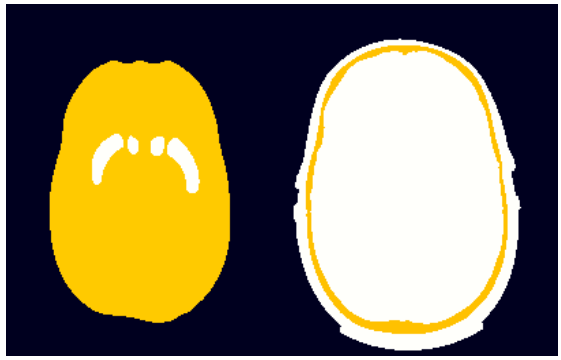

Figure 5.2 A central slice of the activity (left) and attenuation (right) maps derived from the anthropomorphic striatal brain phantom.

5.2.2 Simulated projections

The new version of the SimSET MC code for the simulation of ^{123}I SPECT studies (see chapter 4) was used to simulate the projections of the following two imaging systems: Siemens E.CAM with LEHR parallel-hole collimator and Elscint HELIX with LEHR fan-beam collimator. Low-energy photons with 159 keV and a yield of 97% and high-energy gamma-rays with 529 keV and a yield of 3% were simulated separately, following the simplified emission model shown in chapter 4. Finally, the generated projections for the low and high-energy emissions were added together to obtain the total projections.

Table 5.1 summarises the simulation parameters used for both imaging systems. The differences in the setting that can be observed are due to the different acquisition protocols used for each gamma camera. Energy windows were selected according to the values proposed by the manufacturers.

Table 5.1 Simulation parameters used with each SPECT system.

Parameter	E.CAM system	HELIX system
Collimator	LEHR parallel-hole	LEHR fan-beam
Focal length (mm)	NA	355
Hole shape	Hexagonal	Hexagonal
Hole radius (mm)	0.641	0.866
Septal thickness (mm)	0.16	0.20
Length (mm)	24.05	40.00
Number of projections	128	120
Matrix size	128×128	128×128
Bin size (mm)	3.900	4.424
Energy window (%)	15	20
Radius (mm)	150	150

A total of 30 real-noise projections for each SPECT gamma camera were generated by employing the randomly distributed values of SUR ranging from 0.1 to 6. All the simulated studies were considered to have approximately 3 million counts, thus mimicking real studies obtained with these two imaging systems.

5.2.3 Reconstruction algorithm

AQM for ^{123}I SPECT

AQM is an iterative reconstruction algorithm based on OSEM which performs a fully 3D-reconstruction with attenuation and PSF corrections and includes a MC-based scatter compensation. In AQM, the voxel values λ_i of the reconstructed image are updated in each step of the reconstruction process using the expression:

$$\lambda_i^{k+1} = \frac{\lambda_i^k}{\sum_{j=1}^{nbin} t_{ji}} \cdot \sum_{j=1}^{nbin} \frac{t_{ji} \cdot p_j}{\sum_{m=1}^{nvox} t_{jm} \cdot \lambda_m^k + S_j} \qquad (5.1)$$

Where λ_i^k is the image estimation at iteration k; t_{ji} represents the transition matrix; p_j represents the original projections; $\sum_m t_{jm} \cdot \lambda_m^k$ is the projection bin j after forward projection of the image estimation at iteration k; and S_j is the scatter contribution estimated in bin j.

Thus, the estimated scatter distribution is used in the denominator of the OSEM algorithm as a constant additive term in the forward projector equation (Bowsher and Floyd 1991). The transition matrix incorporates the modelling of attenuation and the geometric component of the PSF for low-energy emission which can, therefore, be corrected in the back-projection.

As regards scatter, its contribution is calculated as:

$$S_j = S_j^{LE} + S_j^{HE} \quad (5.2)$$

Where S_j^{LE} and S_j^{HE} are the low and high-energy photons which have undergone scattering and have been finally detected.

Figure 5.3 shows the scheme of the reconstruction algorithm. Firstly, the original projections are reconstructed without scatter compensation ($S_j = 0$) at loop 0. Then, the reconstructed image at loop 0 is used as the input activity map of the SimSET MC simulator to estimate the scatter distribution. The image at the first iteration is the one selected as the input activity distribution of the SimSET simulator. Photon emission is weighted according to the emission yields of the low (97%) and high-energy photons (3%), which are simulated separately.

SimSET simulates scatter phenomena in the object but to accelerate the process, scatter in the collimator/detector system is modelled using the analytical models based on the low and high-energy PSF described in chapter 3. The scatter estimate is generated only once. A high signal-to-noise ratio scatter distribution is estimated to facilitate convergence (Beekman *et al* 1997). Once calculated, the scatter distribution is included in equation (5.1). As the scatter fraction is included in the forward projector, scatter correction does not remove counts from the original projections and so noise is not increased after scatter correction.

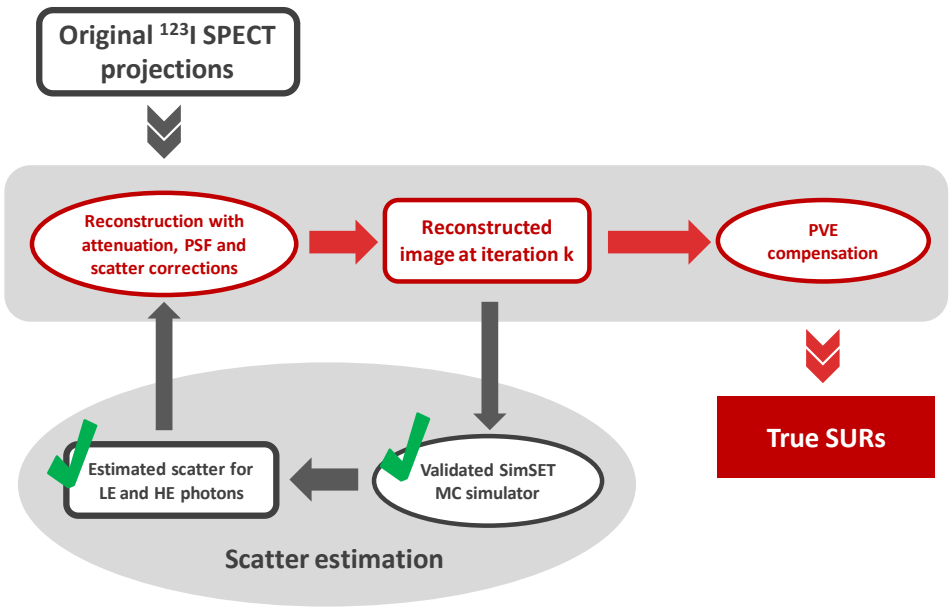

Figure 5.3 Scheme of the AQM method.

Reconstruction of the simulated projections

Table 5.2 summarises the reconstruction parameters used for each imaging system. Given that the convergence of the reconstruction process is not the same for the two SPECT systems, the number of iterations needed for each camera was different. An additional iteration was calculated whenever the recovered SUR values increased at least by 1%. Projections had to be filtered with masks before reconstruction because of high-energy contamination. Thus, the values located outside the field of view of the phantom were discarded to prevent them from interfering in the reconstruction process. Masking was performed by applying a geometric projector to the attenuation map and giving a value of 1 inside the resulting projections and 0 outside their limits.

Table 5.2 Reconstruction parameters used with each SPECT system.

Parameter	E.CAM system	HELIX system
Pixel size (mm)	2.296	2.296
Slice thickness (mm)	3.900	4.424
Image size	128×128	128×128
Number of slices	45	40
Number of subsets	32	30
Number of iterations	8	6
Reconstruction time per study (h)	2	2

5.2.4 Quantification with PVE compensation

The partial volume effect

As seen in chapter 3, accurate quantification in SPECT is impaired, *inter alia*, by the different non-desirable effects that affect acquisition, degrading the contrast and resolution of the SPECT images. In addition to these phenomena, reconstructed images present the so called partial volume effect (PVE).

PVE manifests as an underestimation of the activity in small high-activity structures, such as caudate and putamen, due to the finite spatial resolution of the SPECT technique. PVE causes part of the activity from a certain structure to spill over to adjacent regions, distorting the true activity distribution in all regions. PVE is a major source of bias in SPECT neuroimaging (Soret *et al* 2007) and it may be boosted during the quantification process as a result of segmentation, coregistration and normalisation processes.

Due to the strong influence of PVE on the quantitative results, a number of PVE correction methods have been developed in parallel by different research groups (Rousset *et al* 1998, Frouin *et al* 2002, Bullich *et al* 2004, Quarantelli *et al* 2004, Du *et al* 2005, Vanzi *et al* 2007).

With the aim of minimizing its effect, some techniques apply small ROIs in the most active areas of the striatum, where the influence of PVE is lower. One example is the simple methodology based on cylindrical ROIs applied to a selected number of slices (Varrone *et al* 2004, Zubal *et al* 2007) and which is widespread in clinical routine. Other methods use large ROIs to cover the whole striatum and account for all the counts that have blurred out from the structure's physical volume (Tossici-

Bolt *et al* 2006). However, as these last methods prevent an individual quantification of the caudate and putamen regions this can prove unacceptable in some cases.

The AQM post-reconstruction PVE compensation

In AQM, we included a post-reconstruction PVE compensation based on the methodology described in Fleming *et al* 2004. This compensation requires the measurement of the total activity in the striatum and the calculation of the exact volume of each striatal region. The total activity in the striatum is calculated using ROIs which have been automatically expanded with respect to the original striatal regions. These expanded ROIs are large enough to ensure the inclusion of all the activity that has spread outside the physical volume of the structures because of PVE. The advantage of using an automatic expansion is a reduced operator-introduced variability in their positioning.

In this work, the original striatal ROI and the ROI located at the occipital region were defined by using the CT image of the phantom. To perform the quantification of the studies, all the reconstructed images were re-sampled to the high-resolution space where the ROIs had been defined. The exact volumes of the ROIs were calculated using the 3D ROI map. Compensation for PVE was carried out by expanding the original striatal ROI and calculating the mean activity concentration inside the expanded ROI. The total activity inside the original striatal ROI, A_S, was calculated by removing the non-specific uptake from the total activity in the expanded ROI:

$$A_S = \overline{A}_{S'} \cdot V_{S'} - \overline{A}_O \cdot (V_{S'} - V_S) \qquad (5.3)$$

Where $\overline{A}_{S'}$ and $\overline{A}_O$ are, respectively, the mean activity concentrations inside the expanded striatal ROI and the occipital region; V_S and $V_{S'}$ are the volumes of the original and the expanded striatal ROI respectively. Note that this methodology assumes that the activity concentration of the occipital region is a good estimate of the non-specific uptake in the striatal ROI.

If $\overline{A}_S$ is the mean activity concentration in the striatal region, SUR can be written as:

$$SUR = \frac{\overline{A}_S - \overline{A}_O}{\overline{A}_O} \qquad (5.4)$$

By substituting equation (5.3) in the SUR definition, the SUR value after PVE correction can be calculated as:

$$SUR = \frac{\left(\overline{A}_{S'} - \overline{A}_o\right) \cdot V_{S'}}{\overline{A}_o \cdot V_S} \qquad (5.5)$$

The expansion of the striatal ROI was established by calculating the resolution of the reconstruction method. This value was obtained by using SimSET to project a linear source in air with only low-energy photons emission and reconstructing the projections using a transition matrix which included the modelling of the PSF. Simulation and reconstruction processes were performed using the same parameters as those selected for the studies. Then, the reconstructed image was re-sampled to the high-resolution space and fitted to a Gaussian function to calculate the value of the standard deviation σ. The value of the standard deviation in the high-resolution image depends on the collimator and stands for the resolution of the reconstruction.

In this work, the striatal ROI was enlarged by 1σ. For the E.CAM parallel system, σ had a value of 1.90 mm and for the HELIX fan-beam system, σ had a value of 1.75 mm. The original and expanded striatum volume for both imaging systems is shown in table 5.3.

Table 5.3 Enlargement applied to the original volume of the striatal ROI for each SPECT system.

Imaging system	σ (mm)	Vs (ml)	Vs' (ml)	ΔV (ml)
E.CAM system	1.90	21.5	43.2	21.7
HELIX system	1.75	21.5	38.8	17.3

Figure 5.4 shows one central section of the numerical phantom where the ROIs corresponding to the original striatum, the reference occipital region and the expanded striatum have been drawn.

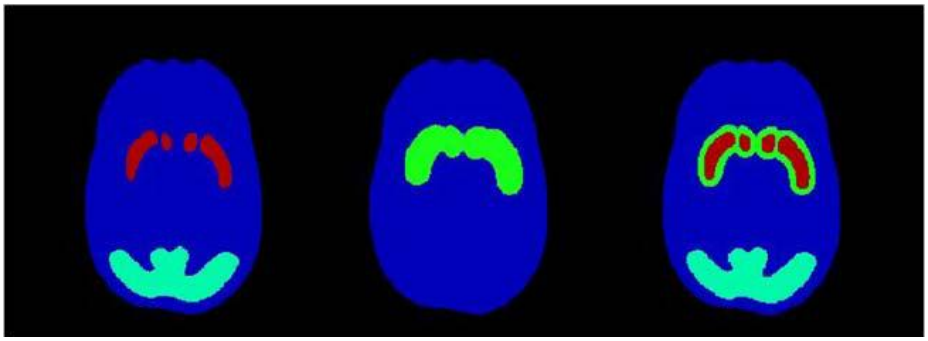

a **b** **c**

Figure 5.4 A central slice of the phantom showing: **a** the considered ROIs for the striatal nuclei (red) and the occipital region (light blue), **b** the expanded striatal ROI (green) and **c** the overlay of **a** and **b**.

5.2.5 Absolute quantification

AQM was designed to provide an absolute volumetric activity at each voxel of the image. However, the values at each voxel of the reconstructed image (λ_i) obtained from equation (5.1) cannot be considered as real activity values. It is therefore necessary to find a factor that transforms these calculated values into real activity, *i.e.* a factor that matches the counts of the simulated and the original projections.

To calculate this factor, the reconstructed image at the first iteration, which had been corrected for attenuation, PSF and scatter, was selected as the input activity distribution of the SimSET simulator. The number of detected counts obtained in this simulation was compared with the total counts of the original projections. The factor that matches the counts of the simulated and the original projections was finally applied to the reconstructed image.

5.3 Results and discussion

5.3.1 Contribution of the high-energy photons to the projections

The contribution of the primary, low-energy scattered photons and high-energy scattered photons to the total projections is shown in figure 5.5 for the two imaging systems studied and for a simulation corresponding to a SUR value of 6.

The numerical values shown in this figure highlight the undeniable significance of high-energy emission when pharmaceuticals labelled with ^{123}I are used in brain SPECT imaging. Comparison of the projections obtained from the two cameras shows that the high-energy contribution is strongly dependent on the imaging system employed. When a LEHR parallel collimator is used with the parameters shown in table 5.1, more than 50% of the total photons detected correspond to scattered photons, with high-energy photons accounting for 40%. These results are in agreement with previous reported results for the same imaging system (Du *et al* 2006). By contrast, for the LEHR fan-beam collimator studied, scattered photons contribution is lower (43%), with a high-energy contamination contribution of about 27%.

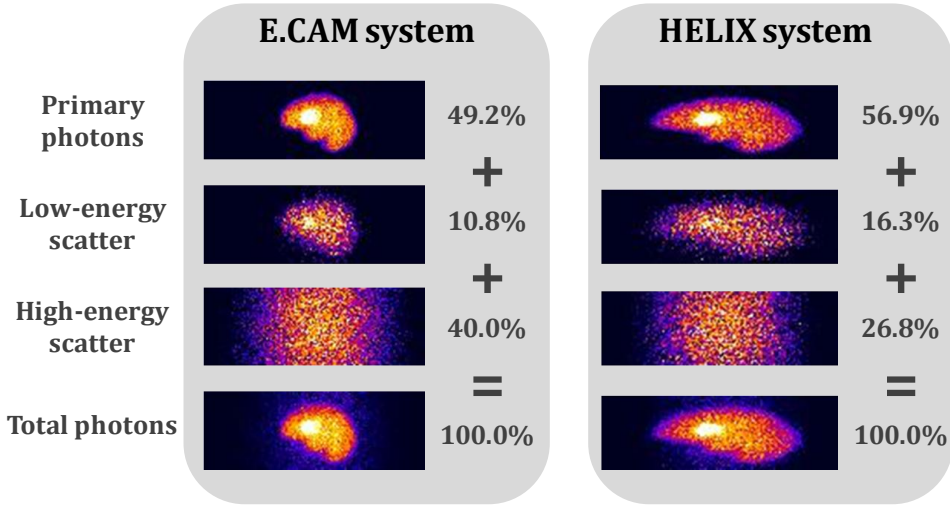

Figure 5.5 A simulated projection of the striatal phantom with SUR of 6 for the E.CAM system (left) and the HELIX system (right). From top to bottom: primary, low-energy scattered photons, high-energy scattered photons and total photons detected. The numerical values of each contribution are also shown. Each image has been normalised to its maximum to improve its contrast.

5.3.2 Effect of the corrections in the quantification

To assess the effect of corrections for the degrading phenomena in the quantification, the following cases were studied:

OSEM: reconstruction without corrections
OSEM-A: reconstruction with attenuation correction
OSEM-AP: 3D-reconstruction with attenuation and PSF corrections
OSEM-APS: 3D-reconstruction with attenuation, PSF and scatter corrections
OSEM-APSV: OSEM-APS plus PVE compensation

The calculated SUR values for the 30 simulated studies reconstructed applying the different corrections are plotted in figure 5.6 against the nominal SURs for both imaging systems.

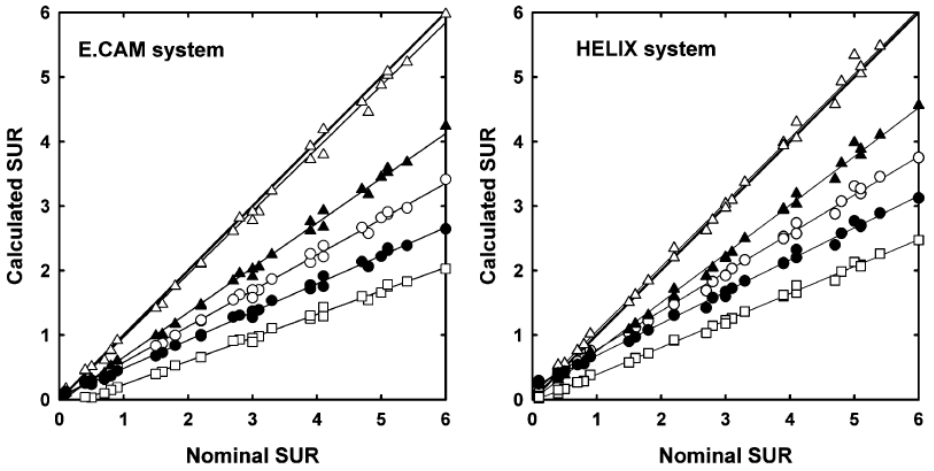

Figure 5.6 Calculated SURs obtained with different corrections for the E.CAM system (left) and the HELIX system (right): OSEM (hollow squares), OSEM-A (filled circles), OSEM-AP (hollow circles), OSEM-APS (filled triangles) and OSEM-APSV (hollow triangles). The dark solid line corresponds to the identity line. The light solid lines correspond to the linear fits for each correction.

A linear relationship was found between calculated and true values in both imaging systems and for all the corrections applied. This relationship may be written as:

$$SUR_{calculated} = \alpha \cdot SUR_{theoretical} + \beta \qquad (5.6)$$

Where α is the slope of the regression line and β stands for the intercept at the origin.

The mean value and standard deviations for α and β, as well as the correlation coefficients of the linear fits are shown in table 5.4 for each imaging system and for all the corrections implemented.

Table 5.4 Mean and standard deviations for α and β and correlation coefficients of the linear fits.

Imaging system	Correction level	α	β	R^2
E.CAM system	OSEM	0.36±0.00	−0.13±0.01	0.997
	OSEM-A	0.44±0.00	0.05±0.02	0.997
	OSEM-AP	0.55±0.01	0.02±0.02	0.997
	OSEM-APS	0.69±0.01	−0.03±0.02	0.997
	OSEM-APSV	0.97±0.01	−0.00±0.03	0.997
HELIX system	OSEM	0.42±0.00	−0.03±0.01	0.998
	OSEM-A	0.50±0.01	0.19±0.02	0.997
	OSEM-AP	0.60±0.01	0.20±0.02	0.997
	OSEM-APS	0.75±0.01	−0.00±0.03	0.997
	OSEM-APSV	1.00±0.01	0.06±0.03	0.997

These results demonstrate that recovered SUR values have a linear relationship with the true specific ratios for both cameras and for each correction applied. It should be pointed out that the relationship between measured and true SUR values is mainly linear with a nonzero intercept at the origin. For high nominal SURs, the slope of the linear regression determines the SUR recovery factor. Nevertheless, for low nominal SURs, the value of the intercept at the origin becomes a determinant parameter as it induces a bias in the recovery factor.

Our findings corroborate that quantitative results are dependent on the imaging system used in the acquisition when the reconstruction method does not include all the corrections for all the degrading phenomena (Koch *et al* 2005, 2006).

For all the cases with the exception of OSEM-APSV, the HELIX camera shows a value of α that is, on average, 6% higher than that of the E.CAM camera. In any case, although both imaging systems achieve different recovery factors with the same corrections, there is a continuous improvement as the corrections are progressively included. For both cameras, the successive corrections raise the value of α from 36 to 97% for the E.CAM system (total increase of 61%) and from 42 to 100% (total increase of 58%) for the HELIX system.

PVE compensation plays a major role in the recovery of the true specific ratios as it may induce an improvement of approximately 25–30% in α values depending on the imaging system used (see table 5.5). The scatter correction also plays an important part as it increases α values by 15%. PSF and attenuation corrections are the least significant corrections with improvements of around 10 and 8%, respectively.

Table 5.5 Improvement achieved in α with each individual correction for each SPECT system.

	E.CAM system	HELIX system
Correction	$\Delta\alpha$ (%)	$\Delta\alpha$ (%)
Attenuation	8%	8%
PSF	11%	10%
Scatter	14%	15%
PVE	28%	25%

On the other hand, the two systems differed in the behaviour of the β values depending on the correction applied. One important fact is that scatter correction causes β to fall close to 0. The addition of the PVE compensation induces a slight increase in β, which has no relevance in the recovery factor of both cameras. Furthermore, PVE compensation minimizes the differences in α, so that both imaging systems attain a recovery factor of around 100%. Thus, our study suggests that recoveries close to 100% may be obtained by expanding the original striatal ROI in 1σ of the spatial resolution of the reconstruction.

5.3.3 Visual effect of the scatter correction

Figure 5.7 shows the reconstructed image of a central slice at the first iteration of the reconstruction algorithm for two cases: OSEM-AP and OSEM-APS.

Improvement is clearly visible when the scatter correction is included. Note that scattered photons detected degrade the image quality as they reduce the signal-to-noise ratio and the resolution in the projections. The first iteration is the most suitable for visual assessment, although the most accurate quantification results are achieved at a higher number of iterations.

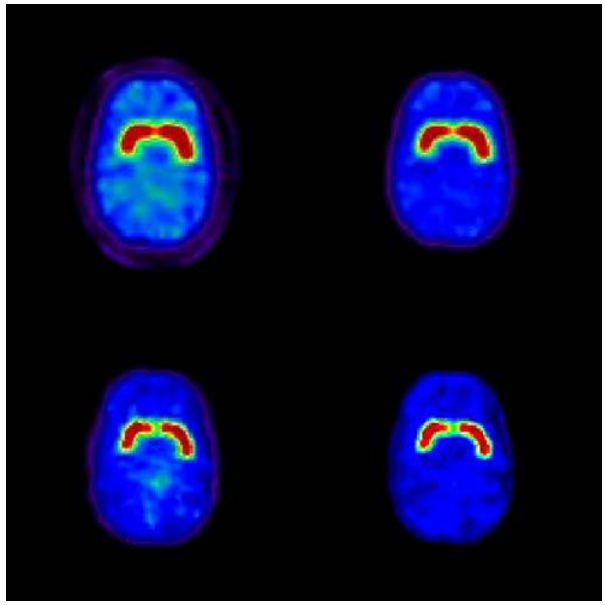

Figure 5.7 Reconstructed central slice of the striatal brain phantom for the E.CAM system (top) and the HELIX system (bottom). For each camera, the images correspond to a nominal SUR of 4.7 and to a reconstruction using OSEM-AP (left) and OSEM-APS (right).

5.3.4 Absolute quantification results

Figure 5.8 shows the bias between calculated and nominal mean activity concentration values as a function of nominal SUR. The bias from the true values was calculated as:

$$\overline{A}_{bias}\,(\%) = \frac{\overline{A}_{calculated} - \overline{A}_{nominal}}{\overline{A}_{nominal}} \times 100 \qquad (5.7)$$

Since the quantification of the radiotracer uptake is less sensitive to PVE in the occipital region than in the striatum because of its size (Du *et al* 2005), PVE compensation is omitted for the occipital region and only the bias in the striatum after PVE compensation is reported.

For the HELIX system and for low values of SUR (approximately between 0.5 and 1), there is a slight positive bias in the striatum when PVE is compensated and a slight negative bias in the occipital region. This causes an overestimation of the calculated SUR in patients with severe reduction in the DAT density.

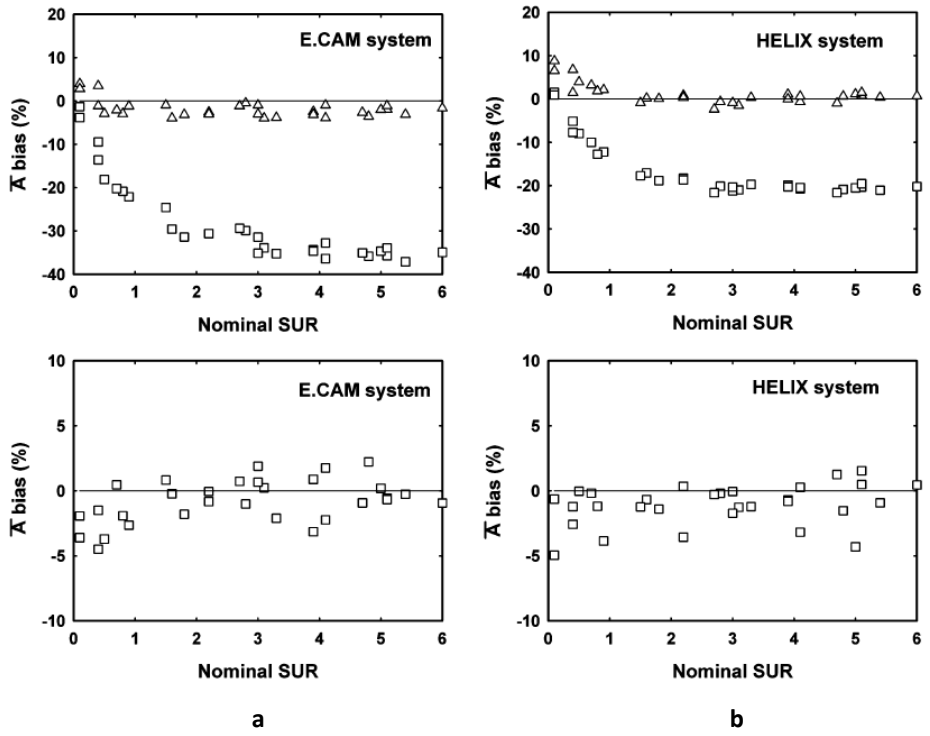

Figure 5.8 The activity concentration bias (%) between calculated and nominal mean activity concentration values vs nominal SURs for (top) the striatum when OSEM-APS (hollow squares) and OSEM-APSV (hollow triangles) are used, and (bottom) the occipital region when OSEM-APS is used (hollow squares). Biases are shown for: **a** the E.CAM system and **b** HELIX system. Horizontal lines represent a percent bias equal to 0.

When reconstruction includes attenuation, PSF and scatter corrections, the calculated mean activity concentration in the striatum is underestimated by about 35% for the E.CAM system and about 20% for the HELIX system, whereas the maximum percent bias in the occipital region is about 5% for both cameras. PVE compensation proves to be effective in minimising the bias in the calculated mean activity concentration in the striatum, reducing errors to about 5% for both systems. These results indicate that PVE compensation in the striatum is necessary for absolute quantification. PVE compensation in the occipital region is not necessary as this area is large enough to influence the measurement of its mean activity concentration.

5.4 Conclusions

Nominal SUR values can be obtained in SPECT neuroimaging provided accurate compensations for all the image-degrading effects are included in the quantification process.

In this chapter we have described, implemented and evaluated AQM, a complete methodology to compensate for all the image-degrading phenomena, including PVE. The effect of the different compensations on SUR quantification has also been assessed. Our findings show that PVE compensation stands out as the most relevant correction, followed by scatter correction.

Chapter 6

6 Semi-quantification of dopaminergic neurotransmission SPECT studies with ^{123}I for clinical routine

6.1 Introduction

Chapter 5 presented a complete methodology that allows recovery of the true activity concentration in the striatum after correction for all the degrading effects involved in dopaminergic neurotransmission SPECT imaging with ^{123}I-labelled radioligands. Although absolute quantification can be achieved using this methodology, some of its computational and technical requirements still prevent a direct implementation in clinical practice. The length of time required for reconstruction is a handicap as well as the need for MR images, which are not usually included in the diagnostic protocols for PD and schizophrenia, for ROI definition. In addition, scatter correction is based on MC simulation which requires the use of a dedicated code that incorporates the characterisation of the imaging system employed.

In clinical routine, simple, reliable and rapid methods are needed to extract high-quality quantitative information from the studies. Quantitative information improves sensitivity, aids diagnosis and patient follow-up and assesses the response to therapy. In neurological practice, a semi-quantitative analysis is highly recommended to objectively assess striatal DAT binding (Darcourt *et al* 2010) or striatal D2 receptor binding (van Laere *et al* 2010) and several semi-quantification methodologies have been proposed (Badiavas *et al* 2011). Some of these methods use anthropomorphic phantoms to demonstrate their reliability by means of a comparison with the true values (Calvini *et al* 2007, Dickson *et al* 2012).

In these studies, a linear relationship between measured and true striatal to background ratios was observed. This linear relationship was found to be dependent on the imaging system used during acquisition and on the reconstruction method applied (Koch *et al* 2006, Crespo *et al* 2008, Tossici-Bolt *et al* 2008, 2011). Some research groups have used the linear relationship calculated for a phantom to standardise all the studies carried out using the same camera system and protocols as the phantom (Varrone *et al* 2013). However, the applicability of a single set of parameters of the linear model to any subject, regardless of morphological differences and striatal specific uptake, has not been validated. Under real conditions, both anatomical variability between subjects and the PVE may affect the linear behaviour between observed and true values (Dewaraja *et al* 2001).

The aim of this chapter is to evaluate whether a linear relationship could also be established for a group of subjects with normal and pathological striatal uptake values. In this evaluation MC simulation was used, thus facilitating the analysis of a large variety of anatomical and tracer uptake cases and the evaluation of the reliability of the methodology applied.

The MC simulation of a test group of studies corresponding to 23 different subjects with non-negligible anatomical differences was performed. Quantification was carried out using the actual striatal ROIs derived from MRI and striatal ROIs derived from the AAL map (Tzourio-Mazoyer *et al* 2002). Caudate and putamen were quantified separately. The study focused on the influence of anatomical variability and PVE on results, as they are the factors most likely to compromise the linear relationship.

6.2 Materials and methods

6.2.1 Numerical brain maps for the simulated test studies

The numerical dataset group was generated using 3D T1-weighted MR images (256x256x116 matrix size; 0.9375x0.9375x1.5 mm^3 voxel size) corresponding to 23 subjects free of cerebral abnormalities. A CT image of an anthropomorphic striatal brain phantom (Radiology Support Devices, RSD. Inc, Long Beach, CA), 256x256x196 matrix size, with a voxel size of 0.89x0x89x0.89 mm^3, was co-registered to each MR image in order to get a bone structure for each subject. The scans were segmented to generate subject-specific activity and attenuation maps that were then used to simulate the projections. The main steps in this procedure are outlined below.

Activity maps

To generate the activity maps, MR images were segmented into grey matter, white matter and cerebrospinal fluid using Statistical Parametric Mapping (SPM2, Wellcome Department of Imaging Neuroscience, London, UK). Non-specific uptake was considered to be the same for grey and white matter, whereas the activity in the cerebrospinal fluid was assumed to be zero. The striatum was segmented from the MR images. The FIRST segmentation tool from FSL (FMRIB, University of Oxford, UK) (Patenaude *et al* 2011) was used to select caudate and putamen nuclei of each subject.

A comprehensive range of possible striatal to background uptake ratios was drawn up, modelling normal and pathological distributions of ^{123}I-FP-CIT. To this end, tracer uptake in caudate and putamen was simulated, assuming that the activity concentration in caudate could not be lower than that in putamen. A wide variety of tracer uptakes in caudate and putamen were simulated, including normal and pathological cases. Activity concentration was considered to be uniform within the whole caudate, putamen and background.

Attenuation maps

The set of 23 MR images was spatially normalised to the T1-weighted template from the MNI, which is included in SPM. A CT image was also obtained from an anthropomorphic striatal brain phantom and normalised to the transmission template of SPM. A 12-parameter affine transformation was considered. Finally, the

inverse transformations of the normalised MR images were applied to the normalised CT so as to obtain a CT image fitted to each MR (Aguiar *et al* 2008).

To generate the attenuation maps, the normalised CT image was segmented into brain and bone using a threshold value. Attenuation maps were obtained by setting the corresponding attenuation coefficients for brain tissue and bone depending on the energy of the simulated photons. Figure 6.1 shows an axial view of the original MR image together with activity and attenuation maps of one of the subjects used for the simulation.

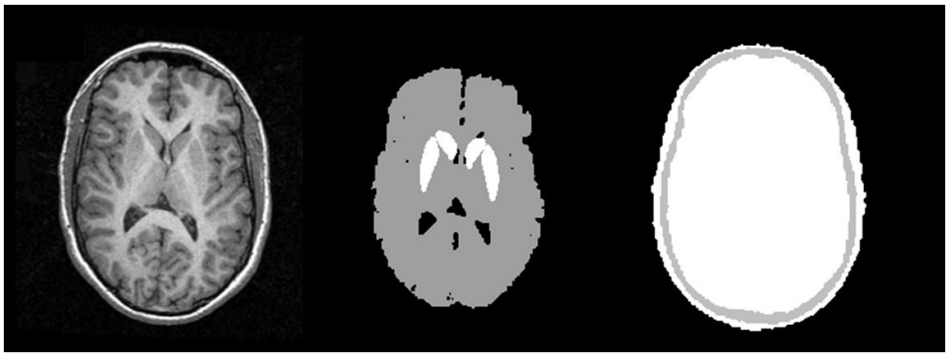

Figure 6.1 Axial views of a randomly selected subject, corresponding to: **a** original MR image, **b** activity distribution map and **c** attenuation map.

6.2.2 Anatomical variability between simulated test studies

The anatomical variability between simulated test studies was quantitatively evaluated by determining the volume of the striatal regions of each subject.

The sample proved to contain non-negligible anatomical variations. The volume of the whole striatum ranged from 19 ml to 27 ml with a coefficient of variation of 9%. Caudate showed the greatest differences between hemispheres, with a 5% difference between the mean volumes of the right and left caudate. Maximum differences in volume between the test subjects ranged from 37% for the right putamen to 49% for the right caudate. The descriptive statistical parameters of these volumes are shown in figure 6.2.

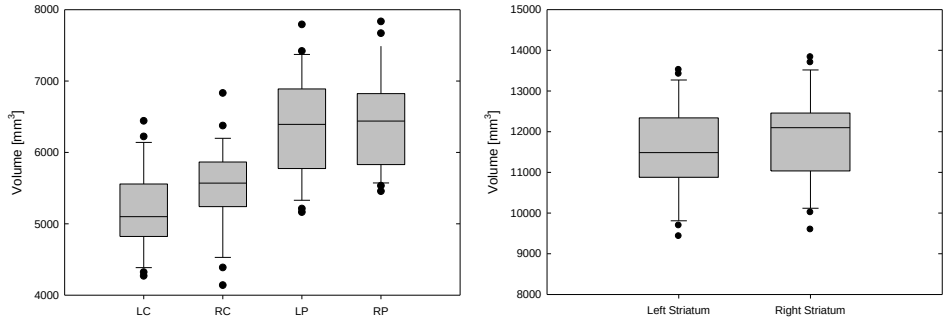

Figure 6.2 Box plots of the volumes of the different striatum regions. LC: left caudate; RC: right caudate; LP: left putamen; RP: right putamen.

6.2.3 SPECT imaging system and SimSET simulation

SPECT projections were simulated for a Siemens E.CAM gamma camera equipped with a LEHR parallel-hole collimator (hexagonal holes 24.05 mm in length with a radius of 0.641 mm and a septal thickness of 0.16 mm).

Subject-specific projections were obtained using the new version of SimSET, which adapts the code to ^{123}I-labelled radioligands simulation (see chapter 4). Six sinograms with a high signal-to-noise ratio were generated for each of the 23 subjects, resulting in a simulated database of 138 studies. SUR values between 0.5 and 10 for caudate and putamen were selected in such a way that a well-distributed sample was obtained. Simulated studies included normal uptake and pathological cases. The pathological cases covered a wide range of possible clinical situations: uniform global striatal uptake reduction and a variety of uptake asymmetries between caudate and putamen, both unilateral and bilateral. Figure 6.3 shows the theoretical SUR values for caudate and putamen for each study.

Studies with a high signal-to-noise ratio were chosen since the aim was to evaluate the PVE without noise interference and earlier studies have shown that differences in the mean SUR values of simulations due to noise are negligible (Cot *et al* 2005). Acquisition parameters were selected according to routine conditions. A total of 128 projections were acquired over 360° using a bin size of 3.9 mm and a 15% energy window. The radius of rotation was considered to be 14.5 cm.

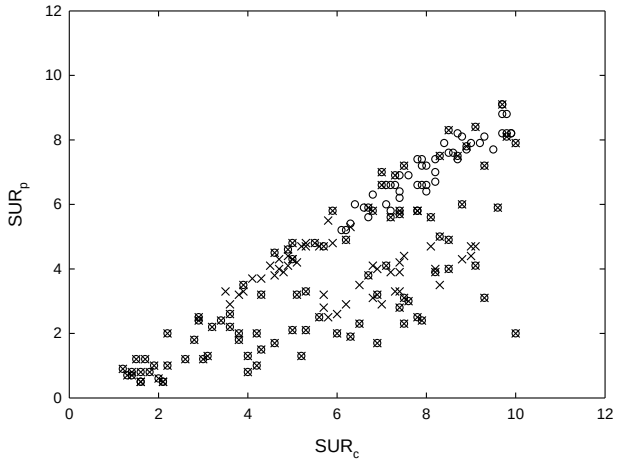

Figure 6.3 Theoretical SUR values for caudate and putamen for each of the 138 simulated studies (hollow circle for left hemisphere and cross for right hemisphere). Asymmetries between left and right hemispheres are seen as non-coincidences between circles and crosses.

6.2.4 Reconstruction of the simulated projections

Reconstruction was performed using FBP and the OSEM algorithm. In FBP reconstruction, MC projections were filtered using a two-dimensional Butterworth filter (order 5; cut-off frequency 0.5 cm^{-1}) and then reconstructed by FBP with a ramp filter. Datasets were corrected for attenuation according to Chang's method and using the attenuation maps for shape contouring. An effective linear attenuation coefficient of 0.10 cm^{-1} was used to generate the uniform attenuation maps, as recommended in the EANM guidelines (Darcourt *et al* 2010) for ^{123}I in the absence of scatter correction (Zaidi and Montandon 2002).

MC projections were also reconstructed using the OSEM algorithm with 8 subsets and 3 iterations (Koch *et al* 2005) and included both attenuation and ideal scatter correction. Attenuation correction was implemented using the corresponding attenuation maps with attenuation coefficients of 0.149 cm^{-1} for brain and 0.307 cm^{-1} for bone. The ideal scatter correction was achieved by considering only the primary photons in the projections. Reconstructed images consisted of 128x128x45 voxels with a voxel size of 3.90x3.90x3.90 mm^3.

6.2.5 Quantification methodology

Reconstructed images were quantified using the actual striatal ROIs and ROIs derived from the AAL map defined in the MNI standard space.

In the first approach, quantification was performed directly over the reconstructed SPECT studies. To this end, the striatal cavities segmented from the original MR images were resized to fit with the reconstructed images. The reference ROI was defined on the occipital region of the MR template of SPM. This occipital ROI was placed on each study by applying the inverse transformations of the previously normalised MR images. Finally, the occipital ROIs were resized to fit the reconstructed images. Since simulated projections had a high signal-to-noise ratio and the quantification ROIs corresponded to those used in the simulation, variability was exclusively associated to anatomical differences and PVE.

In the second approach, each reconstructed image was normalised to a template defined in the MNI standard space. This template was obtained from 14 normal control studies simulated using 14 subjects different from those employed to generate the benchmark sample (see figure 6.4).

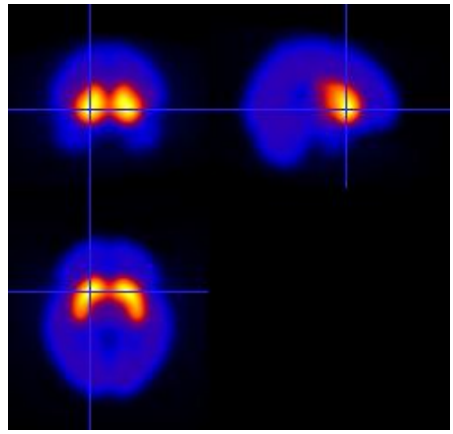

Figure 6.4 Coronal (top left), sagittal (top right) and axial (bottom) views of the SPECT template.

Normalisation was performed in two steps. In the first step, images were normalised to the template using SPM. In the second step, a fine adjustment of the reconstructed striatum of each hemisphere was made by optimizing the local correlation coefficient (LCC) with the corresponding hemisphere of the template (Pavia *et al* 1994). To generate the ROIs, we selected those corresponding voxels

from the striatal AAL ROIs which were common to both hemispheres, thus, generating a symmetric ROI for caudate and putamen. These symmetric AAL ROIs (AAL_{sym}) were finally used to quantify the MNI normalised studies.

Figure 6.5 shows the MRI and AAL_{sym} ROIs on a central slice of a test study reconstructed using OSEM.

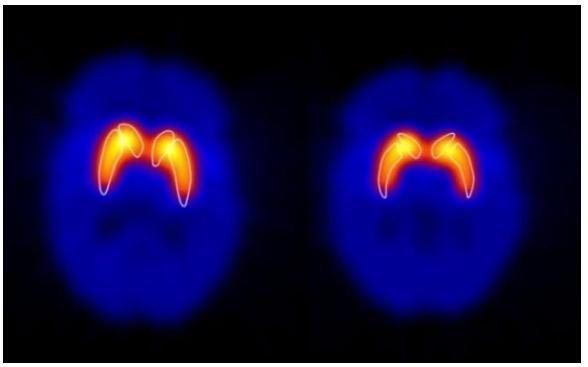

Figure 6.5 A central slice of a reconstructed study using OSEM, showing the striatal MRI ROIs (left) and the AAL_{sym} ROIs (right). Note that the image on the right is in the MNI standard space.

Figure 6.6 shows the reference region on a MR image of one of the subjects.

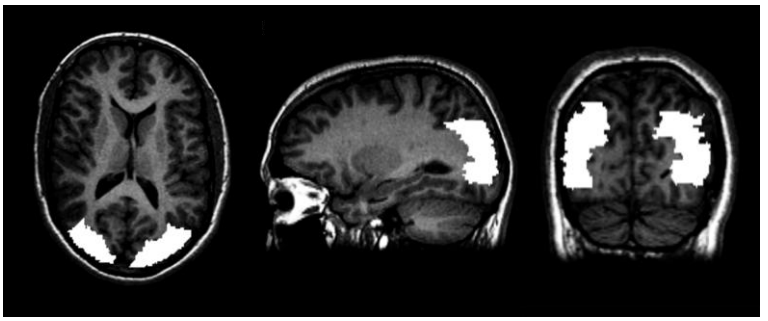

a **b** **c**

Figure 6.6 Axial **a**, sagittal **b** and coronal **c** views of a MR image of a randomly selected subject showing the reference ROI defined on the occipital region.

6.2.6 Standardisation methodology

From studies performed using phantoms, it has been suggested that the calculated striatal SUR (SUR_s^{cal}) for a subject after reconstruction, with or without

corrections for the degrading phenomena, can be written as (Koch *et al* 2006, Crespo *et al* 2008):

$$SUR_s^{cal} = \alpha \cdot SUR_s + \beta \qquad (6.1)$$

Where α is the slope of the regression line, SUR_s is the true value in the striatum and β stands for the intercept. However, if this model is applied to individual caudate or putamen, the influence of adjacent regions is not taken into account.

If the contribution of the counts from the adjacent regions (caudate or putamen) are included in equation (6.1), a new multiple linear model for the individually calculated SURs in caudate and putamen (SUR_c^{cal} and SUR_p^{cal}) can be defined as the following Striatal Uptake Linear System (SULS):

$$\begin{pmatrix} SUR_c^{cal} \\ SUR_p^{cal} \end{pmatrix} = \begin{pmatrix} \alpha_c & k_p^c \\ k_c^p & \alpha_p \end{pmatrix} \cdot \begin{pmatrix} SUR_c \\ SUR_p \end{pmatrix} + \begin{pmatrix} B_c \\ B_p \end{pmatrix} \qquad (6.2)$$

Where α coefficients represent the fraction of true SUR (SUR_c or SUR_p) recovered in the corresponding structure, k coefficients express the fraction of true SUR from adjacent regions that contributes to the calculated SUR and B terms are constants which depend on the reconstruction method. This multiple linear model is inspired by the work by Rousset *et al* (1998) for PVE correction of mean activity values between adjacent ROIs.

In the current study, we assessed how well the SULS model (valid for an individual) describes the relationship between calculated and true SUR values for each individual when we use a single set of parameters obtained as the average values of a group of subjects. The simple linear model was also applied to check its suitability. Thus, standardised values were obtained from the simple linear model by applying the inverse of equation (6.1) and from the multiple linear model by applying the inverse of the system shown in (6.2). Differences between standardised and true values were quantified using the chi-square value (χ^2).

The χ^2 is defined as:

$$\chi^2 = \sum_{i=1}^{N} \frac{\left(\theta_i - \hat{\theta}_i\right)^2}{\hat{\theta}_i} \qquad (6.3)$$

Where θ_i is the standardised value of study i, $\hat{\theta}_i$ is the true SUR and N is the number of studies.

6.3 Results and discussion

6.3.1 Contribution of PVE to the measured SUR values

Contribution of PVE to the measured SUR values was studied by performing two different sets of simulations. One set considered that only caudate had specific uptake while the other one considered that only putamen had it. Ideally, reconstructed images should only show high activity concentration in caudate and putamen, respectively. However, specific uptake was also found in adjacent regions because of PVE and non-ideal scatter correction.

Figure 6.7 shows a central slice of the FBP-reconstructed image of a study simulated under the two situations described. Images **a** and **b** in figure 6.7 correspond to simulations with specific uptake only in caudate or in putamen, respectively. Image **c** shows the overlay of the previous ones.

In agreement with the previous description of the multiple linear model, this figure shows that detected photons that should increase the counts in each of these structures also contribute to the counts in adjacent regions, thereby masking the real activity in all these areas.

The counts that spill into caudate from putamen cause SUR_c^{cal} to inflate by a value which is proportional to SUR_p. The same phenomenon occurs in putamen, where counts that spill in from caudate inflate SUR_p^{cal} in the regions closest to caudate. The area most affected by the spill-out of counts from caudate is the anterior putamen. In the central putamen this influence is hardly noticeable and in the

posterior area it can be ignored. The increase due to these counts is proportional to SUR_c .

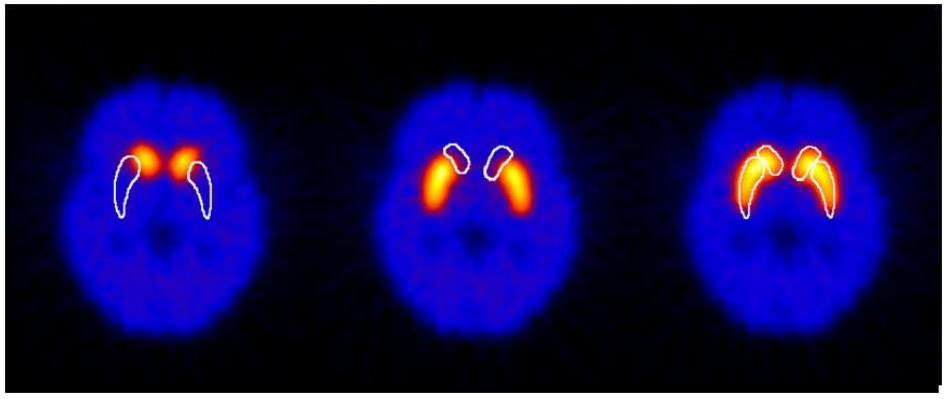

a **b** **c**

Figure 6.7 A central slice of a study using FBP, showing the spill-out of counts from caudate to putamen **a** and from putamen to caudate **b**. In **c**, the overlay of **a** and **b** is shown.

For a randomly selected study quantified using FBP reconstruction and MRI ROIs, the PVE between adjacent regions makes SUR_c^{cal} increase linearly with SUR_p , as $SUR_c^{cal} = 0.035 \cdot SUR_p + 2.13$ when SUR_c has a nominal value of 6. The same phenomenon applies vice versa with $SUR_p^{cal} = 0.036 \cdot SUR_c + 2.14$ when SUR_p has a nominal value of 6. These results show that the influence of PVE causes the calculated SUR to rise to 9% when the adjacent region varies from a nominal value of 0 to 6.

Thus, the qualitative and quantitative results derived from this study suggest that PVE between the striatal regions should be taken into account when defining the relationship between calculated and true SUR values.

6.3.2 Measured individual SUR values for caudate and putamen

Figure 6.8 shows SUR_c^{cal} and SUR_p^{cal} from each hemisphere against their corresponding true values for the 138 simulated test studies. Results are shown for the two reconstruction methods (FBP and OSEM) and the two sets of ROIs applied

(MRI ROIs and AAL_{sym} ROIs). Note that 138 studies generate a database of 276 values for each striatal region (138 studies x 2 hemispheres).

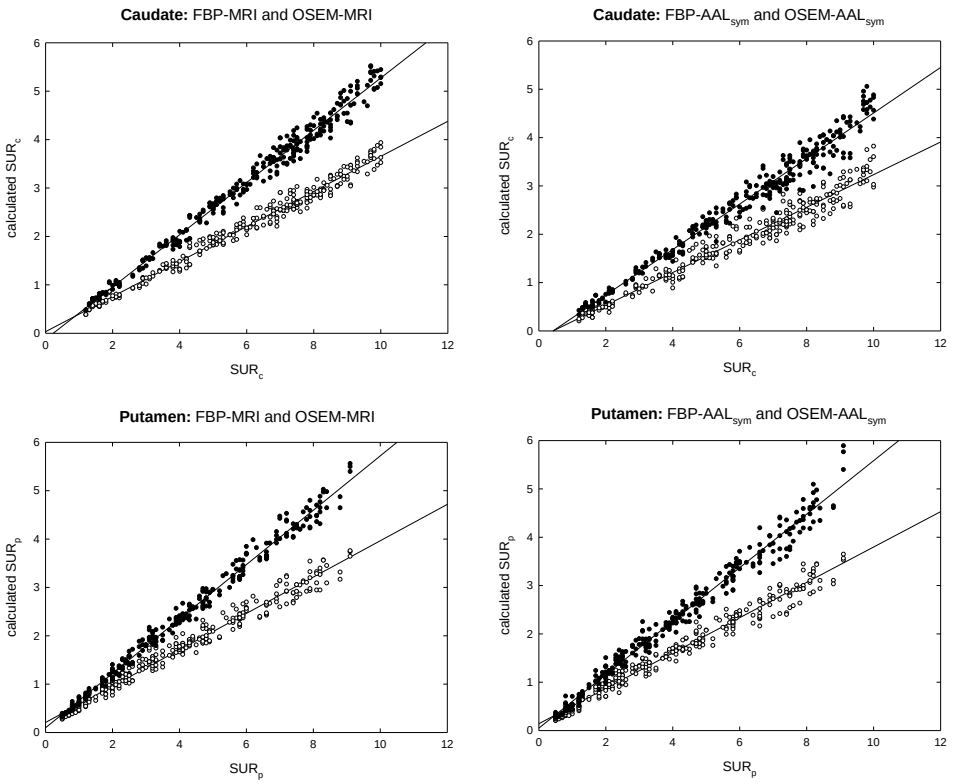

Figure 6.8 Calculated SUR values in caudate and in putamen against their corresponding true values for the two reconstruction methods and the two different ROIs (MRI and AAL_{sym}). Hollow circles indicate reconstruction using FBP and filled circles indicate reconstruction using OSEM. Regression lines are shown as solid lines.

Tables 6.1 and 6.2 show, respectively, the mean and standard error for the parameters of SULS obtained by multiple linear regression of the 138 simulated studies and the slope and intercept (with their standard errors) if a simple linear relationship is applied. Parameters are shown for each reconstruction and quantification method and for each striatal region.

The high values of R^2 found for all the quantification methods applied indicate that not only is the relationship between the calculated and the true striatal values for each individual one of linearity, but also the global behaviour of the whole group of patients, even for individual striatal regions. This would indicate that, despite anatomical differences between subjects and the specific effect of PVE in each

individual, the global behaviour of striatal uptake may be described using some common parameters.

Table 6.1 Mean and standard errors for the parameters obtained by multiple linear regression (SULS) of the 138 simulated studies.

Striatal region	Quantification method	Multiple linear regression (SULS)			
		α	k	B	R^2
Caudate	FBP-MRI	0.332 ± 0.004	0.040 ± 0.005	0.053 ± 0.018	0.985
	FBP-AAL$_{sym}$	0.291 ± 0.007	0.060 ± 0.007	-0.113 ± 0.026	0.963
	OSEM-MRI	0.514 ± 0.006	0.034 ± 0.006	-0.106 ± 0.025	0.987
	OSEM-AAL$_{sym}$	0.427 ± 0.008	0.057 ± 0.008	-0.171 ± 0.031	0.974
Putamen	FBP-MRI	0.344 ± 0.005	0.039 ± 0.005	0.104 ± 0.021	0.980
	FBP-AAL$_{sym}$	0.324 ± 0.005	0.052 ± 0.005	0.003 ± 0.020	0.980
	OSEM-MRI	0.545 ± 0.006	0.021 ± 0.005	0.040 ± 0.022	0.990
	OSEM-AAL$_{sym}$	0.514 ± 0.007	0.049 ± 0.007	-0.082 ± 0.028	0.984

Table 6.2 Mean and standard errors for the parameters obtained by simple linear regression of the 138 simulated studies.

Striatal region	Quantification method	Simple linear regression		
		α	β	R^2
Caudate	FBP-MRI	0.362 ± 0.003	0.033 ± 0.020	0.980
	FBP-AAL$_{sym}$	0.338 ± 0.005	-0.143 ± 0.030	0.952
	OSEM-MRI	0.540 ± 0.004	-0.123 ± 0.026	0.986
	OSEM-AAL$_{sym}$	0.471 ± 0.005	-0.200 ± 0.033	0.969
Putamen	FBP-MRI	0.376 ± 0.004	0.208 ± 0.017	0.976
	FBP-AAL$_{sym}$	0.366 ± 0.004	0.142 ± 0.018	0.973
	OSEM-MRI	0.563 ± 0.004	0.097 ± 0.017	0.989
	OSEM-AAL$_{sym}$	0.553 ± 0.005	0.050 ± 0.022	0.981

The multiple linear model takes into account the PVE phenomena that occurs between adjacent striatal regions. The single set of parameters obtained for the SULS model by multiple linear regression adequately describes the relationship between calculated and true SUR values providing accurate results and high correlation coefficients for both caudate (R^2 in the range 0.963-0.987) and putamen (R^2 in the range 0.980-0.990). On the other hand, results in table 6.2 show that a simple linear relationship can also be established when the PVE is not explicitly included in the model. In this case, however, R^2 values are slightly lower than those of the multiple linear model (R^2 for caudate in the range 0.952-0.986 and R^2 for putamen in the range 0.973-0.989).

It should be noted that these results were obtained assuming a uniform activity distribution within the whole caudate and putamen. In the case of non-uniform activity concentration along these regions, the quantitative results might be slightly modified because of changes in PVE due to intra-regional tracer distribution.

6.3.3 Estimation of the true individual SUR values

Standardised values for individual caudate and putamen were obtained using the multiple linear model as well as the approximation given by the simple linear model. An estimation of the true SUR for caudate and putamen for each individual was calculated by applying the inverse of the regression systems shown in equations (6.1) and (6.2) using the parameters of tables 6.2 and 6.1 for the simple and multiple linear model.

Figure 6.9 shows the estimated SURs against the true values for the 138 simulated tests. Estimated SURs were obtained using the parameters of SULS and those of the linear regression. The linear fits of the estimated SURs are shown in table 6.3.

As table 6.3 shows, more accurate results and lower variability were found when the SULS model was applied, especially when FBP was used. For FBP-MRI, χ^2 values diminished by 18% for caudate and by 30% for putamen when multiple instead of simple linear regression was used. For FBP-AAL_{sym}, χ^2 values diminished by 5% for caudate and by 48% for putamen.

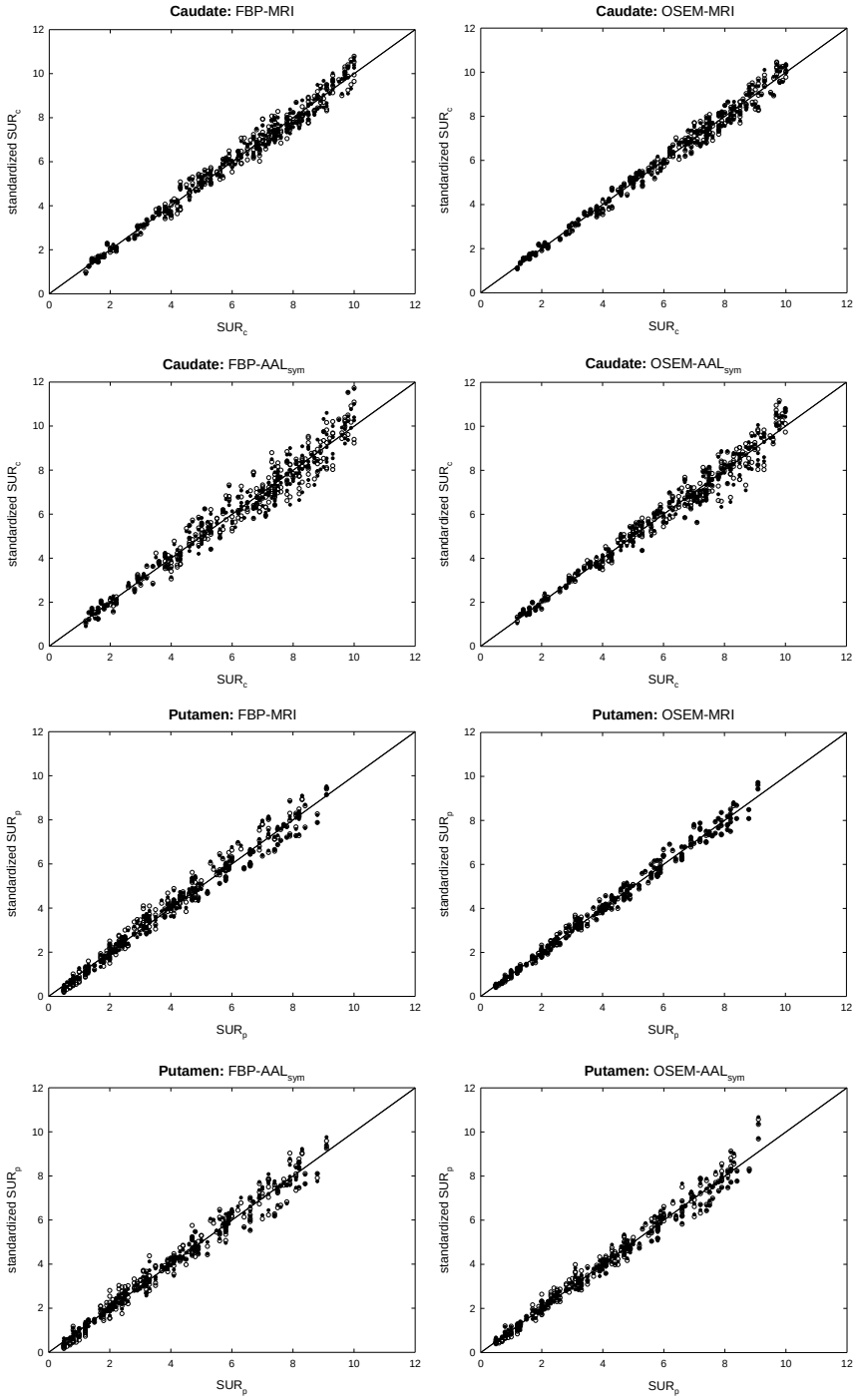

Figure 6.9 Standardised SUR_c and SUR_p against the true values obtained by using the SULS model (filled circles) and the simple linear regression model (hollow circles). Regression lines are shown as solid lines.

Table 6.3 Correlation coefficients of the linear fits of the standardised SUR_c and SUR_p calculated applying the SULS model and the simple regression model.

The χ^2 between standardised and true values is shown for each model.

Striatal region	Quantification method	(SULS) Multiple linear regression		Simple linear regression	
		R^2	χ^2	R^2	χ^2
Caudate	FBP-MRI	0.984	4.28	0.980	5.24
	FBP-AAL$_{sym}$	0.955	11.79	0.952	12.44
	OSEM-MRI	0.986	3.48	0.986	3.62
	OSEM-AAL$_{sym}$	0.970	7.13	0.969	7.42
Putamen	FBP-MRI	0.979	7.36	0.976	10.50
	FBP-AAL$_{sym}$	0.979	6.55	0.973	12.57
	OSEM-MRI	0.990	3.27	0.989	3.62
	OSEM-AAL$_{sym}$	0.983	5.18	0.981	6.96

Differences were found to be less important when OSEM was applied (4-10%) with the exemption of OSEM-AAL$_{sym}$ for putamen, where multiple linear regression diminished χ^2 value by 26%.

The goodness of the fit using the SULS model improves that of the simple linear model, especially for those studies where $k_p^c \cdot SUR_p$ and $k_c^p \cdot SUR_c$ terms in equation (6.3) have a relevant contribution to the calculated SUR_c^{cal} and SUR_p^{cal}, respectively. Thus, for caudate the SULS model will be particularly appropriate for studies with high SUR_p values such as those corresponding to healthy controls (maximum improvement was found for FBP-MRI with a reduction of almost 50% in χ^2 value). For putamen, the SULS model will provide more accurate values than the simple linear model in those studies where there is a large asymmetry between caudate and putamen (maximum improvement was found for FBP-AAL$_{sym}$ with a reduction of 85% in χ^2 value).

It should be pointed out that the set of parameters applied to each model was obtained by linear regression of the dataset and, as a consequence, was fully representative of the average performance of the test studies simulated in this work. In a clinical context, anthropomorphic striatal phantoms could still be used to determine those parameters, provided they can be considered representative of the average anatomy of the population. Parameters for both the linear and the SULS models should be obtained from the phantom using the same protocol as that applied to the patient studies, *i.e*. imaging system, acquisition conditions, reconstruction algorithm and quantification method.

In summary, reconstruction and quantification methods were found to have a high impact on the linearity of the relationship between calculated and true values, and on the accuracy of the standardised results. The use of iterative reconstruction in conjunction with precise attenuation and scatter corrections improved linearity and accuracy with respect to FBP using an effective linear coefficient. The application of generic ROIs instead of subject specific ROIs, yielded inaccuracies due to the normalisation process and morphological differences between the generic ROI and the actual ROI of each subject. In general, linearity and accuracy were found to be lower when using generic ROIs than when the gold standard MRI ROIs were used, especially in caudate. These results indicate that wherever available, the use of subject specific ROIs derived from a co-registered MRI scan or, in the future, from hybrid SPECT/MRI systems should be the method of choice.

6.4 Conclusions

A number of works using anthropomorphic phantoms have shown a linear relationship between calculated and true SUR values for a subject. As a consequence, several standardisation methods use the linear relationship calculated for a phantom to standardise the SUR values. However, these methods take it for granted that the parameters derived from the phantom characterization are valid for any subject, regardless of morphological differences and whatever the uptake ratio between the caudate and putamen nuclei of the subject.

In this chapter we have evaluated the feasibility of this assumption using a dataset of simulated studies which mimicked studies of pathological and healthy subjects. Our findings show that anatomical variability does not compromise the general linear model between calculated and true SUR values for any of the quantification methods applied. A single set of parameters obtained for the SULS model by

multiple linear regression adequately describes the relationship between calculated and true SUR values for both caudate and putamen. This behaviour can also be described by a simple linear model, albeit with slightly lower correlation coefficients. Thus, this work demonstrates that a simple linear relationship with a single set of parameters can be used to standardise the calculated SUR values of those studies carried out using the same imaging equipment and following the same reconstruction and quantification procedures.

Chapter 7

7 Applications

7.1 Introduction

In the previous chapters the difficulties associated with an accurate quantification of dopaminergic neurotransmission SPECT images have been evaluated and two different methodological strategies to achieve reliable quantitative values have been proposed. The first methodology allows recovery of the true activity concentration in the striatum after correcting for all the degrading effects. In this case, computational and technical requirements limit the applicability of this methodology to clinical research trials. The second methodology consists of a semi-quantification method that offers standardised values in the clinical routine. Both quantification methodologies have been evaluated using MC simulation, which allows us to know the ground truth.

The works developed in chapters 5 and 6 have permitted, *inter alia*, a study of the contribution of scattered photons to the projections in different imaging systems, an evaluation of the importance of correcting for degradations in the quantification accuracy, and have demonstrated that standardisation can be achieved using a simple linear regression model. Besides the above methodological works based on MC simulation, these methods have also been applied in research and clinical frameworks with real studies. The aim of these works was to extract reliable quantitative information from the SPECT images to help in the development of antipsychotic drugs and in the diagnosis of neurological and psychiatric diseases associated with dysfunction of the dopaminergic system (see chapter 1).

In this chapter, the contribution to these studies of the methodologies presented in this thesis is briefly discussed. Table 7.1 summarises the main methodological issues of the three studies presented below.

Table 7.1 Main methodological criteria followed in the three works with real studies.

Study	Type of study	Imaging system	Reconstruction method and corrections applied	Quantification method
Bullich *et* al 2010 Neuroimage	Research	PRISM	FBP with attenuation correction (Chang's method) OSEM with attenuation and PSF corrections (AQM) OSEM with attenuation, PSF and scatter corrections (AQM)	Absolute quantification with MRI ROIs defined in the space of each subject
Mané *et al* 2011 Psychiatry Res	Clinical	HELIX	FBP with PSF correction (Metz filter)	Relative quantification with geometrical ROIs defined in the standard space of a SPECT template
Iranzo *et al* 2010 Lancet Neurol	Clinical	E.CAM	FBP with attenuation correction (Chang's method)	Relative quantification with geometrical ROIs defined in the standard space of a SPECT template

7.2 Impact of scatter correction on D_2 receptor occupancy measurements using ^{123}I-IBZM SPECT: Comparison to ^{11}C-Raclopride PET

7.2.1 Aim of the study

In 2009, Catafau *et al* raised the question of the differences found in striatal dopamine D_2 receptor occupancy (RO) values when measured using SPECT or PET imaging. Reported D_2 RO values induced by antipsychotic drugs reveal that

measured values with ^{123}I-IBZM SPECT tend to be lower than those measured with ^{11}C-Raclopride PET for any given dose medication.

In 2010, Bullich *et al* gave response to this question. The authors suspected that image degrading factors that are not routinely corrected in SPECT and, specifically, scatter of low and high-energy photons were responsible for this difference. Thus, we used the AQM method presented in chapter 5 to reconstruct the SPECT images with accurate scatter compensation.

7.2.2 Materials and methods

To clarify this issue, the authors designed a precise research work to measure D_2 RO in the same subjects using both ^{123}I-IBZM SPECT and ^{11}C-Raclopride PET. A total of 26 studies from 9 healthy subjects and 17 patients with schizophrenia recruited in the study above mentioned (see Catafau *et al* 2009) and an experimental striatal phantom were included in this study.

SPECT projections were acquired with a Picker PRISM 3000 S gamma camera equipped with a fan-beam collimator (see chapter 4 for a detailed description of the imaging system). To identify the origin of the quantitative differences between both imaging techniques, we reconstructed the SPECT images using different correction levels: FBP with attenuation correction applying the Chang's algorithm, OSEM with attenuation and PSF corrections and, finally, OSEM with attenuation, PSF and scatter corrections. Reconstructions using OSEM were performed using the AQM method for ^{123}I-labelled radioligands. PET images were reconstructed elsewhere using FBP and corrected for attenuation, scatter, random coincidences and dead time. PET transmission scans were obtained to define the attenuation maps used in the attenuation correction.

In addition, each subject underwent a MRI scan. Individual MR images were used to manually delineate subject specific anatomical ROIs. Quantification was performed using these ROIs once each MRI was coregistered to the corresponding SPECT and PET images.

7.2.3 Discussion

^{123}I-IBZM SPECT images from the 26 subjects and from the experimental phantom were quantified in our laboratory using the AQM method presented in chapter 5 for

the absolute quantification of SPECT studies with ^{123}I-labelled radioligands. We calculated the scatter estimation for each individual subject using the new version of the MC code SimSET adapted to the simulation of ^{123}I SPECT studies. Activity maps were derived from the reconstructed images without scatter compensation and the attenuation maps were obtained from PET transmission scans. The characterisation of the gamma camera was already included in the collimator module of SimSET (see chapter 4 for a detailed description). Note that, in this work, AQM was used to quantify D_2 RO, thus demonstrating its applicability in studies of the postsynaptic functioning.

SPECT D_2 RO values were found to be significantly lower when compared to PET when FBP with attenuation correction, and OSEM with attenuation and PSF corrections were applied, with differences of about 20%. In contrast, when scatter correction was included in the reconstruction algorithm, differences diminished to approximately 6%. Thus, it was concluded that scatter correction plays a major role in explaining the differences between D_2 RO values measured using ^{123}I-IBZM SPECT and ^{11}C-Raclopride PET and should be taken into consideration when interpreting the results.

In this work, the accuracy of the scatter estimation achieved using AQM was essential for understanding the origin of the bias between SPECT and PET measurements. This finding is important for drug development and for the understanding and interpretation of imaging literature on D_2 RO.

7.3 A 4-year dopamine transporter (DAT) imaging study in neuroleptic-naive first episode schizophrenia patients

7.3.1 Aim of the study

Mané *et al* in 2011 presented a longitudinal study evaluating the course of DAT in schizophrenia. The main objective of the authors was to test the hypothesis that schizophrenia is associated with an accelerated loss of striatal DAT binding over the course of the illness.

7.3.2 Materials and methods

To test this hypothesis, the authors carried out a 4-year DAT SPECT follow-up clinical study with 14 patients and 7 controls.

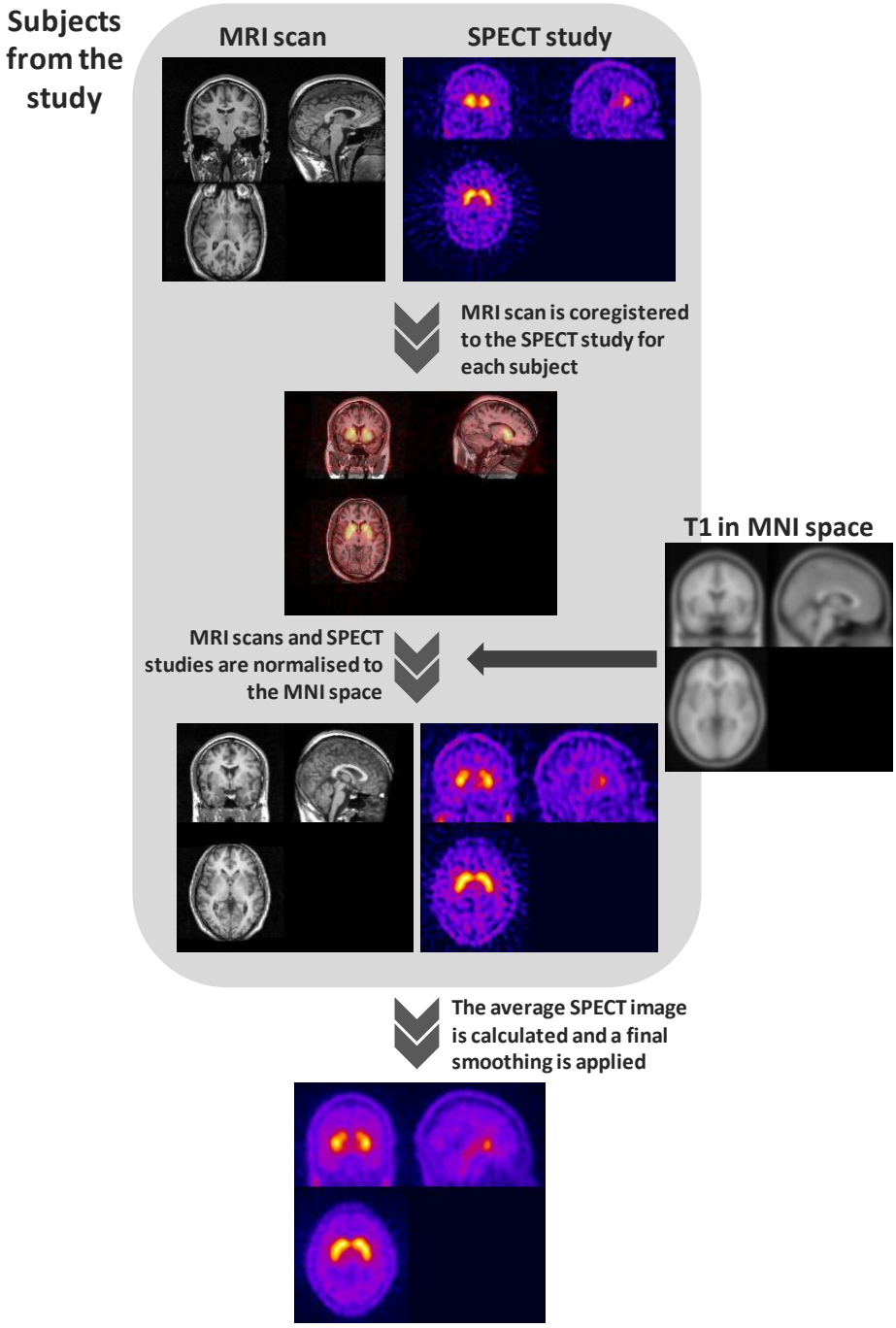

Figure 7.1 Steps followed to create the ^{123}I-FP-CIT SPECT template.

SPECT studies were acquired with an Elscint HELIX gamma camera equipped with a LEHR fan-beam collimator (see chapter 5 for a detailed description of the imaging system) and using ^{123}I-FP-CIT. Images were reconstructed elsewhere using FBP with a Metz filter for partial recovery of the spatial resolution and without additional corrections for degradations. A MRI follow-up study was also carried out.

To quantify the SPECT images, we created a ^{123}I-FP-CIT SPECT template from the subjects that took part in the study (see figure 7.1). The template was created following a number of steps. Firstly, MR images were coregistered to the SPECT images for each subject using SPM. Secondly, MR images were normalised to the T1-weighted template defined in the MNI standard space and the same transformations were applied to the SPECT images. Thirdly, normalised SPECT images were summed together and averaged out. Finally, a 3D Gaussian filter of 8 mm (Full Width Half Maximum) was applied to obtain a suitable template.

A total of 16 slices from the template were visually selected as representing the central part of the striatum. We defined the striatal ROIs and the reference ROI over the selected slices from the template. To quantify the striatal area, we drew six prismatic ROIs using the ImageJ software (area: 36 mm^2, height: 32 mm). ROIs were placed in caudate, anterior putamen and posterior putamen from each hemisphere. Additionally, an irregular reference ROI was drawn in the occipital cortex covering both hemispheres (area: 27.24 cm^2, height: 32 mm).

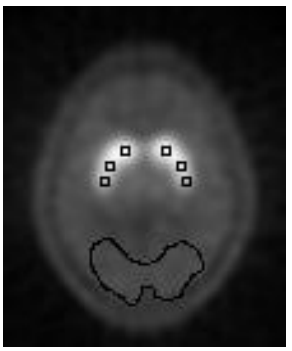

Figure 7.2 Central slice of the template showing the ROIs used to quantify the studies.

Each SPECT image was normalised to the template using SPM. The location of the striatal ROIs was manually adjusted, where necessary, for each study to fit the ROIs in the middle of the highest activity zones of caudate and putamen, far away from the edge to minimise PVE. Figure 7.2 shows a central slice of the SPECT template with the ROIs used to quantify the studies.

7.3.3 Discussion

^{123}I-FP-CIT SPECT images from 21 subjects were quantified in our laboratory using geometrical ROIs defined on a SPECT template. In this work, we adapted the methodology developed in chapter 6 for the semi-quantification of SPECT images based on standardised ROIs defined on a template to the resources available in a real clinical situation. Standardisation of the calculated values was not needed as they were compared with those values derived from control subjects obtained using the same procedure.

We chose to use geometrical ROIs to easily quantify the different regions of the putamen and obtain a variety of indexes to help in the study. This type of ROIs do not require a very accurate spatial normalisation of the SPECT images to the template, in contrast with the anatomical ROIs derived from the AAL map applied in chapter 6. Due to their simplicity and versatility, geometrical ROIs are commonly used to quantify images in clinical routine (Walker *et al* 2002, Varrone *et al* 2004, Mateos *et al* 2005).

In this longitudinal study, no differences were found in either overall striatal DAT binding or binding in striatal subregions (left and right caudate and putamen) over time between patients and controls. However, smaller differences in DAT binding over time were found in those patients with more negative symptoms at follow-up.

In this work, a clinical situation with real studies, both pathological and normal, was addressed with the use of the semi-quantification methodology presented in this doctoral dissertation.

7.4 Decreased striatal dopamine transporter uptake and substantia nigra hyperechogenicity as risk markers of synucleinopathy in patients with idiopathic rapid-eye-movement sleep behaviour disorder: a prospective study

7.4.1 Aim of the study

Iranzo *et al* in 2010 presented a prospective study assessing DAT uptake using ^{123}I-FP-CIT SPECT and echogenicity of the *substantia nigra* by use of transcranial sonography (TCS) in identified patients with idiopathic rapid-eye-movement sleep behaviour disorder (IRBD). IRBD patients can develop synucleinopathies associated with *substantia nigra* dysfunction such as PD, dementia with Lewy bodies and multiple system atrophy but, until present, identification of which patients with IRBD will develop these disorders is unknown. The authors hypothesised that neuroimaging findings such as decreased DAT uptake and midbrain hyperechogenicity, which are typical of early PD, might also occur in some patients with IRBD, who might then be at increased risk for development of a neurological syndrome.

7.4.2 Materials and methods

To prove this hypothesis, the authors carried out a prospective study with 43 patients with IRBD. Patients had both DAT imaging and TCS at baseline, and two and a half years later the number of patients who had developed a neurodegenerative syndrome was assessed. Results obtained from IRBD patients were compared with a group of healthy controls (18 controls for DAT imaging and 149 for TCS).

SPECT studies were acquired with a Siemens E.CAM gamma camera equipped with a LEHR collimator (see chapter 5 for a detailed description of the imaging system) and using ^{123}I-FP-CIT. SPECT images were reconstructed using FBP with a Butterworth filter and attenuation compensation using the Chang's method.

We quantified the SPECT images using a ^{123}I-FP-CIT SPECT template and a template of ROIs generated using the same methodology as in Mané *et al* 2011, which is described in section 7.3.2.

Evaluation of the calculated ratios was performed by comparison with those values corresponding to control subjects obtained using the same imaging system and following the same acquisition, reconstruction and quantification protocols. The specific striatal-to-occipital cortex uptake ratio was regarded as pathological when the value was less than two standard deviations of the mean ratio measured in controls.

7.4.3 Discussion

As in the previous clinical work, ^{123}I-FP-CIT SPECT images were processed in our laboratory using geometrical ROIs defined on a template. Since calculated values were compared with those values derived from control subjects obtained using the same procedure, standardisation of the measured values was not required.

This prospective study showed that only those patients with reduced DAT uptake or midbrain hyperechogenicity at baseline developed a synucleinopathy. On this basis, the authors suggested that combined DAT imaging and TCS is a potential strategy for early identification of IRBD individuals who are at increased short-term risk for development of synucleinopathies such as PD, dementia with Lewy bodies or multiple system atrophy.

In this clinical work, the main steps of the semi-quantification methodology presented in this doctoral dissertation were adapted to the resources and image processing programs available in a real clinical situation, finding a suitable alternative to overcome the limitations and extracting valid conclusions from the results.

Chapter 8

8 Conclusions

1. The SimSET MC code was adapted for the simulation of SPECT studies with ^{123}I-labelled radioligands. Once validated by comparing simulated and experimental projections of the anthropomorphic striatal phantom, it was used to simulate dopaminergic neurotransmission ^{123}I SPECT studies with different gamma cameras and collimators. The simulated projections obtained using the modified SimSET allow us to conclude that:

    a) An emission model which considers the low-energy line at 159 keV with a yield of 97% and one single high-energy line at 529 keV with a yield of 3%, permits the user to accurately simulate ^{123}I SPECT studies.

    b) The scatter contribution is strongly dependent on the imaging system employed, with values ranging from 43% for a Elscint HELIX gamma camera equipped with a LEHR fan-beam collimator to 51% for a Siemens E.CAM gamma camera equipped with a LEHR parallel collimator.

2. A new quantification method to provide absolute quantification in dopaminergic neurotransmission SPECT studies with ^{123}I was developed. The comparison between calculated and true SUR values derived from simulated studies showed that:

    a) Calculated SUR values depend on the imaging system when the quantification method does not include compensation for all degrading phenomena. However, a linear relationship between calculated and true SUR values was found regardless of the corrections applied.

b) PVE compensation plays a major role in the recovery of the true values. The proposed MC-based scatter compensation also plays an important part while PSF and attenuation corrections are the least significant.

c) The new quantification method, which includes compensation for all degradations, allows the theoretical SUR values to be reached, thereby enabling absolute quantification.

3. A methodology was developed to provide standardised semi-quantitative values in dopaminergic neurotransmission SPECT studies with ^{123}I in a clinical context. The comparison between calculated and true SUR values derived from simulated studies showed that:

a) Inter-subject anatomical variability does not compromise the general linear model between calculated and true values for any of the quantification methods applied in the study (ROIs derived from MRI and generic ROIs derived from the AAL map).

b) A simple linear model can be used to obtain standardised SUR values, although a multiple linear model which specifically accounts for the influence of PVE provides slightly higher accuracy and lower variability.

c) Reconstruction and quantification methods have a high impact on the linearity of the relationship between calculated and true values and on the accuracy of the standardised results.

Bibliography

Abi-Dargham A, Gil R, Krystal J, Baldwin RM, Seibyl JP, Bowers M, van Dyck CH, Charney DS, Innis RB, Laruelle M. Increased striatal dopamine transmission in schizophrenia: confirmation in a second cohort. Am J Psychiatry. 1998;155(6):761-767. PubMed PMID: 9619147

Abi-Dargham A, Rodenhiser J, Printz D, Zea-Ponce Y, Gil R, Kegeles LS, Weiss R, Cooper TB, Mann JJ, Van Heertum RL, Gorman JM, Laruelle M. Increased baseline occupancy of D2 receptors by dopamine in schizophrenia. Proc Natl Acad Sci U S A. 2000;97(14):8104-8109. PubMed PMID: 10884434

Aguiar P, Pareto D, Gispert JD, Crespo C, Falcón C, Cot A, Lomeña F, Pavía J, Ros D. Effect of anatomical variability, reconstruction algorithms and scattered photons on the SPM output of brain PET studies. Neuroimage. 2008;39(3):1121-1128. PubMed PMID: 18042402

Amara SG, Kuhar MJ. Neurotransmitter transporters: recent progress. Annu Rev Neurosci. 1993;16:73–93. Review. PubMed PMID: 8096377

Andreasen NC, Olsen S. Negative v positive schizophrenia. Definition and validation. Arch Gen Psychiatry. 1982;39(7):789-794. PubMed PMID: 7165478

Anger HO. Scintillation camera. Rev Sci Instrum. 1958;29(1):27–33. DOI: 10.1063/1.1715998

Asenbaum S, Brücke T, Pirker W, Podreka I, Angelberger P, Wenger S, Wöber C, Müller C, Deecke L. Imaging of dopamine transporters with iodine-123-β-CIT and SPECT in Parkinson's disease. J Nucl Med. 1997;38(1):1–6. PubMed PMID: 8998140

Assié K, Dieudonné A, Gardin I, Véra P, Buvat I. A preliminary study of quantitative protocols in Indium 111 SPECT using computational simulations and phantoms. IEEE Trans Nucl Sci. 2010;57(3):1096–1104. DOI: 10.1109/TNS.2010.2041252

Badiavas K, Molyvda E, Iakovou I, Tsolaki M, Psarrakos K, Karatzas N. SPECT imaging evaluation in movement disorders: far beyond visual assessment. Eur J Nucl Med Mol Imaging. 2011;38(4):764–773. PubMed PMID: 21125269

Beekman FJ, Viergever MA. Fast SPECT simulation including object shape dependent scatter. IEEE Trans Med Imaging. 1995;14(2):271–282. DOI: 10.1109/42.387709

Beekman FJ, Kamphuis C, Frey EC. Scatter compensation methods in 3D iterative SPECT reconstruction: a simulation study. Phys Med and Biol. 1997;42(8):1619–1632. PubMed PMID: 9279910

Beekman FJ, de Jong HW, van Geloven S. Efficient fully 3-D iterative SPECT reconstruction with Monte Carlo-based scatter compensation. IEEE Trans Med Imaging. 2002;21(8):867–877. PubMed PMID: 12472260

Belanger MJ, Dobrzeniecki AB, Yanch JC. The SimSPECT simulation system. In: Ljungberg M, Strand SE, King MA, editors. Monte Carlo calculations in nuclear medicine. Bristol, Philadelphia: IOP Publishing. 1998;111–124.

Benamer TS, Patterson J, Grosset DG, Booij J, de Bruin K, van Royen E, Speelman JD, Horstink MH, Sips HJ, Dierckx RA, Versijpt J, Decoo D, Van Der Linden C, Hadley DM, Doder M, Lees AJ, Costa DC, Gacinovic S, Oertel WH, Pogarell O, Hoeffken H, Joseph K, Tatsch K, Schwarz J, Ries V. Accurate differentiation of parkinsonism and essential tremor using visual assessment of [123I]-FP-CIT SPECT imaging: the [123I]-FP-CIT study group. Mov Disord. 2000;15(3):503–510. PubMed PMID: 10830416

Bezard E, Dovero S, Prunier C, Ravenscroft P, Chalon S, Guilloteau D, Crossman AR, Bioulac B, Brotchie JM, Gross CE. Relationship between the appearance of symptoms and the level of nigrostriatal degeneration in a progressive 1-methyl-4-phenyl-1,2,3,6-tetrahydropyridine-lesioned macaque model of Parkinson's disease. J Neurosci. 2001;21(17):6853–6861. PubMed PMID: 11517273

Booij J, Tissingh G, Winogrodzka A, van Royen EA. Imaging of the dopaminergic neurotransmission system using single-photon emission tomography and positron emission tomography in patients with parkinsonism. Eur J Nucl Med. 1999;26(2):171–182. PubMed PMID: 9933352

Booij J, Speelman JD, Horstink MW, Wolters EC. The clinical benefit of imaging striatal dopamine transporters with [123I]FP-CIT SPET in differentiating patients with presynaptic parkinsonism from those with other forms of parkinsonism. Eur J Nucl Med. 2001;28(3):266–272. PubMed PMID: 11315592

Bose SK, Turkheimer FE, Howes OD, Mehta MA, Cunliffe R, Stokes PR, Grasby PM. Classification of schizophrenic patients and healthy controls using [18F] fluorodopa PET imaging. Schizophr Res. 2008;106(2-3):148-155. PubMed PMID: 18849151

Bowsher JE, Floyd CE Jr. Treatment of Compton scattering in Maximum-Likelihood, Expectation-Maximization reconstructions of SPECT images. J Nucl Med. 1991;32(6):1285-1291. PubMed PMID: 2045948

Bradshaw J, Burnham C, Correia J, Rogers WL, Clinthorne NH. Application of Monte Carlo methods to the design of SPECT detector systems. IEEE Trans Nucl Sci. 1985;32(1):753–757. DOI: 10.1109/TNS.1985.4336936

Brooks DJ. Diagnosis and management of atypical parkinsonian syndromes. J Neurol Neurosurg Psychiatry. 2002;72(suppl 1):i10-i16. DOI: 10.1136/jnnp.72.suppl_1.i10

Brown WD, Taylor MD, Roberts AD, Oakes TR, Schueller MJ, Holden JE, Malischke LM, DeJesus OT, Nickles RJ. FluoroDOPA PET shows the nondopaminergic as well as dopaminergic destinations of levodopa. Neurology. 1999;53(6):1212-1218. PubMed PMID: 10522875

Bullich S, Ros D, Pavía J, Penengo M, Mateos J, Falcón C, Danús M, Perich X, Lomeña F, Catafau A. Influence of co-registration algorithms on I-123-IBZM SPET imaging quantification. Eur J Nucl Med Mol Imaging. 2004;31(Suppl):S49.

Bullich S, Cot A, Gallego J, Gunn RN, Suárez M, Pavía J, Ros D, Laruelle M, Catafau AM. Impact of scatter correction on D_2 receptor occupancy measurements using ^{123}I-IBZM SPECT: Comparison to ^{11}C-Raclopride PET. Neuroimage. 2010;50(4):1511-1518. DOI: 10.1016/j.neuroimage.2010.01.013

Buvat I, Castiglioni I. Monte Carlo simulations in SPET and PET. Q J Nucl Med. 2002;46(1):48–61.

Buvat I, Lazaro D. Monte Carlo simulations in emission tomography and GATE: An overview. Nucl Instrum Meth A. 3rd International Conference on Imaging Technologies in Biomedical Sciences. 2006;323–329.

Buvat I. Quantification in emission tomography: Challenges, solutions, and performance. Nucl Instrum Meth A. 2007;571(1–2):10–13.

Calvini P, Rodriguez G, Inguglia F, Mignone A, Guerra UP, Nobili F. The basal ganglia matching tools package for striatal uptake semi-quantification: description and validation. Eur J Nucl Med Mol Imaging. 2007;34(8):1240–1253. PubMed PMID: 17287959

Catafau AM, Tolosa E. Impact of dopamine transporter SPECT using 123I-Ioflupane on diagnosis and management of patients with clinically uncertain Parkinsonian syndromes. Mov Disord. 2004;19(10):1175-1182. PubMed PMID: 15390019

Catafau AM, Bullich S, Danús M, Penengo MM, Cot A, Abanades S, Farré M, Pavía J, Ros D. Test–retest variability and reliability of 123I-IBZM SPECT measurement of striatal dopamine D2 receptor availability in healthy volunteers and influence of iterative reconstruction algorithms. Synapse. 2008;62(1):62–69. PubMed PMID: 17960766

Catafau AM, Suarez M, Bullich S, Llop J, Nucci G, Gunn RN, Brittain C, Laruelle M. Within-subject comparison of striatal D2 receptor occupancy measurements using [123I]IBZM SPECT and [11C]Raclopride PET. NeuroImage. 2009;46(2):447–458. DOI: 10.1016/j.neuroimage.2009.02.005

Chang LT. A method for attenuation correction in radionuclide computed tomography. IEEE Trans Nucl Sci. 1978;25(1):638–643. DOI: 10.1109/TNS.1978.4329385

Chang LT. Attenuation correction and incomplete projection in single photon emission computed tomography. IEEE Trans Nucl Sci. 1979;26(2):2780–2789. DOI: 10.1109/TNS.1979.4330536

Chornoboy ES, Chen CJ, Miller MI, Miller TR, Snyder DL. An evaluation of maximum likelihood reconstruction for SPECT. IEEE Trans Med Imaging. 1990;9(1):99–110. DOI: 10.1109/42.52987

Cot A, Sempau J, Pareto D, Bullich S, Pavía J, Calviño F, Ros D. Evaluation of the geometric, scatter and septal penetration components in fan-beam collimators using Monte Carlo simulation. IEEE Trans Nucl Sci. 2002;49(1):12–16.
DOI: 10.1109/TNS.2002.998674

Cot A. Absolute quantification in brain SPECT imaging. Doctoral thesis. Universitat Politècnica de Barcelona. 2003.

Cot A, Sempau J, Pareto D, Bullich S, Pavía J, Calviño F, Ros D. Study of the point spread function (PSF) for 123I SPECT imaging using Monte Carlo simulation. Phys Med Biol. 2004;49(14):3125–3136. PubMed PMID: 15357186

Cot A, Falcón C, Crespo C, Sempau J, Pareto D, Bullich S, Lomeña F, Calviño F, Pavía J, Ros D. Absolute quantification in dopaminergic neurotransmission SPECT using a Monte Carlo-based scatter correction and fully 3-dimensional reconstruction. J Nucl Med. 2005;46(9):1497–1504. PubMed PMID: 16157533

Cot A, Jané E, Sempau J, Falcón C, Bullich S, Pavía J, Calviño, Ros D. Modeling of high-energy contamination in SPECT imaging using Monte Carlo simulation. IEEE Trans Nucl Sci. 2006;53(1):198–203. DOI: 10.1109/TNS.2006.870174

Counihan TJ, Penney JB. Regional dopamine transporter gene expression in the substantia nigra from control and Parkinson's disease brains. J Neurol Neurosurg Psychiatry. 1998;65(2):164–169. PubMed PMID: 9703165

Crespo C, Gallego J, Cot A, Falcón C, Bullich S, Pareto D, Aguiar P, Sempau J, Lomeña F, Calviño F, Pavía J, Ros D. Quantification of dopaminergic neurotransmission SPECT studies with 123I-labelled radioligands. A comparison between different imaging systems and data acquisition protocols using Monte Carlo simulation. Eur J Nucl Med Mol Imaging. 2008;35(7):1334–1342. DOI: 10.1007/s00259-007-0711-z

Darcourt J, Booij J, Tatsch K, Varrone A, Vander Borght T, Kapucu OL, Nagren K, Nobili F, Walker Z, Van Laere K. EANM procedure guidelines for brain neurotransmission SPECT using ^{123}I-labelled dopamine transporter ligands, version 2. Eur J Nucl Med Mol Imaging. 2010;37(2):443–450. DOI: 10.1007/s00259-009-1267-x

De Vries DJ, Moore SC; Zimmerman RE, Mueller SP, Friedland B, Lanza RC. Development and validation of a Monte Carlo simulation of photon transport in an Anger camera. IEEE Trans Med Imaging. 1990;9(4):430–438. PubMed PMID: 18222790

Dewaraja YK, Ljungberg M, Koral KF. Monte Carlo evaluation of object shape effects in iodine-131 SPET tumor activity quantification. Eur J Nucl Med. 2001;28(7):900–906. PubMed PMID: 11504087

Dickson JC, Tossici-Bolt L, Sera T, de Nijs R, Booij J, Bagnara MC, Seese A, Koulibaly PM, Akdemir UO, Jonsson C, Koole M, Raith M, Lonsdale MN, George J, Zito F, Tatsch K. Proposal for the standardisation of multi-centre trials in nuclear medicine imaging: prerequisites for a European 123I-FP-CIT SPECT database. Eur J Nucl Med Mol Imaging. 2012;39(1):188-197. DOI: 10.1007/s00259-011-1884-z

Dobbeleir AA, Hambÿe AS, Franken PR. Influence of high-energy photons on the spectrum of iodine-123 with low- and medium-energy collimators: consequences for imaging with 123I-labelled compounds in clinical practice. Eur J Nucl Med. 1999;26(6): 655–658. PubMed PMID: 10369952

Du Y, Frey EC, Wang WT, Tocharoenchai C, Baird WH, Tsui BMW. Combination of MCNP and SimSET for Monte Carlo simulation of SPECT with medium- and high-energy photons. IEEE Trans Nucl Sci. 2002;49(3):668–674.
DOI: 10.1109/TNS.2002.1039547

Du Y, Tsui BMW, Frey EC. Partial volume effect compensation for quantitative brain SPECT imaging. IEEE Trans Med Imaging. 2005;24(8):969–976. PubMed PMID: 16092329

Du Y, Tsui BMW, Frey EC. Model-based compensation for quantitative 123I brain SPECT imaging. Phys Med Biol. 2006;51(5):1269-1282. PubMed PMID: 16481693

El Fakhri G, Kijewski MF, Moore SC. Absolute activity quantitation from projections using an analytical approach: comparison with iterative methods in Tc-99m and I-123 brain SPECT. IEEE Trans Nucl Sci. 2001;48(3):768–773. DOI: 10.1109/23.940161

Eshuis SA, Jager PL, Maguire RP, Jonkman S, Dierckx RA, Leenders KL. Direct comparison of FP-CIT SPECT and F-DOPA PET in patients with Parkinson's disease and healthy controls. Eur J Nucl Med Mol Imaging. 2009;36(3):454-462. DOI: 10.1007/s00259-008-0989-5

Fischman AJ, Alpert NM, Rubin RH. Pharmacokinetic imaging: a noninvasive method for determining drug distribution and action. Clin Pharmacokinet. 2002;41(8):581-602. PubMed PMID: 12102642

Fleming JS, Bolt L, Stratford JS, Kemp PM. The specific uptake size index for quantifying radiopharmaceutical uptake. Phys Med Biol. 2004;49(14):N227–N234. PubMed PMID: 15357202

Floyd CE Jr, Jaszczak RJ, Greer KL, Coleman RE. Inverse Monte Carlo as a unified reconstruction algorithm for ECT. J Nucl Med. 1986;27(10):1577–1585. PubMed PMID: 3489822

Frey EC, Tsui BMW. A practical method for incorporating scatter in a projector-backprojector for accurate scatter compensation in SPECT. IEEE Trans Nucl Sci. 1993;40(4):1107–1116. DOI: 10.1109/23.256720

Frey EC, Tsui BMW. A new method for modelling the spatially-variant, object dependent scatter response function in SPECT. Conf Rec. 1996. IEEE Nuclear Science Symposium Medical Imaging Conf. (Piscataway, NJ) pp 1035-1307.

Frey EC, Tsui BMW, Gullberg GT. Improved estimation of the detector response function for converging beam collimators. Phys Med Biol. 1998;43(4):941–950. PubMed PMID: 9572517

Frey KA. Can SPET imaging of dopamine uptake sites replace PET imaging in Parkinson's disease? Against. Eur J Nucl Med Mol Imaging. 2002;29(5):715-717.

Frouin V, Comtat C, Reilhac A, Grégoire MC. Correction of partial-volume effect for PET striatal imaging: fast implementation and study robustness. J Nucl Med. 2002;43(12):1715–1726. PubMed PMID: 12468524

Gallego J, Niñerola-Baizán A, Cot A, Aguiar P, Crespo C, Falcón C, Lomeña F, Sempau J, Pavía J, Ros D. Validation of semi-quantitative methods for DAT SPECT: influence of anatomical variability and partial volumen effect. Phys Med Biol. 2015;60(15):5925-5938. DOI: 10.1088/0031-9155/60/15/5925

GEANT4 home page. http://geant4.web.cern.ch/geant4/

Gerasimou G, Tsolaki M, Bostanjopoulou S, Liaros G, Papanastasiou E, Balaris V, Katsarou Z, Fotiou F, Dedousi E, Baloyannis S, Milonas I. Findings from molecular imaging with SPET camera and 123I-ioflupane in the differential diagnosis of Parkinsonism and essential tremor. Hell J Nucl Med. 2005;8(2):81–85. PubMed PMID: 16142248

Gilman S, Wenning GK, Low PA, Brooks DJ, Mathias CJ, Trojanowski JQ, Wood NW, Colosimo C, Dürr A, Fowler CJ, Kaufmann H, Klockgether T, Lees A, Poewe W, Quinn N, Revesz T, Robertson D, Sandroni P, Seppi K, Vidailhet M. Second consensus statement on the diagnosis of multiple system atrophy. Neurology. 2008;71(9):670-676. DOI: 10.1212/01.wnl.0000324625.00404.15

Giros B, Caron MG. Molecular characterization of the dopamine transporter. Trends Pharmacol Sci. 1993;14(2):43–49. PubMed PMID: 8480373

Gold JM, Harvey PD. Cognitive deficits in schizophrenia. Psychiatr Clin North Am. 1993;16(2):295-312. PubMed PMID: 8332566

Guilland DR, Jaszczak RJ, Wang H, Turkington TG, Greer KL, Coleman RE. A 3D model of non-uniform attenuation and detector response for efficient iterative reconstruction in SPECT. Phys Med Biol. 1994;39(3):547–561. PubMed PMID: 15551597

Habraken JB, Booij J, Slomka P, Sokole EB, van Royen EA. Quantification and visualization of defects of the functional dopaminergic system using an automatic algorithm. J Nucl Med. 1999;40(7):1091–1097. PubMed PMID: 10405125

Halbleib JA, Kensek RP, Mehlhorn TA, Valdez GD, Seltzer SM, Berger MJ. ITS Version 3.0: the integrated TIGER series of coupled electron/photon Monte Carlo transport codes. Sandia National Laboratories. Tech Rep. 1992; SAND91–1634.

Halldin C, Gulyás B, Langer O, Farde L. Brain radioligands - State of the art and new trends. Q J Nucl Med. 2001;45(2):139–152. PubMed PMID: 11476163

Haynor DR, Harrison RL, Lewellen TK. The use of importance sampling techniques to improve the efficiency of photon tracking in emission tomography simulations. Med Phys. 1991;18(5):990-1001. PubMed PMID: 1961165

Haynor DR, Kaplan MS, Miyaoka RS, Lewellen TK. Multiwindow scatter correction techniques in single-photon imaging. Med Phys. 1995;22(12):2015–2024. PubMed PMID: 8746706

Hietala J, Syvälahti E, Vuorio K, Räkköläinen V, Bergman J, Haaparanta M, Solin O, Kuoppamäki M, Kirvelä O, Ruotsalainen U, et al. Presynaptic dopamine function in striatum of neuroleptic-naive schizophrenic-patients. Lancet. 1995;346(8983): 1130–1131. PubMed PMID: 7475604

Howes OD, Kapur S. The dopamine hypothesis of schizophrenia: version III—the final common pathway. Schizophr Bull. 2009;35(3):549–562. DOI: 10.1093/schbul/sbp006

Huang WS, Chiang YH, Lin JC, Chou YH, Cheng CY, Liu RS. Crossover study of ^{99m}Tc-TRODAT-1 SPECT and ^{18}F-FDOPA PET in Parkinson's disease patients. J Nucl Med. 2003;44(7):999–1005. PubMed PMID: 12843212

Hudson HM, Larkin RS. Accelerated image reconstruction using ordered subsets of projection data. IEEE Trans Med Imag. 1994;13(4):601–609. DOI: 10.1109/42.363108

Hutton BF, Buvat I, Beekman FJ. Review and current status of SPECT scatter correction. Phys Med Biol. 2011;56(14):R85–R112. DOI: 10.1088/0031-9155/56/14/R01

Ichihara T, Ogawa K, Motomura N, Kubo A, Hashimoto S. Compton scatter compensation using the triple-energy window method for single- and dual-isotope SPECT. J Nucl Med. 1993;34(12):2216–2221. PubMed PMID: 8254414

Iranzo A, Lomeña F, Stockner H, Valldeoriola F, Vilaseca I, Salamero M, Molinuevo JL, Serradell M, Duch J, Pavía J, Gallego J, Seppi K, Högl B, Tolosa E, Poewe W, Santamaria J. Decreased striatal dopamine transporter uptake and substantia nigra hyperechogenicity as risk markers of synucleinopathy in patients with idiopathic rapid-eye-movement sleep behaviour disorder: a prospective study. Lancet Neurol. 2010;9(11):1070-1077. DOI: 10.1016/S1474-4422(10)70216-7

Jaber M, Jones S, Giros B, Caron MG. The dopamine transporter: a crucial component regulating dopamine transmission. Mov Disord. 1997;12(5):629–633. PubMed PMID: 9380041

Johannsen B, Pietzsch HJ. Development of technetium-99m-based CNS receptor ligands: have there been any advances?. Eur J Nucl Med Mol Imaging. 2002;29(2):263–275. PubMed PMID: 11926389

Kadrmas DJ, Frey EC, Karimi SS, Tsui BMW. Fast implantation of reconstruction-based scatter compensation in fully 3D SPECT image reconstruction. Phys Med Biol. 1998;43(4):857–873. PubMed PMID: 9572510

Kamphuis C, Beekman FJ, Viergever MA. Evaluation of OS-EM vs. ML-EM for 1D, 2D and fully 3D SPECT reconstruction. IEEE Trans Nucl Sci. 1996;43(3):2018–2024. DOI: 10.1109/23.507262

Kamphuis C, Beekman FJ, van Rijk PP, Viergever MA. Dual matrix ordered subset reconstruction for accelerated 3D scatter correction in single-photon emission tomography. Eur J Nucl Med. 1998;25(1):8–18. PubMed PMID: 9396869

Kaplan MS, Harrison RL, Vannoy SD. Coherent scatter implementation for SimSET. IEEE Trans Nucl Sci. 1998;45(6):3064–3068. DOI: 10.1109/23.737665

Kish SJ, Shannak K, Hornykiewicz O. Uneven pattern of dopamine loss in the striatum of patients with idiopathic Parkinson's disease. Pathophysiologic and clinical implications. N Engl J Med. 1988;318(14):876–880. PubMed PMID: 3352672

Koch W, Hamann C, Welsch J, Pöpperl G, Radau PE, Tatsch K. Is iterative reconstruction an alternative to filtered backprojection in routine processing of dopamine transporter SPECT studies? J Nucl Med. 2005;46(11):1804-1811. PubMed PMID: 16269593

Koch W, Radau PE, Münzing W, Tatsch K. Cross-camera comparison of SPECT measurements of a 3-D anthropomorphic basal ganglia phantom. Eur J Nucl Med Mol Imaging. 2006;33(4):495–502. PubMed PMID: 16435116

Koch W, Mustafa M, Zach C, Tatsch K. Influence of movement on FP-CIT SPECT quantification: a Monte Carlo based simulation. Nucl Med Commun. 2007a;28(8):603–614.

Koch W, Hamann C, Radau PE, Tatsch K. Does combined imaging of the pre- and postsynaptic dopaminergic system increase the diagnostic accuracy in the differential diagnosis of parkinsonism? Eur J Nucl Med Mol Imaging. 2007b;34(8):1265–1273. PubMed PMID: 17318547

Koole M, Laere KV, de Walle RV, Vandenberghe S, Bouwens L, Lemahieu I, Dierckx RA. MRI guided segmentation and quantification of SPECT images of the basal ganglia: a phantom study. Comput Med Imaging Graph. 2001;25(2):165–172. PubMed PMID: 11137793

Kumakura Y, Cumming P, Vernaleken I, Buchholz HG, Siessmeier T, Heinz A, Kienast T, Bartenstein P, Gründer G. Elevated [18F]fluorodopamine turnover in brain of patients with schizophrenia: an [18F]fluorodopa/positron emission tomography study. J Neurosci. 2007;27(30):8080-8087. PubMed PMID: 17652599

Lange K, Carson R. EM reconstruction algorithms for emission and transmission tomography. J Comput Assist Tomogr. 1984;8(2):306–316. PubMed PMID: 6608535

Laruelle M, Abi-Dargham A, van Dyck CH, Gil R, D'Souza CD, Erdos J, McCance E, Rosenblatt W, Fingado C, Zoghbi SS, Baldwin RM, Seibyl JP, Krystal JH, Charney DS, Innis RB. Single photon emission computerized tomography imaging of amphetamine-induced dopamine release in drug-free schizophrenic subjects. Proc Natl Acad Sci U S A. 1996; 93(17):9235-9240. PubMed PMID: 8799184

Laruelle M, Abi-Dargham A, van Dyck C, Gil R, D'Souza DC, Krystal J, Seibyl J, Baldwin R, Innis R. Dopamine and serotonin transporters in patients with schizophrenia: an imaging study with [(123)I]beta-CIT. Biol Psychiatry. 2000;47(5):371-379. PubMed PMID: 10704949

Lazaro D, El Bitar Z, Breton V, Hill D, Buvat I. Fully 3D Monte Carlo reconstruction in SPECT: a feasibility study. Phys Med Biol. 2005;50(16):3739-3754. PubMed PMID: 16077224

Lieberman JA, Kane JM, Alvir J. Provocative tests with psychostimulant drugs in schizophrenia. Psychopharmacology. 1987;91(4):415–433. DOI: 10.1007/BF00216006

Lindström LH, Gefvert O, Hagberg G, Lundberg T, Bergström M, Hartvig P, Langström B. Increased dopamine synthesis rate in medial prefrontal cortex and striatum in schizophrenia indicated by L-(β-^{11}C) DOPA and PET. Biol Psychiatry. 1999;46(5):681–688. PubMed PMID: 10472420

Ljungberg M, Strand SE. A Monte Carlo program for the simulation of scintillation camera characteristics. Comput Methods Programs Biomed. 1989;29(4):257–272. PubMed PMID: 2791527

Ljungberg M, Strand S. Scatter and attenuation correction in SPECT using density maps and Monte Carlo simulated scatter functions. J Nucl Med. 1990;31(9):1560–1567. PubMed PMID: 2395025

Lomeña F, Catafau AM, Parellada E, Bernardo M, Font M, Gutiérrez F, Pavía J. Striatal dopamine D2 recpetor density in neuroleptic-naive and in neuroleptic-free schizophrenic patients: an 123I-IBZM-SPECT study. Psychopharmacology (Berl). 2004;172(2):165-169. PubMed PIMD: 14624330

Lupton LR, Keller NA. Performance study of single-slice positron emission tomography scanners by Monte Carlo techniques. IEEE Trans Med Imaging. 1983;2(4):154–168. PubMed PMID: 18234601

Lyon GJ, Abi-Dargham A, Moore H, Lieberman JA, Javitch JA, Sulzer D. Presynaptic regulation of dopamine transmission in schizophrenia. Schizophr Bull. 2011;37(1):108–117. DOI: 10.1093/schbul/sbp010

Mahapatra RK, Edwards MJ, Schott JM, Bhatia KP. Corticobasal degeneration. Lancet Neurol. 2004;3(12):736-743. PubMed PMID: 15556806

Mané A, Gallego J, Lomeña F, Mateos JJ, Fernández-Egea E, Horga G, Cot A, Pavía J, Bernardo M, Parellada E. A 4-year dopamine transporter (DAT) imaging study in neuroleptic-naive first episode schizophrenia patients. Psychiatry Res. 2011;194(1):79-84. DOI: 10.1016/j.pscychresns.2011.03.004

Marsden CD. Parkinson's disease. J Neurol Neurosurg Psychiatry. 1994;57(6):672–681. DOI: 10.1136/jnnp.57.6.672

Marshall V, Grosset D. Role of dopamine transporter imaging in routine clinical practice. Mov Disord. 2003;18(12):1415–1423. PubMed PMID: 14673877

Mateos JJ, Lomeña F, Parellada E, Font M, Fernandez E, Pavia J, Prats A, Pons F, Bernardo M. Decreased striatal dopamine transporter binding assessed with [123I]FP-CIT in first-episode schizophrenic patients with and without short-term antipsychotic-induced parkinsonism. Psychopharmacology (Berl). 2005;181(2):401-406. PubMed PMID: 15830229

MCNP directory. https://mcnp.lanl.gov

Meikle SR, Hutton BF, Bailey DL. A transmission-dependent method for scatter correction in SPECT. J Nucl Med. 1994;35(2):360–367. PubMed PMID: 8295011

Metz CE, Beck RN. Quantitative effects of stationary linear image processing on noise and resolution of structure in radionuclide images. J Nucl Med. 1974;15(3):164–170. PubMed PMID: 4813223

Metz CE, Atkins FB, Beck RN. The geometric transfer function component for scintillation camera collimators with straight parallel holes. Phys Med Biol. 1980;25(6):1059–1070. PubMed PMID: 7208618

Murray D. Using EGS4 Monte Carlo in medical radiation physics. Australas Phys Eng Sci Med. 1990;13(3):132–147. PubMed PMID: 2173530

Neumeyer JL, Wang S, Gao Y, Milius RA, Kula NS, Campbell A, Baldessarini RJ, Zea-Ponce Y, Baldwin RM, Innis RB. N-omega-fluoroalkyl analogs of (1R)-2 beta-carbomethoxy-3-beta-(4-iodophenyl)-tropane (beta-CIT) - radiotracers for positron emission tomography and single-photon emission computed-tomography imaging of dopamine transporters. J Med Chem. 1994;37(11):1558–1561. PubMed PMID: 8201589

Nussbaum RL, Ellis CE. Alzheimer's disease and Parkinson's disease. N Engl J Med. 2003;348(14):1356–1364. PubMed PMID: 12672864

Ogawa K, Harata Y, Ichihara T, Kubo A, Hashimoto S. A practical method for position-dependent Compton-scatter correction in Single Photon Emission CT. IEEE Trans Med Imaging. 1991;10(3):408–412. PubMed PMID: 18222843

Pareto D, Cot A, Falcón C, Juvells I, Pavía J, Ros D. Geometrical response modeling in fan-beam collimators - A numerical simulation. IEEE Trans Nucl Sci. 2002;49(1):17– 24. DOI: 10.1109/TNS.2002.998675

Pareto D, Cot A, Pavía J, Falcón C, Juvells I, Lomeña F, Ros D. Iterative reconstruction with correction of the spatially variant fan-beam collimator response in neurotransmission SPET imaging. Eur J Nucl Med Mol Imaging. 2003;30(10):1322–1329. PubMed PMID: 12845485

Patenaude B, Smith SM, Kennedy DN, Jenkinson M. A Bayesian model of shape and appearance for subcortical brain segmentation. Neuroimage. 2011;56(3):907–922. DOI: 10.1016/j.neuroimage.2011.02.046

Pavia J, Ros D, Catafau AM, Lomeña FJ, Huguet M, Setoain J. Three-dimensional realignment of activation brain single-photon emission tomographic studies. Eur J Nucl Med. 1994;21(12):1298-1302. PubMed PMID: 7875167

PENELOPE home page. http://www.oecd-nea.org/lists/penelope.html

Perälä J, Suvisaari J, Saarni SI, Kuoppasalmi K, Isometsä E, Pirkola S, Partonen T, Tuulio-Henriksson A, Hintikka J, Kieseppä T, Härkänen T, Koskinen S, Lönnqvist J. Lifetime prevalence of psychotic an bipolar I disorders in a general population. Arch Gen Psychiatry. 2007;64(1):19-28. PubMed PMID: 17199051

Plotkin M, Amthauer H, Klaffke S, Kühn A, Lüdemann L, Arnold G, Wernecke KD, Kupsch A, Felix R, Venz S. Combined 123I-FP-CIT and 123I-IBZM SPECT for the diagnosis of parkinsonian syndromes: study on 72 patients. J Neural Transm. 2005;112(5):677-692. PubMed PMID: 15375677

Quarantelli M, Berkouk K, Prinster A, Landeau B, Svarer C, Balkay L, Alfano B, Brunetti A, Baron JC, Salvatore M. Integrated software for the analysis of brain PET/SPECT studies with partial-volume-effect correction. J Nucl Med. 2004;45(2):192–201. PubMed PMID: 14960635

Rault E, Staelens S, Van Holen R, De Beenhouwer J, Vandenberghe S. Accurate Monte Carlo modelling of the back compartments of SPECT cameras. Phys Med Biol. 2011;56(1):87-104. DOI: 10.1088/0031-9155/56/1/006

Reith J, Benkelfat C, Sherwin A, Yasuhara Y, Kuwabara H, Andermann F, Bachneff S, Cumming P, Diksic M, Dyve SE, Etienne P, Evans AC, Lal S, Shevell M, Savard G, Wong DF, Chouinard G, Gjedde A. Elevated dopa decarboxylase activity in living brain of patients with psychosis. Proc Natl Acad Sci U S A. 1994;91(24):11651–11654. PubMed PMID: 7972118

Riauka TA, Gortel ZW. Photon propagation and detection in single-photon emission computed tomography — an analytical approach. Med Phys. 1994;21(8):1311–1321. PubMed PMID: 7799876

Roé N. Evaluation of Compton scattering in SPECT studies with ^{123}I-labeled radiotracers and quantification of small animal neurotransmission studies. Doctoral thesis. Universitat de Barcelona. 2011.

Rogers DW. Fifty years of Monte Carlo simulations for medical physics. Phys Med Biol. 2006;51(13):R287–301. PubMed PMID: 16790908

Rojas GM, Raff U, Quintana JC, Huete I, Hutchinson M. Image fusion in neuroradiology: three clinical examples including MRI of Parkinson disease. Comput Med Imaging Graph. 2007;31(1):17–27. PubMed PMID: 17150328

Rousset OG, Ma Y, Evans AC. Correction for partial volume effects in PET: principle and validation. J Nucl Med. 1998;39(5):904–911. PubMed PMID: 9591599

Schmitt GJ, Meisenzahl EM, Frodl T, La FC, Hahn K, Moller HJ, Dresel S. The striatal dopamine transporter in first-episode, drug-naive schizophrenic patients: evaluation by the new SPECT-ligand [^{99m}Tc]TRODAT-1. J Psychopharmacol. 2005;19(5):488-493. DOI: 10.1177/0269881105056530

Schreckenberger M, Hägele S, Seissmeier T, Buchholz HG, Armbrust-Henrich H, Rösch F, Gründer G, Bartenstein P, Vogt T. The dopamine D2 receptor ligand 18F-desmethoxyfallypride: an appropriate fluorinated PET tracer for the differential diagnosis of parkinsonism. Eur J Nucl Med Mol Imaging. 2004;31(8):1128-1135. PubMed PMID: 15042325

Seeman P, Lee T. Antipsychotic drugs: direct correlation between clinical potency and presynaptic action on dopamine neurons. Science. 1975;188(4194):1217–1219. PubMed PMID: 1145194

Seibyl JP, Marek KL, Quinlan D, Sheff K, Zoghbi S, Zea-Ponce Y, Baldwin RM, Fussell B, Smith EO, Charney DS, van Dyck C, et al. Decreased single-photon emission computed tomographic [123I]beta-CIT striatal uptake correlates with symptom severity in Parkinson's disease. Ann Neurol. 1995;38(4):589–598. PubMed PMID: 7574455

Seibyl JP, Marek K, Sheff K, Baldwin RM, Zoghbi S, Zea-Ponce Y, Charney DS, van Dyck CH, Hoffer PB, Innis RB. Test/retest reproducibility of iodine-123-beta CIT SPECT brain measurement of dopamine transporters in Parkinson's patients. J Nucl Med. 1997;38(9):1453–1459. PubMed PMID: 9293807

Shepp LA, Vardi Y. Maximum likelihood reconstruction for emission tomography. IEEE Trans Med Imaging. 1982;1(2):113–122. PubMed PMID: 18238264

Smith MF, Floyd CE, Jaszczak RJ. A vectorized Monte Carlo code for modeling photon transport in SPECT. Med Phys. 1993;20(4):1121–1127. PubMed PMID: 8413021

Song X, Segars WP, Du Y, Tsui BMW, Frey EC. Fast modelling of collimator-detector response in Monte Carlo simulation of SPECT imaging using the angular response function. Phys Med Biol. 2005;50(8):1791–1804. PubMed PMID: 15815096

Soret M, Koulibaly PM, Darcourt J, Hapdey S, Buvat I. Quantitative accuracy of dopaminergic neurotransmission imaging with ^{123}I SPECT. J Nucl Med. 2003;44(7):1184–1193. PubMed PMID: 12843235

Soret M, Alaoui J, Koulibaly PM, Darcourt J, Buvat I. Accuracy of partial volume effect correction in clinical molecular imaging of dopamine transporter using SPECT. Nucl Instrum Meth A. 2007;571(1-2):173–176. DOI: 10.1016/j.nima.2006.10.236

Staelens S, de Wit T, Beekman F. Fast hybrid SPECT simulation including efficient septal penetration modelling (SP-PSF). Phys Med Biol. 2007;52(11):3027–3043. PubMed PMID: 17505087

Talvik M, Nordström AL, Okubo Y, Olsson H, Borg J, Halldin C, Farde L. Dopamine D2 receptor binding in drug-naïve patients with schizophrenia examined with raclopride-C11 and positron emission tomography. Psychiatry Res. 2006; 148(2-3):165-173. PubMed PMID: 17095199

Tatsch K. Imaging of the dopaminergic system in parkinsonism with SPET. Nucl Med Commun. 2001;22(7):819–827. PubMed PMID: 11453057

Tossici-Bolt L, Hoffmann SM, Kemp PM, Mehta RL, Fleming JS. Quantification of [123I]FP-CIT SPECT brain images: an accurate technique for measurement of the specific binding ratio. Eur J Nucl Med Mol Imaging. 2006;33(12):1491–1499. PubMed PMID: 16858570

Tossici-Bolt L, Dickson JC, Sera T, Varrone A, Tatsch K. SPECT imaging of a ^{123}I striatal phantom on different cameras: relevance of scatter and septal penetration correction to quantification accuracy. Eur J Nucl Med Mol Imaging. 2008;35(2):S216.

Tossici-Bolt L, Dickson JC, Sera T, de Nijs R, Bagnara MC, Jonsson C, Scheepers E, Zito F, Seese A, Koulibaly PM, Kapucu OL, Koole M, Raith M, George J, Lonsdale MN, Münzing W, Tatsch K, Varrone A. Calibration of gamma camera systems for a multicentre European ^{123}I-FP-CIT SPECT normal database. Eur J Nucl Med Mol Imaging. 2011;38(8):1529-1540. DOI: 10.1007/s00259-011-1801-5

Tsuang M. Schizophrenia: genes and environment. Biol Psychiatry. 2000;47(3):210-220. PubMed PMID: 10682218

Tsui BMW, Gullberg GT. The geometric transfer function for cone and fan beam collimators. Phys Med Biol. 1990;35(1):81–93.

Tzourio-Mazoyer N, Landeau B, Papathanassiou D, Crivello F, Etard O, Delcroix N, Mazoyer B, Joliot M. Automated anatomical labeling of activations in SPM using a macroscopic anatomical parcellation of the MNI MRI single-subject brain. Neuroimage. 2002;15(1):273-289. PubMed PMID: 11771995

Uhl GR, Walther D, Mash D, Faucheux B, Javoy-Agid F. Dopamine transporter messenger RNA in Parkinson's disease and control substantia nigra neurons. Ann Neurol. 1994;35(4):494–498. PubMed PMID: 8154880

van der Wee NJ, van Veen JF, Stevens H, van Vliet IM, van Rijk PP, Westenberg HG. Increased serotonin and dopamine transporter binding in psychotropic medication-naive patients with generalized social anxiety disorder shown by 123I-beta-(4-iodophenyl)-tropane SPECT. J Nucl Med. 2008;49(5):757–763. DOI: 10.2967/jnumed.107.045518

van Laere K, Varrone A, Booij J, Vander Borght T, Nobili F, Kapucu OL, Walker Z, Nagren K, Tatsch K, Darcourt J. EANM procedure guidelines for brain neurotransmission SPECT/PET using dopamine D2 receptor ligands, version 2. Eur J Nucl Med Mol Imaging. 2010;37(2):434-442. DOI: 10.1007/s00259-009-1265-z

Vanzi E, De Cristofaro MT, Ramat S, Sotgia B, Mascalchi M, Formiconi AR. A direct ROI quantification method for inherent PVE correction: accuracy assessment in striatal SPECT measurements. Eur J Nucl Med Mol Imaging. 2007;34(9):1480–1489. PubMed PMID: 17390134

Varrone A, Marek KL, Jennings D, Innis RB, Seibyl JP. [^{123}I]beta-CIT SPECT imaging demonstrates reduced density of striatal dopamine transporters in Parkinson's disease and multiple system atrophy. Mov Disord. 2001;16(6):1023-1032. PubMed PMID: 11748733

Varrone A, Salvatore E, De Michele G, Barone P, Sansone V, Pellecchia MT, Castaldo I, Coppola G, Brunetti A, Salvatore M, Pappatà S, Filla A. Reduced striatal [123I]FP-CIT binding in SCA2 patients without parkinsonism. Ann Neurol. 2004; 55(3):426–430. PubMed PMID: 14991822

Varrone A, Dickson JC, Tossici-Bolt L, Sera T, Asenbaum S, Booij J, Kapucu OL, Kluge A, Knudsen GM, Koulibaly PM, Nobili F, Pagani M, Sabri O, Vander Borght T, Van Laere K, Tatsch K. European multicentre database of healthy controls for [123I]FP-CIT SPECT (ENC-DAT): age-related effects, gender differences and evaluation of different methods of analysis. Eur J Nucl Med Mol Imaging. 2013;40(2):213–227. DOI: 10.1007/s00259-012-2276-8

Verhoeff NP, Kapucu O, Sokole-Busemann E, van Royen EA, Janssen AG. Estimation of dopamine D2 receptor binding potential in the striatum with iodine-123-IBZM SPECT: technical and interobserver variability. J Nucl Med. 1993;34(12):2076–2084. PubMed PMID: 8254390

Walker E, Kestler L, Bollini A, Hochman KM. Schizophrenia: etiology and course. Annu Rev Psychol. 2004;55:401-430. PubMed PMID: 14744221

Walker Z, Costa DC, Walker RW, Shaw K, Gacinovic S, Stevens T, Livingston G, Ince P, McKeith IG, Katona CL. Differentiation of dementia with Lewy bodies from Alzheimer's disease using a dopaminergic presynaptic ligand. J Neurol Neurosurg Psychiatry. 2002;73(2):134-140. DOI: 10.1136/jnnp.73.2.134

Welch A, Clack R, Natterer F, Gullberg GT. Toward accurate attenuation correction in SPECT without transmission measurements. IEEE Trans Med Imaging. 1997;16(5):532–541. PubMed PMID: 9368109

Weng YH, Yen TC, Chen MC, Kao PF, Tzen KY, Chen RS, Wey SP, Ting G, Lu CS. Sensitivity and specificity of 99mTc-TRODAT-1 SPECT imaging in differentiating patients with idiopathic Parkinson's disease from healthy subjects. J Nucl Med. 2004;45(3):393-401. PubMed PMID: 15001678

Yanch JC, Dobrzeniecki AB, Ramanathan C, Behrman R. Physically realistic Monte Carlo simulation of source, collimator and tomographic data acquisition for emission computed tomography. Phys Med Biol. 1992;37(4):853–870. DOI: 10.1088/0031-9155/37/4/003

Zaidi H. Relevance of accurate Monte Carlo modeling in nuclear medical imaging. Med Phys. 1999;26(4):574–608. PubMed PMID: 10227362

Zaidi H, Montandon ML. Which attenuation coefficient to use in combined attenuation and scatter corrections for quantitative brain SPET? Eur J Nucl Med Mol Imaging. 2002;29(7):967-969. PubMed PMID: 12212549

Zaidi H, Koral KF. Scatter modelling and compensation in emission tomography. Eur J Nucl Med Mol Imaging. 2004;31(5):761–782. PubMed PMID: 15057488

Zaidi H, El Fakhri G. Is absolute quantification of dopaminergic neurotransmission studies with ^{123}I SPECT ready for clinical use? Eur J Nucl Med Mol Imaging. 2008;35(7):1330–1333. DOI: 10.1007/s00259-008-0842-x

Zigmond MJ, Abercrombie ED, Berger TW, Grace AA, Stricker EM. Compensations after lesions of central dopaminergic neurons: some clinical and basic implications. Trends Neurosci. 1990;13(7):290–296. PubMed PMID: 1695406

Zubal IG, Early M, Yuan O, Jennings D, Marek K, Seibyl JP. Optimized, automated striatal uptake analysis applied to SPECT brain scans of Parkinson's disease patients. J Nucl Med. 2007;48(6):857–864. PubMed PMID: 17504864

Appendix A

Publications

Crespo C, **Gallego J**, Cot A, Falcón C, Bullich S, Pareto D, Aguiar P, Sempau J, Lomeña F, Calviño F, Pavía J, Ros D. Quantification of dopaminergic neurotransmission SPECT studies with ^{123}I-labelled radioligands. A comparison between different imaging systems and data acquisition protocols using Monte Carlo simulation. Eur J Nucl Med Mol Imaging. 2008;35(7):1334–1342. DOI: 10.1007/s00259-007-0711-z

Bullich S, Cot A, **Gallego J**, Gunn RN, Suárez M, Pavía J, Ros D, Laruelle M, Catafau AM. Impact of scatter correction on D_2 receptor occupancy measurements using ^{123}I-IBZM SPECT: Comparison to ^{11}C-Raclopride PET. Neuroimage. 2010;50(4):1511-1518. DOI: 10.1016/j.neuroimage.2010.01.013

Iranzo A, Lomeña F, Stockner H, Valldeoriola F, Vilaseca I, Salamero M, Molinuevo JL, Serradell M, Duch J, Pavía J, **Gallego J**, Seppi K, Högl B, Tolosa E, Poewe W, Santamaria J. Decreased striatal dopamine transporter uptake and substantia nigra hyperechogenicity as risk markers of synucleinopathy in patients with idiopathic rapid-eye-movement sleep behaviour disorder: a prospective study. Lancet Neurol. 2010;9(11):1070-1077. DOI: 10.1016/S1474-4422(10)70216-7

Mané A, **Gallego J**, Lomeña F, Mateos JJ, Fernández-Egea E, Horga G, Cot A, Pavía J, Bernardo M, Parellada E. A 4-year dopamine transporter (DAT) imaging study in neuroleptic-naive first episode schizophrenia patients. Psychiatry Res. 2011;194(1):79-84. DOI: 10.1016/j.pscychresns.2011.03.004

Muñoz E, Iranzo A, Rauek S, Lomeña F, **Gallego J**, Ros D, Santamaría J, Tolosa E. Subclinical nigrostriatal dopaminergic denervation in the cerebellar subtype of multiple system atrophy (MSA-C). J Neurol. 2011; 258(12):2248-2253. DOI: 10.1007/s00415-011-6108-8

Gallego J, Niñerola-Baizán A, Cot A, Aguiar P, Crespo C, Falcón C, Lomeña F, Sempau J, Pavía J, Ros D. Validation of semi-quantitative methods for DAT SPECT: influence of anatomical variability and partial volume effect. Phys Med Biol. 2015;60(15):5925-5938. DOI: 10.1088/0031-9155/60/15/5925